Ferroelectric phase transition and dynamical behavior of PNRs of potassium tantalate niobate crystals : broadband inelastic light scattering study

Md. Mijanur Rahaman

February 2016

Ferroelectric phase transition and dynamical behavior of PNRs of potassium tantalate niobate crystals : broadband inelastic light scattering study

Md. Mijanur Rahaman

Doctoral Program in Materials Science

Submitted to the Graduate School of
Pure and Applied Sciences
in Partial Fulfillment of the Requirements
for the Degree of Doctor of Philosophy in
Engineering

at the
University of Tsukuba

Abstract

The lead-based oxide relaxor ferroelectrics (RFEs) such as (1-x)Pb($Mg_{1/3}Nb_{2/3}O_3$)-$x$$PbTiO_3$ (PMN-xPT) and (1-x)Pb($Zn_{1/3}Nb_{2/3}O_3$)-$x$$PbTiO_3$ (PZN-xPT) have been extensively used in piezoelectric devices for their colossal piezoelectricity and dielectric responses. However, its future applicability is highly limited because of the toxic nature of lead. Therefore, the development of lead free ferroelectric materials is the urgent topic in materials science from an environmental view point. In the midst of lead free ferroelectrics, the potassium tantalate niobate ($KTa_{1-x}Nb_xO_3$, KTN) exhibits high quadratic electro-optic (EO) coefficient and good photorefractive effects. In addition, the excellent piezoelectric and high EO effects of KTN are improved by the Li-doping. Therefore, KTN emerges as the potential alternative of the lead-based ferroelectrics as a promising material for the applications to not only optical but also electromechanical devices. KTN has been extensively studied due to a unique combination of physical properties and lead free chemical composition. However, the microscopic origin of the Fano resonance, a phenomenon in which a discrete state interferes with the continuum states results in an asymmetric line shape, at around 196 cm^{-1} in not only non-doped KTN but also Li-doped KTN still remains unclear. Moreover, in non-doped Nb rich KTN and Li-doped KTN, the experimental evidence of polar nanoregions (PNRs), which was responsible for the excellent EO and piezoelectric response, is rather scarce.

In this study, the high quality non-doped Nb rich KTN and Li-doped KTN single crystals were investigated to clarify the precursor dynamics and the related physical properties by Brillouin and Raman scattering. The comparative study between non-doped KTN and Li-doped KTN was performed to discuss the effect of Li-doping on PNRs and the lattice dynamical properties related to a relaxor ferroelectric (RFE) phase transition. The physical origin of the Fano resonance in Li-doped KTN single crystals was discussed on the basis of the results of Raman scattering.

The precursor dynamics of a relaxor-like phase transition in KTN crystals with x = 0.40 (KTN/0.40) were investigated by Brillouin and Raman scattering. Upon cooling, the remarkable increase in the damping of the LA phonon and significant softening of the frequency of the TA phonon start at 45 K above the Curie temperature of T_C = 308 K, which is defined as the intermediate temperature, T^* ~ 353 K, implying the start of the rapid growth of the dynamic PNRs. The coupling of the LA and the TA phonons with the fluctuations of local polarization in PNRs caused a prominent elastic anomalies in the vicinity of T_C. The relaxation time estimated from the central peak (CP) shows a critical slowing down towards T_C, which is the evidence for the order-disorder nature of a ferroelectric phase transition. The evolution of the dynamic PNRs is discussed by the estimation of their length scale, and it is found that it starts to increase near T^* and gradually grows towards T_C. The breaking of local symmetry and the microscopic origin of the central peak (CP) in the cubic phase caused by the A_1(z) symmetry of PNRs with a rhombohedral *R3m* symmetry were discussed on the basis of the results of the angular dependence of Raman scattering. The phase difference between different Raman tensor components related to PNRs with the A_1(z) symmetry was observed.

The high quality 5%Li doped-KTN crystals with x = 0.27 (KLTN/0.05/0.27) was studied to investigate the effect of Li-doping on the lattice dynamical properties related to a RFEs phase transition in comparison with the non-doped KTN/0.40 crystal. The anomalous changes of the elastic properties in the KLTN/0.05/0.27 were observed in the vicinity of the T_C = 304 K. By the Li-doping, the temperature region of the elastic anomaly was extended in comparison with that of the non-doped KTN crystal. This fact demonstrates that the Li-doping enhances the growth of PNRs, while the remarkable elastic anomaly just above T_C is suppressed. The growth of PNRs was also evident from the change in the behavior of the

CP in comparison with the non-doped KTN. The broadening of the elastic anomaly can be the evidence of the enhanced diffusive nature of the ferroelectric phase transition, which is induced by Li ions. By the Li-doping, the enhanced diffusive nature was also confirmed by the dielectric properties using the extended Curie-Weiss law.

The Li-doping effect in KLTN/0.05/0.27 crystal was also studied by the observation of the critical slowing down using Brillouin scattering, transformation of local symmetry of PNRs by Raman scattering, and first-principles calculations. Above the T_C, the suppression of the critical slowing down of 5%Li-doped KTN was clearly observed in comparison with that of the non-doped crystal. It can be attributed to the increase of the random fields by the Li-doping. By the 5%Li-doping in KTN, the transformation of local A_1(z) symmetry to $E(x,y)$ symmetry of PNRs was observed by Raman scattering. The site occupancy for the 5%Li-doping in the perovskite structure was calculated by the density functional theory, and it shows that 4.2%Li ions occupy at A-site, while the 0.8%Li ions occupy at B-site. In the 5% Li-doped KTN crystals, the hetero-valence random occupation of 0.8% Li ions at B-site can be the origin to enhance the random fields strength. The microscopic origin of the stretched critical slowing down and the change of the local symmetry of PNRs in 5%Li-doped KTN crystal can be the hetero-valence charge disorder at B-site, which is induced by the partial occupancy of Li ions at B-site.

The enhancement of functionality of perovskite ferroelectrics by local structure is one of current interests. By the Li-doping to KTN, the large piezoelectric and electro-optic effects were reported. In order to give new insights into the mechanism of doping, the microscopic origin of the Fano resonance induced by the local structure was investigated in 5%Li-doped KTN single crystals by Raman scattering. The coupling between the continuum states and the transverse optical phonon near 196 cm^{-1} (Slater mode) caused a Fano resonance. In the vicinity of the T_C = 304 K, the almost disappearance of the Fano resonance and the remarkable change of the CP intensity were observed upon heating. The local broken symmetry of the polar nanoregions (PNRs) related to CP was determined to $E(x,y)$ symmetry by the angular dependence of Raman scattering. The electric field induced the significant change in the intensity of both CP and Fano resonance. From these experimental results, it is concluded that the origin of the Fano resonance in 5%Li-doped KTN crystals is the coupling between polarization fluctuations in PNRs and the Slater mode, both belong to the $E(x,y)$ symmetry.

As for integrated optics a value of T_C near room temperature (RT) is desirable, therefore it is necessary to study the composition gradient of a KTN crystal wafer sliced from a bulk as grown crystal of which T_C is close to RT. The composition gradient Li-doped $KTa_{1-x}Nb_xO_3$ wafer with the size of about 3.5 cm square with thickness 1.5 mm was investigated by micro-Brillouin scattering. The positional dependence of elastic constants was clearly observed. The origin of positional dependence was discussed by the comparison with the temperature variation of elastic constants of the homogeneous crystal. The difference of elastic constants between high and low defect density regions in a wafer was also studied.

Table of Contents

Chapter 1

Ferroelectrics and Theory of Structural Phase Transition

1.1 Ferroelectricity

In crystal symmetry, there are 32 microscopic point groups, among them 11 point groups are centro-symmetric and 21 are noncentro-symmetric. A crystal having a centro-symmetric does not possess any polarity and also has no third-rank tensor properties such as linear electro-optic and piezoelectric effects. The other 21 noncetro-symmetric groups can possess one or more crystallographic unique directions. All of the noncentro-symmetry groups exhibit third-rank tensor properties along a unique direction except 432 point group. In the midst of the noncentro-symmetry groups, 10 point groups, i.e., *1, 2, m, mm2, 4, 4mm, 3, 3m, 6* and *6mm* are referred to as pyroelectric classes. A crystal having one of this point group symmetry has a unique rotation axis, but does not have any mirror perpendicular to this axis. Consequently, the atomic arrangement at one end along the unique rotation axis is different from that at the other end. Hence, the crystal becomes bi-polar and it shows spontaneous polarization.[1] Ferroelectricity is the phenomenon which refers to the state of spontaneous polarization, i.e., polarization of the material in the absence of an electric field. The phenomenon of ferroelectricity was observed in 1921 for the first time in Rochelle salt, $NaKC_4H_4O_6.4H_2O$.[2]

A crystal is said to be ferroelectric when it possesses an electric polarization in the absence of an external applied electric field, and the direction of the polarization can be reversed by the application of an external electric field. The important characteristics of ferroelectric materials are: (i) the existence of spontaneous polarization and ferroelectric domains (ii) *P-E* hysteresis loop and (iii) ferroelectric Curie temperature (T_C) at which a ferroelectric crystal undergoes a structural phase transition from a paraelectric phase to ferroelectric phase.

1.2 Properties of ferroelectrics

1.2.1 Ferroelectric domains and domain walls

A ferroelectric domain is a region in which the spontaneous polarization is uniformly oriented. The six possible orientation of spontaneous polarization in the ferroelectric tetragonal phase is displayed in Fig. 1.1.

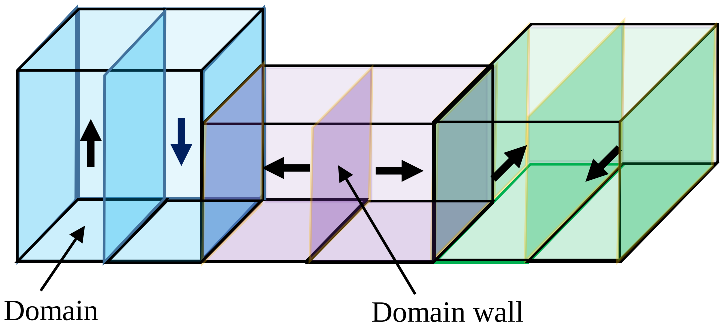

Fig. 1.1. Schematic illustration of ferroelectric domains and domain walls in ferroelectric materials. The arrow indicates the direction of the spontaneous polarization.

The interface between two domains is called a domain wall (Fig. 1.1). In a tetragonal ferroelectric phase, the angles between two domains are either 90° or 180°, whereas they are 71°, 109°, or 180° in a rhombohedral phase. The walls separated by oppositely oriented polarization are called 180° domain walls, while 90° domain walls separate perpendicular domains. The 180° domains can be reversed with minimal structural strains. However, a significant structural deformation is required for switching of 71°, 90°, and 109° domains.

1.2.2 *P-E* hysteresis loop

Figure 1.2 shows the typical ferroelectric *P-E* hysteresis loop. When an external electric field is applied in one direction, the polarization of domains with an unfavorable direction of polarization trend to align in the direction of the applied field.[1] When all of the domains are aligned in the direction of the filed, the nominal value of the polarization becomes a maximum, and is called saturated or spontaneous polarization, P_s. This process is reversible and is called polarization switching. When the field reduces to zero, the polarization does not return back to the initial value. The amount of switchable polarization after the removal of an applied field is called the remnant polarization, P_r. The application of the reverse electric field is required to reach the initial state of polarization. The strength of the electric field to bring the initial sate of polarization is called the coercive field, E_C. The process can be repeated.

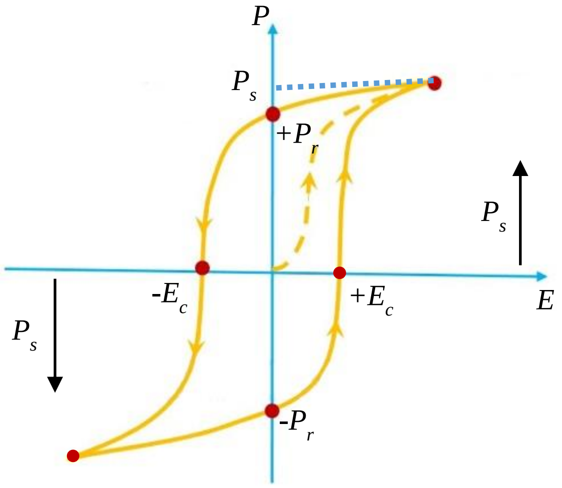

Fig. 1.2. Typical diagram of a *P-E* hysteresis loop in ferroelectric materials.

1.2.3 Ferroelectric Curie temperature and phase transition

One of the important property of the ferroelectric materials is the temperature of structural phase transition. The certain temperature at which a ferroelectric material under goes structural phase transition from a paraelectric phase to a ferroelectric phase is called the Curie temperature (T_C). If there are more than one ferroelectric phase in a crystal, the T_C only determine the temperature at which a paraelectric to ferroelectric phase transition occurs. The temperature at which a crystal transforms from one ferroelectric phase to another ferroelectric phase is simply called the transition temperature.

The concept of phase transition is vital for explaining ferroelectric properties. In general, the phase transitions are characterized by a quantity referred to as the order parameter, $\eta(T)$, which decreases with increasing temperature and goes to zero at the T_C. The parameter $\eta(T)$ denotes the polarization in the case of ferroelectric phase transition. In accordance with the nature of the order parameter and the details of its interaction with the macroscopic parameter such as strain, there are three types of phase transition observed in crystals, namely; order-disorder, displacive, and electronic. The order-disorder and the displacive involve order parameters which are primarily atomic, whereas electronically induced transitions involve an electron-lattice coupled order parameter.

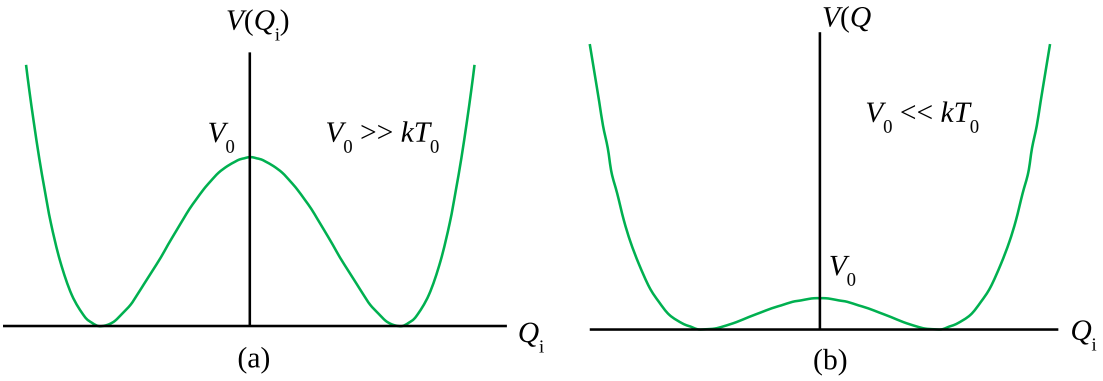

Fig. 1.3. Single cell potentials in (a) order-disorder type and (b) displacive type structural phase transitions.

The order-disorder and the displacive types of phase transition can be distinguished in terms of a single cell potential (Fig. 1.3.) for a special coordinate Q with an anharmonic potential of the form[3]

$$V(Q) = aQ^2 + bQ^4 \tag{1.1}$$

with constants $a < 0$ and $b > 0$. The Eq. (1.1) corresponds to a double well potential with an energy difference V_0 between the maximum and two minima. When $V_0 >> kT_0$ (T_0 is the transition temperature), the phase transition would be an associated with the dynamic ordering at one site or orientation. When $V_0 << kT_0$, a cooperative displacements of atoms along Q occurs upon cooling from high temperature, which describes the limiting case of a displacive type phase transition. In inelastic light scattering spectra, the displacive type phase transition is characterized by the existence of the soft optic phonon, whereas the presence of the central peak symbolize the order-disorder type phase transition in case of ferroelectric materials.

1.2.4 Electrostrictive effect

The electrostriction is an electromechanical phenomenon in all dielectric materials, and is caused by a small displacements of ions in the crystal upon being exposed to an external field result in overall strain in the direction of the field. The electrostrictive effect describes the electric field/polarization induced strain (S_{ij}), which is proportional to the square of the electric field/polarization in the following equations:

$$S_{ij} = M_{ijkl} E_k E_l \tag{1.2}$$

$$S_{ij} = Q_{ijkl} P_k P_l \tag{1.3}$$

where M_{ijkl} and Q_{ijkl} are the electrostrictive coefficients. The electrostriction is a four-rank tensor property and it can be observed in all crystalline materials.[4] The electrostrictive coefficients are related to each other via the dielectric susceptibility by the following relation:

$$M_{ijmn} = \sum_{kl} \chi_{km} \chi_{ln} Q_{ijkl} \tag{1.4}$$

The Eq. (1.2) holds only for weak fields, thus Eq. (1.3) is more suitable one, whereas the Eq. (1.4) is always valid for pure electrostrictive effect. In ferroelectric materials, therefore, piezoelectric effect is a kind of electrostriction biased by the P_s. In general, the piezoelectric effect is much larger than the electrostrictive effect. However, in certain materials the electrostrictive effect dominates and is preferred because the strain direction is independent of the field direction and hysteresis effects are reduced. The $Pb(Mg_{1/3}Nb_{2/3})O_3$ (PMN), $PbTiO_3$ (PT) and PMN-*x*PT are the most commonly used electrostrictive materials.

1.2.5 Piezoelectric effect

The effect known as piezoelectricity was discovered by Pierre and Jacque Curie in 1880.[5] The term “piezoelectricity” comes from the Greek word *piezo or piezein*, which means to squeeze or press. In a more precise sense, piezoelectricity means the ability of materials by which we can convert mechanical stress into electric charge.[6] In crystalline materials with centro-symmetry structure, the piezoelectric effect is understood as the linear electromechanical interaction between the mechanical and the electrical state. For ferroelectric materials whose paraelectric phase is centro-symmetric, the piezoelectric coefficient d_{mij} can be expressed as a derivative of strain to electric field by

$$d_{mij} = \frac{\partial S_{ij}}{\partial E_m} = \frac{Q_{ijkl} P_k \partial P_l}{\partial E_m} + \frac{Q_{ijkl} P_l \partial P_k}{\partial E_m} \tag{1.5}$$

$$d_{mij} = Q_{ijkl} P_k \varepsilon_{lm} + Q_{ijkl} P_l \varepsilon_{km} \tag{1.6}$$

where ε_{ij} is the dielectric permittivity.

1.2.6 Electro-optic effect

In a material, the speed of light is mainly determined by its refractive index, *n*, and is defined as the ratio of the velocity of light in vacuum *c* to that in the material *V*, i.e., $n = c/V$. Maxwell’s equations show that the propagation velocity of light in non-magnetic materials is given by the following equation, in which the relative permeability (μ/μ_0) is taken as 1.

$$V = \frac{c}{\sqrt{\varepsilon_\infty}}, \text{ and } n = \sqrt{\varepsilon_\infty}, \tag{1.7}$$

where ε_∞ is the dielectric constant that associates with the dielectric displacement (*D*) and electric field at optical frequency in the medium as $D = \varepsilon_0 \varepsilon_\infty E$, here, ε_0 is the permittivity in vacuum. When an electric field is applied to certain materials, the optical properties of these are changed. This is caused by the forces that distort the orientation, position, or shape of the molecule, which constitute of the materials. The electro-optic effect is the change in the refractive index resulting from the application of a dc or low frequency electric filed. For non-linear polarization properties:

$$D = \varepsilon_0 \varepsilon_\infty E + \alpha E^2 + \beta E^3 \tag{1.8}$$

where α and β are the non-linear co-efficients of the materials. The permittivity of materials is defined by the slope of the curve:

$$\frac{\partial D}{\partial E} = \varepsilon_0 \varepsilon_\infty + 2\alpha E + 3\beta E^2 \tag{1.9}$$

In Eq. (1.9), the first term is a constant and other terms demonstrate the change in permittivity owing to the applied electric field. Since the refractive index of materials is directly related to its permittivity, therefore the refractive index also changes under the electric filed due to the non-linear effect. This phenomenon is known as the electro-optic effect, which was first discovered in 1875 by Kerr. For simplicity, the change in refractive index can be described as a modulation of the optical impermeability by the external electric field:

$$\Delta\left(\frac{1}{n_{ij}^2}\right) = r_{ijk}E_k + R_{ijkl}E_kE_l \,, \tag{1.10}$$

where the first term is a linear electro-optic effect known as *Pockels effect* with the coefficient r_{ijk} , and the second term is a quadratic electro-optic effect known as *Kerr effect* with the coefficient R_{ijkl}.[7] The co-efficient r_{ijk} describing the linear electro-optic effect is a third rank-tensor, and is absent in materials with a centro-symmetry.

1.3 Classification of ferroelectrics

On the basis of their dielectric, polarization, and phase transition scenario, ferroelectrics can be classified into two categories:[8,9]

(i) Normal ferroelectrics
(ii) Relaxor ferroelectrics

(i) Normal ferroelectrics: The normal ferroelectric materials exhibits weak frequency dependent of the dielectric permittivity and under goes a sharp or progress vanishing of the spontaneous polarization, P_s, related to a first or second order phase transition. In the paraelectric phase of normal ferroelectrics, the dielectric constant follow the well-known Curie-Weiss law as follows:

$$\frac{1}{\varepsilon} = \frac{(T\text{-}T_C)}{C}\,,\ T > T_C \tag{1.11}$$

where T_C and C are the Curie temperature and Curie constant, respectively. The temperature dependence of the dielectric constant of a normal ferroelectric $BaTiO_3$ single crystal is shown in Fig. 1.4.

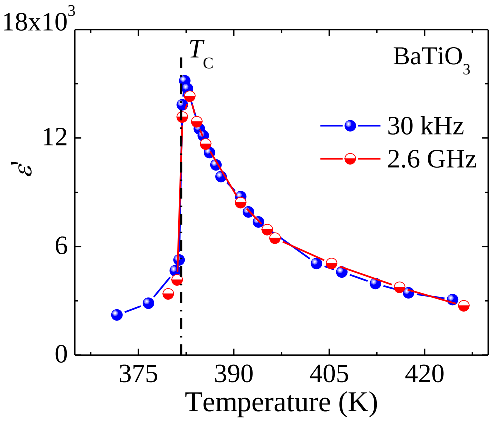

Fig. 1.4. The temperature dependence of the dielectric constant of a $BaTiO_3$ (BT)[10] single crystal at some selected frequencies.

(i) Relaxor ferroelectrics: The relaxor ferroelectrics (RFEs) possess a diffuse phase transition over a wide range of temperature and exhibit strong frequency dispersion on the lower side of the temperature of dielectric maximum, T_{m}, as shown in Fig. 1.5. In the high temperature range RFEs first follow the Curie-Weiss law, but show the deviation from it below the Burns temperature, T_{B}, at which dynamic polar nanoregions (PNRs) starts to appear. Below the T_{B}, the dielectric permittivity in the paraelectric phase of the RFEs can be explained by the following phenomenological equation:[11]

$$\frac{1}{\varepsilon} = \frac{1}{\varepsilon_{\mathrm{m}}}\left[1+\frac{(T\text{-}T_{\mathrm{m}})^{\gamma}}{2\delta^{2}}\right], \quad (T > T_{\mathrm{m}})\ ;\ 1 < \gamma \leq 2 \tag{1.12}$$

where ε_{m} is the magnitude of the dielectric peak at the T_{m}. γ and δ are fitting parameters mentioning the degree of the diffuseness of the phase transition. When γ = 1, Eq. (1.12) is the same as Curie-Weiss relation, while the case of γ = 2 describe a typical relaxor property. It is believed that such a peculiar properties in relaxor ferroelectrics attributed to random fields related to PNRs.

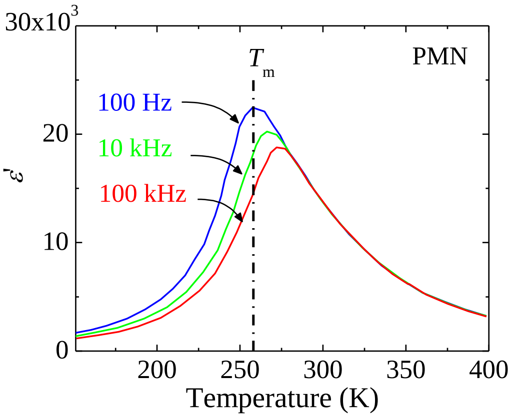

Fig.1.5. The dielectric constant of the $Pb(Mg_{1/3}Nb_{2/3})O_3$ (PMN)[11] single crystal at some selected frequencies as a function of temperatures.

1.4 Existence of polar nanoregions (PNRs) above the T_{m}

Albeit the existence of polar nanoregions (PNRs) in relaxor ferroelectrics (RFEs) seems to be doubtless; however, the exact knowledge of the cause and mechanism of their formations is far from completely understood. In RFEs, the presence of PNRs was first observed by Burns and Docal[12-14] in measurements of the refractive index, n, as a function of temperature as shown in Fig. 1.6. In normal ferroelectrics, upon cooling from high temperature, the n decreases linearly with decreasing temperature down to T_{C} where n deviates from the linearity. The abrupt change of the n at T_{C} is for the first order normal ferroelectric materials. Below the T_{C}, n has an extra contribution that varies as the square of the spontaneous polarization, P_{s}. On the other hand, the n starts to deviate from linearity well above T_{C} in the case of RFEs. The temperature of the onset of the deviation of the n is known as the Burns temperature, T_{B}, which is 620 K for the $Pb(Mg_{1/3}Nb_{2/3})O_3$ (PMN) RFEs.[13] This effect was rationalized by the quadratic electro-optic effect. This effect arises in all crystals classes and relates in change in refractive index to the square of the local polarization, P_{d}. There is no macroscopic polarization i.e., $\sum P_{\mathrm{d}} = 0$ because of random orientation of PNRs, however, $\sum P_{\mathrm{d}}^{2} \neq 0$. The existence of PNRs well above T_{m}, at which the dielectric constant attains a maximum value, also came from high resolution transmission electron microscope (TEM) and showed their growth with decreasing temperature.[15,16]

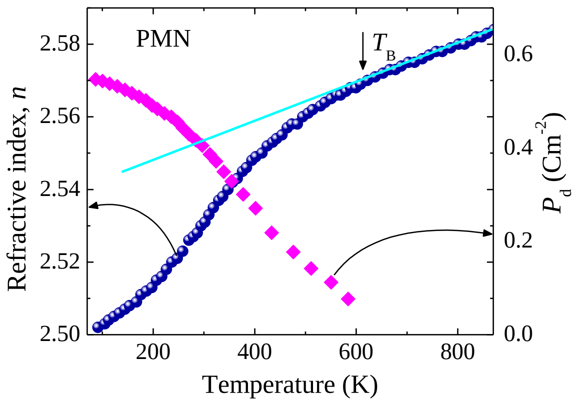

Fig. 1.6. The temperature dependence of the refractive index, n and calculated local polarization, P_d, in $Pb(Mg_{1/3}Nb_{2/3})O_3$ (PMN) relaxor ferroelectrics as a function temperatures after Burns and Dacol.[13] The solid line is guide to eyes.

1.5 Theory of structural phase transition of ferroelectrics

1.5.1 Thermodynamics of the phase transition

A phenomenological or thermodynamic theory which is used extensively to explain the phase transition is the Landau-Ginzburg free energy theory.[17,18] By considering the polarization, P, as an order parameter, Devonshire[19,20] developed a phenomenological theory of ferroelectricity based on the Landau-Ginzburg theory of phase transition. In this theory, the thermodynamic potential is expressed in terms of an order parameter. In general, the most convenient thermodynamic potential is the elastic Gibbs function, G_1, which can be expressed as a function temperature, stress, and polarization.[21] For simplicity, Devonshire considered a ferroelectric crystal having an intrinsic spontaneous polarization, P_s, along a specific axis, and expressed the G_1 as a function of polarization by the following equation:[20]

$$G_1(T,P)\text{-}G_0(T) = \tfrac{1}{2}\beta(T)P^2+\tfrac{1}{4}\xi(T)P^4+\tfrac{1}{6}\zeta(T)P^6+\dots, \qquad (1.13)$$

where G_0 is the free energy for P = 0. A stable state of a thermodynamic system is characterized by the minimum value of the G ($G_1 = G$, when E = 0). The conditions for the minimum value of the G are given by

$$E = \left(\frac{\partial G}{\partial P}\right)_{Ps}, \ \left(\frac{\partial^2 \mathrm{G}}{\partial P^2}\right)_{Ps} > 0 \text{ , or } \left(\frac{\partial E}{\partial P}\right)_{Ps} = \chi^{-1} > 0 \qquad (1.14)$$

If Eqs. (1.13) and (1.14) are combined, the equation takes the following form:

$$E \ = \frac{\partial G}{\partial P} = P_s(\beta + \xi P_s^2 + \zeta P_s^4) = 0, \qquad (1.15)$$

$$\chi^{-1} = (\beta + 3\xi P_s^2 + 5\zeta P_s^4) > 0 \qquad (1.16)$$

where E is the Maxwell field (parallel to P_s). The G versus P_s curves are qualitatively sketched in Fig. (1.7) with the Eq. (1.13) in which ξ and ζ are positive. When the value of the β is positive the free energy curve has single minimum at P_s = 0, but when β is negative the curve acquires a double-minimum at non-zero value of polarization. Since the minima describe the equilibrium value of polarization as a function of temperature, therefore the change of the value of the β from positive to negative corresponds to change of the stable paraelectric state with $P = 0$ to a ferroelectric state with $P_s \neq 0$. This is called the ferroelectric phase transition.

If $P_s = 0$, the Eq. (1.16) can be expressed as

$$\chi^{-1} = \beta > 0 \tag{1.17}$$

It is clear that β must be a positive value when a stable state is paraelectric phase. Thus, the boundary condition at T_C is $\beta \geq 0$. Expanding β as a Taylor series in (T-T_0) and considering only the first term in (T-T_0), β can be expressed as

$$\beta = \beta_0 (T\text{-}T_0) \tag{1.18}$$

By combining Eqs. (1.17) and (1.18), the dielectric susceptibility can be expressed by the following equation.

$$\chi = \frac{1}{\beta\ (T - T_0)} \tag{1.19}$$

This is called the Curie-Weiss law that applies to the dielectric permittivity in the paraelectric phase. Since ξ and ζ have a very weak temperature dependence, therefore it can be neglected. However, in the case of $P_s \neq 0$, one result corresponds to first order phase transition when $\xi < 0$, and other result to a second order phase transition when $\xi > 0$. According to the Devonshire theory, the temperature dependence of the free energy, polarization, and dielectric susceptibility for the second order and first order phase transition are displayed in Fig. 1.7 and 1.8, respectively.

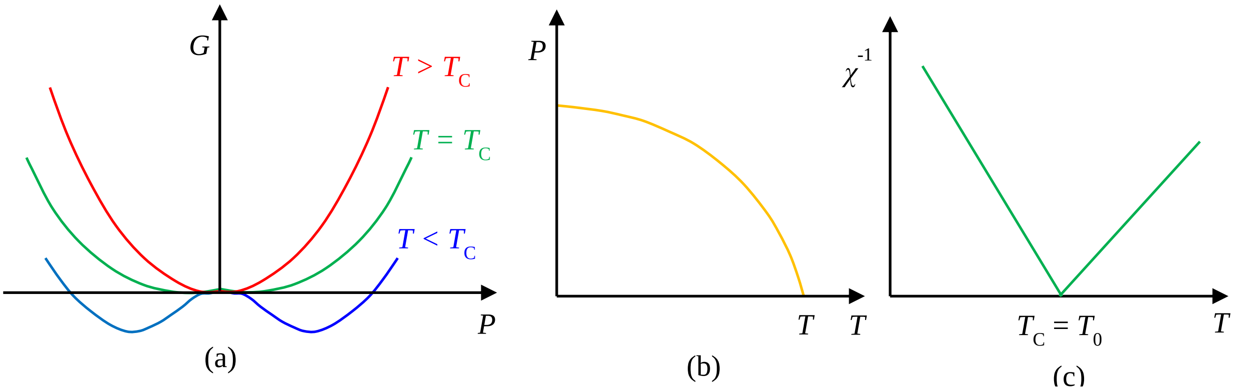

Fig. 1.7. The temperature dependence of (a) the free energy, (b) polarization, and (c) dielectric susceptibility for the second order phase transition.

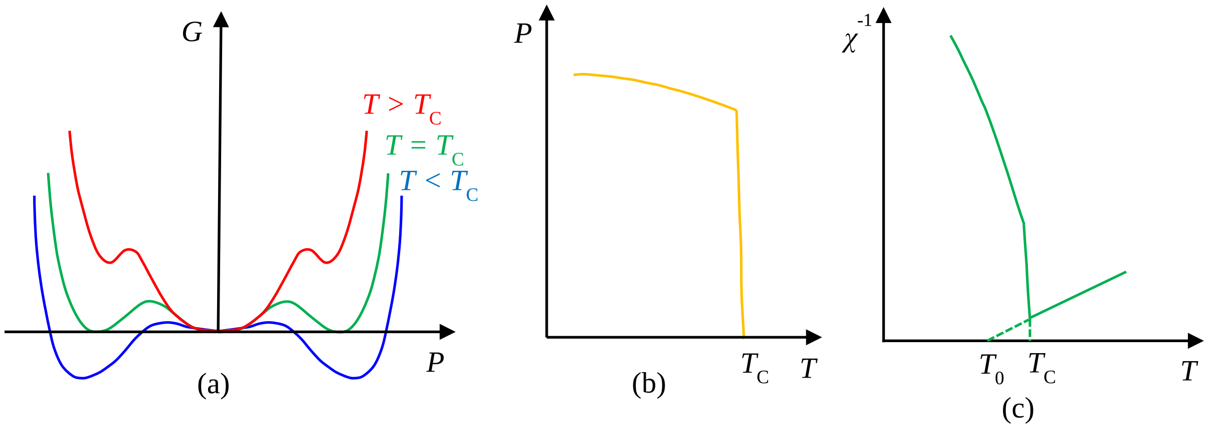

Fig. 1.8. The temperature dependence of (a) the free energy, (b) polarization, and (c) dielectric susceptibility for the first order phase transition.

1.5.2 Devonshire theory

In ferroelectric materials, Devonshire rationalized the phase and phase transition mechanism in terms of Landau-type expansion of the free energy in terms of an order parameter polarization, *P*. He induced a straightforward model with a single temperature dependent second order coefficient and three temperature independent higher order coefficients for the expansion of the free energy to six order in *P*.[19] The free energy, *G*, can be expressed as a function of polarization components P_x, P_y, and P_z by the following reation:

$$G=\frac{1}{2}\beta\left(P_x^2+P_y^2+P_z^2\right)+\frac{1}{4}\xi_{11}^{'}\left(P_x^4+P_y^4+P_z^4\right)+\frac{1}{2}\xi_{12}^{'}\left(P_y^2P_z^2+P_z^2P_x^2+P_x^2P_y^2\right)+\frac{1}{6}\zeta^{'}\left(P_x^6+P_y^6+P_z^6\right) \qquad (1.20)$$

where β is a decreasing function of temperature which passes through a zero value in the vicinity of the paraelectric to ferroelectric phase transition, and $\xi_{11}^{'}$, $\xi_{12}^{'}$, and $\zeta^{'}$ are the temperature independent coefficients in which $\zeta^{'} > 0$, $\xi_{12}^{'} > 0$, and $\xi_{11}^{'} < 0$.

The derivatives of the *G* with respect to P_x give the field components for the unstressed crystal.

$$E_x = \frac{\partial G}{\partial P_x} = \beta P_x + \xi_{11}^{'}P_x^3 + \xi_{12}^{'}P_x\left(P_y^2 + P_z^2\right) + \zeta^{'}P_x^5 \qquad (1.21)$$

In the absence of electric field, E_x must be zero and for stability free energy must be a minimum. When β is sufficient large, the minimum value of *G* corresponds to zero polarization. However, for β small or negative, the minimum value of the *G* will correspond to a finite polarization. The second order term in Eq. (1.20) is the direction independent, but for a given resultant polarization the fourth and sixth order terms have its minima along the axial and diagonal directions, respectively. Therefore, when the temperature decreases and the magnitude of the polarization increases the direction of the polarization will change from an axial to a diagonal one. For zero electric field, the Eq. (1.21) and similar equations become:

$$\begin{aligned}
&P_x = 0, \text{ or } \zeta^{'}P_x^4 + \xi_{11}^{'}P_x^2 + \xi_{12}^{'}\left(P_y^2 + P_z^2\right) + \beta = 0,\\
&P_y = 0, \text{ or } \zeta^{'}P_y^4 + \xi_{11}^{'}P_y^2 + \xi_{12}^{'}(P_z^2 + P_x^2) + \beta = 0, \qquad (1.22)\\
&P_z = 0, \text{ or } \zeta^{'}P_z^4 + \xi_{11}^{'}P_z^2 + \xi_{12}^{'}\left(P_x^2 + P_y^2\right) + \beta = 0,
\end{aligned}$$

For corresponding minima of the *G*, there are four sets of solution of these equations

$$\begin{aligned}
&P_x = P_y = P_z = 0,\\
&P_x = P_y = 0, \zeta^{'}P_z^4 + \xi_{11}^{'}P_z^2 + \beta = 0,\\
&P_x = 0, P_y = P_z\,, \ \zeta^{'}P_z^4 + \left(\xi_{11}^{'} + \xi_{12}^{'}\right)P_z^2 + \beta = 0, \qquad (1.23)\\
&P_x = P_y = P_z\,, \ \zeta^{'}P_z^4 + \left(\xi_{11}^{'} + 2\xi_{12}^{'}\right)P_z^2 + \beta = 0
\end{aligned}$$

Hence, upon cooling from high temperature, the polarization, which was zero in the paraelectric phase, will in turn point along a cubic edge, a face diagonal, and a body diagonal. The corresponding effect on the crystal symmetry will be to change from the paraelectric cubic ($Pm\bar{3}m$) symmetry successively to tetragonal (*P4mm*), orthorhombic (*Pmm2*) and rhombohedral (*R3m*) symmetry. The typical directions of polarization in respective phase are depicted in Fig. 1.9.

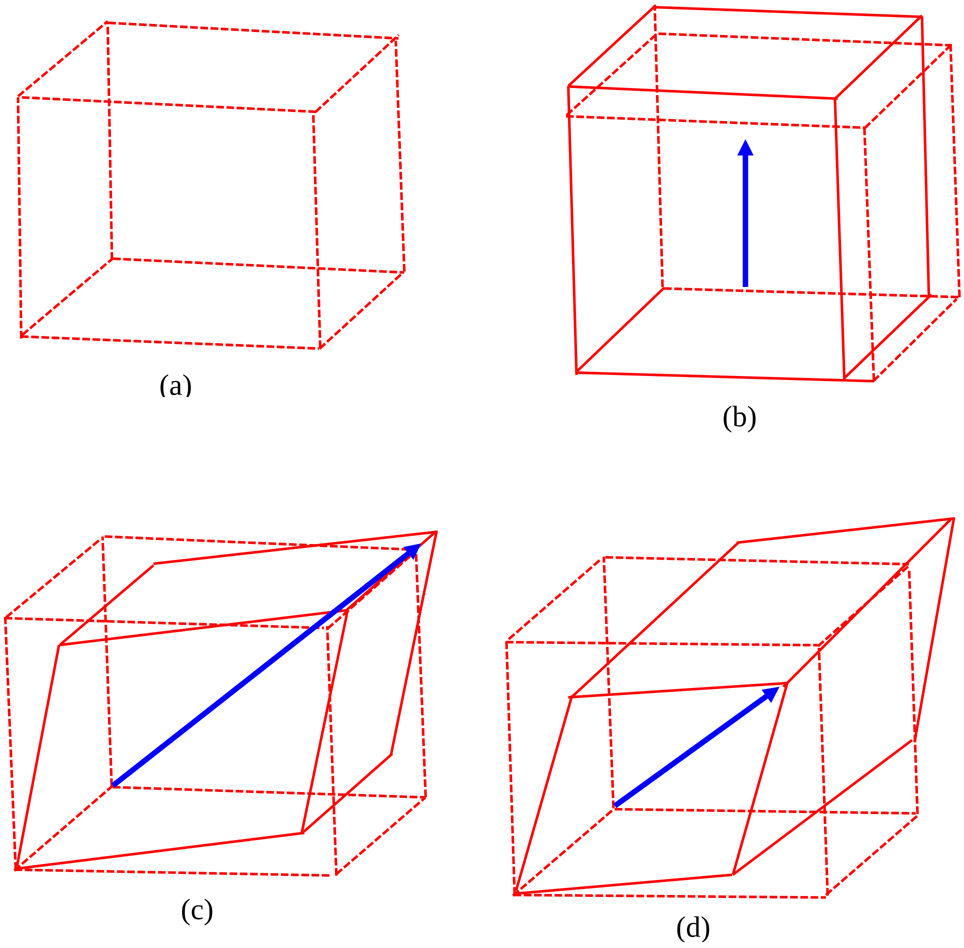
(a) (b) (c) (d)

Fig. 1.9. Schematic illustration of the direction of polarization in (a) cubic phase (b) tetragonal phase (c) orthorhombic phase (d) rhombohedral phase.

1.6 Perovskite structures

The name of perovskite is originated from Perovsky who discovered mineral crystals composed of calcium titanate, with the chemical formula $CaTiO_3$. The materials which have the same type of crystal structure as $CaTiO_3$, known as the perovskite structure. The general chemical formula for perovskite oxide compounds is ABO_3, where O is oxygen, A represents a cation with a larger ionic radius, and B a cation with a smaller ionic radius. Figure 1.10 shows a unit cell of the ABO_3-type cubic perovskite structure. Most of the ferroelectrics with the perovskite-type structure are compounds with either $A^{2+}B^{4+}O_3^{2-}$ or $A^{1+}B^{5+}O_3^{2-}$-type formula. The crystals with perovskite ABO_3-type structure, and its derivative have received significant attention because the structure can accommodate various metals with a wide range of valence and ionic radii. The perovskite structure is essentially a three dimensional network of BO_6 octahedral, it can be considered also as a cubic close pack arrangement of A and O ions with B ions filling the octahedral interstitial positions.

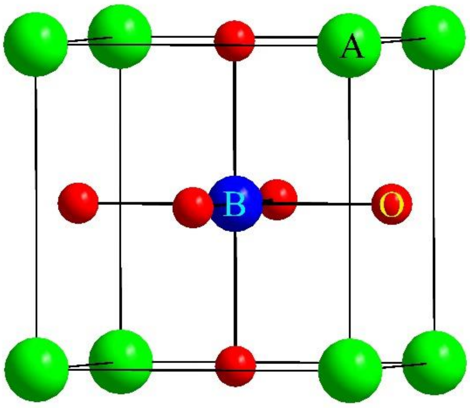

Fig.1.10. A cubic ABO_3-type perovskite unit cell.

The stability of the BO_6 octahedral can be described by the tolerance factor, *t*:

$$t = \frac{R_A + R_O}{\sqrt{2}(R_B + R_O)} \qquad (1.24)$$

where R_A, R_B and R_O are the ionic radii of A, B and O ions, respectively. The *t* can be used as a degree of distortion of a perovskite from the ideal cubic phase. Therefore, the closer to the cubic, the value of the *t* closer to the unity. In general, to form a stable perovskite structure, one requires $0.9 < t < 1.1$. Above the T_C, these materials have a centro-symmetric structure and therefore lose all spontaneous polarization. In this state, the material is termed as paraelectric. When the temperature is lowered trough the T_C, a phase transformation takes place from the paraelectric to the ferroelectric state. The transitions from the ideal cubic phase to the tetragonal, orthorhombic, and rhombohedral phases are well known in many perovskite ferroelectric materials. These transitions from the cubic perovskite structure proceed from a simple distortion of the cubic unit cell, or an enlargement of the cubic unit cell, or a combination of both.

From an environmental view point, the advancement of lead free ferroelectric is the urgent topic in material sciences. The well-known lead free perovskite ferroelectrics are barium titanate ($BaTiO_3$), potassium niobate ($KNbO_3$), potassium sodium niobate ($K_xNa_{1-x}NbO_3$), and potassium tantalate niobate ($KTa_{1-x}Nb_xO_3$). Among them the study of $KTa_{1-x}Nb_xO_3$ (KTN) has attracted a great deal of attention owing to their enormous quadratic electro-optic coefficient[22,23], large electrostriction[24], and excellent piezoelectric effect[25], which make them one of the potential candidates for not only optical but also electromechanical device applications.

1.7 Ideas and goals of my Ph.D. study

The lead-based oxide perovskite relaxor ferroelectrics (RFEs) have attracted much attention because of their outstanding electromechanical properties and potential applications in piezoelectric devices.[26-28] However, lead affects on the natural environment owing to its toxicity. Therefore, the development of the lead free ferroelectric materials is an imperative matter in applied physics. The potassium tantalate niobate ($KTa_{1-x}Nb_xO_3$, KTN) is one of the well-known lead free relaxor-like ferroelectrics with the ABO_3-type perovskite structure. The investigation of KTN has fascinated much scientific attention because of their high quadratic electro-optic coefficient and excellent photorefractive effect in the vicinity of the paraelectric to ferroelectric phase transition[22,29], which make them one of the promising material for the application to the optical devices such as an optical beam scanner, an optical intensity modulator, an optical beam deflector, a varifocal lens, and an optical coherence tomography.[30-35]

The KTN crystals are the solid solution of the potassium tantalate ($KTaO_3$) and potassium niobate ($KNbO_3$). Its end member of $KTaO_3$ displays a quantum paraelectricity and retains a cubic symmetry down to 0 K because of quantum fluctuations.[36] KTN crystals undergo a successive phase transition of a cubic-tetragonal-orthorhombic-rhombohedral sequence as same as $KNbO_3$ ($x = 1$) for solid solutions of $x > 0.05$, and three phase transition temperature can be modified by the Nb content.[37,38] The KTN crystal of $x = 0.008$-0.05 undergoes a cubic-rhombohedral phase transition without tetragonal and rhombohedral phases. Samara reported that KTN with small Nb content ($x < 0.02$) exhibit relaxational glass-like behavior rather than a ferroelectric structural phase transition.[39] Moreover, the KTN with $x = 0.02$ i.e., KTN/0.02 did not exhibit any frequency dispersion unless subject to high pressure.[39] However, the diffuse ferroelectric phase transition KTN/0.02 crystal was observed by refractive index and linear birefringence measurements.[40] On the other hand, Toulouse *et al*. observed the structural phase transition and existence of polar nanoregions (PNRs) well above T_C of KTN/0.012 crystal by dielectric, polarization, and Raman measurements.[41] An inelastic light scattering study also revealed the presence of PNRs in KTN/0.09 crystal, which led to the relaxor-like nature of the KTN/0.09 crystal.[42] Recently, the relaxor-like behaviors of a high quality KT/0.32 single crystal were observed by the observation of the Burns temperature, $T_B \sim 620$ K, at which the dynamic PNRs appear, and intermediate temperature, $T^* \sim 310$ K, indicating the begin of the PNRs rapid growth.[43] By the Brillouin scattering, the relaxor-like dynamics in the vicinity of a ferroelectric phase transition of the KTN/0.32 crystal were also studied.[44] Hence, there is a considerable debate on the optimum composition at which KTN crystal exhibit relaxor-to-normal crossover ferroelectric phase transition.

RFEs are characterized by the diffusive temperature dependence and the remarkable frequency dispersion of the dielectric properties. It is well known that such peculiar properties are attributed to PNRs related to random fields.[45] In ferroelectrics, the relaxor behavior results from the structural disorder.[46,47] The main structural disorder is the random occupation of different ions on a crystallographic equivalent site, a common origin of the relaxor nature in the RFEs. Heterovalency and the difference in the ionic radii of the B-site cations [e.g., Mg^{2+} and Nb^{5+} in $Pb(Mg_{1/3}Nb_{2/3})O_3$, PMN] can lead to the formation of random fields related to chemical order region (COR) and PNRs.[48] RFEs also typically exhibit three characteristic temperatures known as the Burns temperature, T_B, the intermediate temperature, T^*, and the freezing temperature, T_f.[12,39,45,49] It is believed that the T_B is associated with the start of the formation of dynamical PNRs, the T^* corresponds to the temperature at which dynamic to static transition of PNRs begins, and the T_f corresponds to the temperature at which PNRs percolate into a ferroelectric state. In spite of many experimental[50-54] and theoretical efforts including the random field model,[55] the dipole glass model,[49] and the spherical random-bond-random-field model[56] carried out to date on relaxors, the exact knowledge of the static and the dynamical aspect of PNRs is far from completely understood. However, in the case of KTN, the two B-site cations are homovalent and their raddi are similar. In KTN, the Nb ions at the B-site go off-center, and therefore they induce PNRs.[57] By the X-ray absorption fine structure (XAFS) measurement, the Nb ions in KTN crystals were found to occupy one of eight off-center positions along the equivalent [111] direction.[58] The microscopic origin of the off-centering of Nb was rationalized by the pseudo Jahn-Teller effect (PJTE).[59] Based on the comparison with lead-based RFEs, which are highly complex, presenting both chemical and structural local order, KTN exhibits relaxor-like properties, but much less complicated than the lead-based RFEs.[41,43,60] Therefore, KTN is better suited for the investigation of the fundamental origin and mechanism of the relaxor-like phenomenon as the case of mean random fields.

Recently, the Li-doping effect on the $KTaO_3$ is one of the interesting research fields in materials science. By the Li-doping to $KTaO_3$, the quantum paraelectricity was suppressed and ferroelectricity appeared.[61,62] However, in $K_{1-y}Li_yTaO_3$ (KLT) there is a crossover at around critical concentration y_C = 0.022 between a freezing and a structural transition with a critical level of local polarization.[61] Therefore, the Li-doped KTN is an intriguing topic to investigate the Li-doping effects on precursor dynamics and the related physical properties of a RFE phase transition. In addition, Zhou *et al*. reported the excellent piezoelectric response of a high quality Li-doped KTN single crystal.[25] The excellent piezoelectric properties indicate that the Li-doped KTN is a very promising lead free piezoelectric material for the applications to electromechanical devices such as transducers, actuators, and sensors.

Since the value of T_C near room temperature (RT) is highly desirable for integrated optics, therefore, it is necessary to investigate the KTN with the composition where T_C is close to RT. By inelastic light scattering, the dynamical aspect of PNRs was extensively studied in the cubic phase of KTN with compositions where T_C is far below from RT.[41,42,44,63] However, the study of the dynamical behaviors of PNRs in Nb rich KTN is rather scarce. Furthermore, the physical origin of the Fano resonance, a phenomenon which results from the interaction between a discrete state and continuum states showing an asymmetry of the spectral line shape, at around 196 cm^{-1} in KTN still remains unclear. Therefore, in this study, we aim to clarify the precursor dynamics and thus also related physical properties in high quality Nb rich not only KTN but also Li-doped KTN single crystals by Brillouin and Raman scattering. The comparative study between KTN and Li-doped KTN was performed to discuss the effect of Li-doping on PNRs and the lattice dynamical properties related to a RFE phase transition. The microscopic origin of the Fano resonance of Li-doped KTN crystals was discussed on the basis of the results of Raman scattering.

1.8 Major findings of this study

In this study, the high quality Nb rich KTN and Li-doped KTN crystals were investigated to clarify the elastic anomaly in the GHz range caused by the coupling of acoustic phonons and CPs with the dynamical PNRs and their slowing down. The thesis is composed of mainly four parts:

i) The experimental evidence of PNRs in Nb rich KTN and Li-doped KTN single crystals.
ii) The effects of Li-doping on PNRs and the related physical properties of a RFE phase transition.
iii) The discussion of the microscopic origin of the Fano resonance in Li-doped KTN single crystals.
iv) The effects of composition and defects on elastic properties of Li-doped KTN single crystals.

References

[1]Y. Xu, *Ferroelectric Materials and Their Applications*, (North-Holland, London, 1991).

[2]J. Valasek, Phys. Rev. **17,** 475 (1921).

[3]A. K. Muller and H. Thomas, *Structural Phase Transitions I,* (Springer-Verlag, Berlin and New York, 1981).

[4]R. E. Newnham, *Properties of Materials: Anisotropy, Symmetry, Structure* (Oxford, New York, 2005).

[5]G. H. Haertling, *Piezoelectric and Electroptic Ceramics in Ceramic Materials for Electronics: Processing, Properties and Application*, R. C. Buchanan ed. (Dekker, New York, 1986).

[6]B. Jaffee, W. R. Cook, and H. Jaffee, *Piezoelectric Ceramics*, (London and New York, 1971).

[7]J. F. Nye, *Physical Properties of Crystals*, (Clarendon press, Oxford, 1957)

[8]M. E. Lines and A. M. Glass: *Principles and Applications of Ferroelectrics and Related Materials*, (Clarendon press, Oxford, 1977).

[9]I. Rivera, A. Kumar, N. Ortega, R. S. Katiyar, and S. Lushikov, Solid State Commun. **149**, 172 (2009).

[10]U. Kaatze, Metrologia **47,** S91 (2010).

[11]A. A. Bokov and Z.-G. Ye, Solid State Commun. **116,** 105 (2000).

[12]G. Burns and F. H. Dacol, Phys. Rev. B **28,** 2527 (1983).

[13]G. Burns and F. H. Dacol, Slid State Commun. **48,** 853 (1983).

[14]G. Burns and F. H. Dacol, Slid State Commun. **58,** 567 (1983).

[15]G. A. Samara, J. Phys.: Condens. Matter **15,** R367 (2003).

[16]D. Viehland, Z. Xu, and D. A. Payne, J. Appl. Phys. **74,** 7454 (1993).

[17]L. D. Landau, Phys. Z. Sowjetunion **11,** 26 (1937).

[18]V. L. Ginzberg, Zh. Eksp, and T. Fiz, **15,** 739 (1945).

[19]A. F. Devonshire, Philos. Mag. **40,** 1040 (1949).

[20]A. F. Devonshire, Adv. Phys. **3,** 85 (1954).

[21]T. Mitsui, I. Tatsuzaki, and E. Nakamura, *An Introduction to the Physics of Ferroelectrics* (Gordon and Breach, London, 1976).

[22]Y. C. Chang, C. Wang, S. Yin, R. C. Hoffman, and A. G. Mott, Opt. Lett. **38,** 4574 (2013).

[23] H. Tian, B. Yao, C. Hu, X. Meng, and Z. Zhou, Appl. Phys. Express **7,** 062601 (2014).

[24]H. Tian, C. Hu, Q. Chen, and Z. Zhou, Mater. Lett. **68,** 12 (2012).

[25] Z. Zhou, J. Li, H. Tian, Z. Wang, Y. Li, and R. Zhang, J. Phys. D: Appl. Phys. **42,** 125405 (2009).

[26]S. E. Park and T. R. Shrout, J. Appl. Phys. **82,** 1804 (1997).

[27]R. Zhang, B. Jiang, and W. Cao, J. Appl. Phys. **90,** 3471 (2001).

[28]A. B. Ustinov, G. Srinivasan, and Y. K. Fetisov, J. Appl. Phys. **103,** 063901 (2001).

[29]A. Agranat, R. Hofmeister, and A. Yariv, Opt. Lett. **17,** 713 (1992).

[30]J. E. Geusic, S. K. Kurtz, L. G. Van Uitert, and S. H. Wemple, Appl. Phys. Lett. **4,** 141 (1964).

[31]F. S. Chen, J. E. Geusic, S. K. Kurtz, J. G. Skinner, and S. H. Wemple, J. Appl. Phys. **37,** 388 (1966).

[32]A. J. Fox, Appl. Opt. **14,** 343 (1975).

[33]S. Yagi, K. Naganuma, T. Imai, Y. Shibata, J. Miyazu, M. Ueno, Y. Okabe, Y. Sasaki, K. Fujiura, M. Sasaura, K. Kato, M. Ohmi, and M. Haruna, Proc. SPIE **8213,** 821333 (2012).

[34]T. Imai, S. Yagi, S. Toyoda, J. Miyazu, K. Naganuma, M. Sasaura, and K. Fujiura, Appl. Phys. Express **4,** 022501 (2011).

[35]Y. Sasaki, Y. Okabe, M. Ueno, S. Toyoda, J. Kobayashi, S. Yagi, and K. Naganuma, Appl. Phys. Express **6,** 102201 (2013).

[36]R. P. Lowndes and A. Rastogi, J. Phys. C **6**, 932 (1973).

[37]S. Triebwasser, Phys. Rev. **114**, 63 (1959).

[38]D. Rytz and H. J. Scheel, J. Cryst. Growth **59**, 468 (1982).

[39]G. A. Samara, Phys. Rev. Lett. **53,** 298 (1984).

[40]W. Kleemann, F. J. Schafer, and D. Rytz, Phys. Rev. Lett. **54,** 2038 (1985).

[41]J. Toulouse, P. DiAntonio, B. E. Vugmeister, X. M. Wang, and L. A. Knauss, Phys. Rev. Lett. **68,** 232 (1985).

[42]Y. Yacoby, Z. Physik B **31,** 275 (1978).

[43]E. Dul'kin, S. Kojima, and M. Roth, Euro. Phys. Lett. 97, 57004 (2012).

[44]R. Ohta, J. Zushi, T. Ariizumi, and S. Kojima, Appl. Phys. Lett. 98, 092909 (2011).

[45]A. A. Bokov and Z.-G. Ye, J. Mater. Sci. **41,** 31 (2006).

[46]L. E. Cross, Ferroelectrics **76,** 241 (1987).

[47]G. A. Samara, Ferroelectrics **117,** 347 (1991).

[48]D. Phelan, C. Stock, J. A. Rodriguez-Rivera, S. Chi, J. Leão, X. Long, Y. Xie, A. A. Bokov, Z.-G. Ye, P. Ganesh, and P. M. Gehring, Proc. Natl. Acad. Sci. U.S.A. **111,** 1754 (2014).

[49]D. Viehland, S. J. Jang, L. E. Cross, and M. Wuttig, J. Appl. Phys. **68,** 2916 (1990).

[50]F. M. Jiang and S. Kojima, Phys. Rev. B **62,** 8572 (2000).

[51]S. Kojima and J.-H. Ko, Curr. Appl. Phys. **11,** S22 (2011).

[52]V. Sivasubramanian, S. Tsukada, and S. Kojima, J. Appl. Phys. **105,** 014108 (2009).

[53]S. Kojima, S. Tsukada, Y. Hidaka, A. A. Bokov, and Z.-G. Ye, J. Appl. Phys. **109,** 084114 (2011).

[54]J. Toulouse, F. Jiang, O. Svitelskiy, W. Chen, and Z.-G. Ye, Phys. Rev. B **72,** 184106 (2005).

[55]V. Westphal, W. Kleemann, and M. D. Glinchuk, Phys. Rev. Lett. **68,** 847 (1992).

[56]R. Pirc and R. Blinc, Phys. Rev. B **60,** 13470 (1999).

[57]J. P. Sokoloff, L. L. Chase, and L. A. Boatner, Phys. Rev. B **41,** 2398 (1990).

[58]O. Hanske-Petitpierre, Y. Yacoby, J. Mustre de Leon, E. A. Stern, and J. J. Rehr, Phys. Rev. B **44**, 6700 (1991).

[59]V. Polinger, Chem. Phys. **459,** 72 (2015).

[60]L. A. Knauss, X. M. Wang, and J. Toulouse, Phys. Rev. B **52,** 13261 (1995).

[61]L. Cai, J. Toulouse, L. Harrier, R. G. Downing, and L. A. Boatner, Phys. Rev. B **91,** 134106 (2015).

[62]H. Schremmer, W. Kleemann, and D. Rytz, Phys. Rev. B **62,** 1896 (1992).

[63]O. Svitelskiy and J. Toulouse, J. Phys. Chem. Solids **64,** 665 (2003).

Chapter 2

Inelastic Light Scattering and Dielectric Spectroscopy

2.1 Light scattering

In materials, light is scattered by the fluctuations in the dielectric tensor. The fluctuations of certain physical quantities are coupled to the fluctuations in the dielectric tensor. In the vicinity of the phase transitions, the fluctuations of some physical quantities become significant and give some useful informations regarding the dynamical aspect of structural phase transition. Thus, the light scattering is a powerful tool for the investigation of the structural phase transitions phenomena. The measured integrated scattered intensity provides essential information in connection to the total fluctuation of the appropriate physical quantity that coherently related to the phase transition. On the other hand, the measurements of the peak frequency and line width of the spectral power density yield information about the structure and dynamics of the solid undergoing the phase transition.[1-7]

In a light scattering experiment, an incident light having frequency ω_0 coming from an intense monochromatic light source, usually a laser, interacts with the collective excitations present in a medium, giving rise to scattered light with a spectral distribution of frequencies $\{\omega_S\}$ as shown in Fig. 2.1.

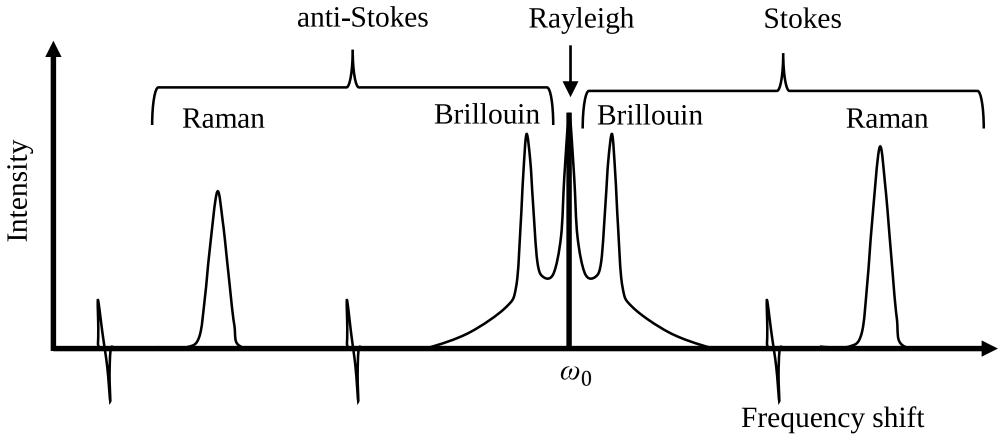

Fig. 2.1. Schematic diagram of a light scattering spectrum

In the center of the spectrum, the peak is the contribution of incident photons which have been elastically or quasi-elastically scattered with no change in frequency. The remaining peaks correspond to inelastic scattering and their shifts from ω_0 normally occur in two separate ranges of frequency. One is the Brillouin scattering component and other is the Raman scattering component (Fig. 2.1). The component of Brillouin scattering, resulting from sound waves, occurs close to the ω_0. The typical shifts of the Brillouin component are approximately at the range 3~30 GHz (0.1~1 cm^{-1}). The component of Raman scattering, resulting from the scattering of phonon by internal vibrations of molecules or optic vibrations in crystals, lies at higher shifts, normally is in the range of 10~4000 cm^{-1}. The inelastic light scattering spectrum is subdivided into two events namely Stokes (energy-loss) and anti-Stokes (energy-gain) related to the creation and annihilation of the excitation quanta.

The kinematics of light scattering can be derived from either a quantum mechanical or classical point of view. Classically, It is imagined that each lattice vibration, ($\mathbf{q}$, ω) perturbs the dielectric constant, ε, in such a way that it can be expressed by the following relation:[8]

$$\varepsilon = \varepsilon_0 + \sum\nolimits_{q,\omega} \varepsilon_{k\omega} \exp i\Big(\mathbf{q}\cdot\mathbf{r}\text{-}\omega t\Big) = \varepsilon_0+\delta\varepsilon \tag{2.1}$$

or in the tensor form

$$\varepsilon_{\mathrm{ij}}(\mathbf{r},t) = \hat{e}_{\mathrm{i}}\cdot\boldsymbol{\varepsilon}(\mathbf{r},t).\hat{e}_{\mathrm{j}} = \varepsilon^{0}_{\mathrm{ij}}+\delta\varepsilon_{\mathrm{ij}}(\mathbf{r},t) \tag{2.2}$$

When a plane of monochromatic light wave $E(\mathbf{r},t) = E_0 \exp i\,\left(\mathbf{k}_0\cdot\mathbf{r}\text{-}\omega_0 t\right)$ transverses through the crystal, there will be an “excess polarization” $\delta p_{\mathrm{ij}} = \delta\varepsilon_{\mathrm{ij}}E_0/4\pi$, that will give rise to a scattered field $E_{\mathrm{s}}(\mathbf{r},t)$. This scattered field can be expressed in the following form

$$E_{\mathrm{s}}(\mathbf{r},t) = \delta\varepsilon_{\mathrm{ij}}(\mathbf{r},t)\propto \sum\nolimits_{k,\omega_q} \exp i\,[\mathbf{k}_{\mathrm{s}}\cdot\mathbf{r}\text{-}\big(\omega_0\mp\omega_{\mathrm{q}}\big)t]\int_V \exp i\,\big(\mathbf{k}_0\mp\mathbf{q}\text{-}\mathbf{k}_{\mathrm{s}}\big).\mathbf{r}'\mathrm{d}V' \tag{2.3}$$

The volume integral in Eq. (2.3) gives a δ-function in ($\mathbf{k}_0\mp\mathbf{q}\text{-}\mathbf{k}_{\mathbf{s}}$), that imposes wave vector conservation. Therefore, there are 3sN normal modes in a crystal, where s is the number of atoms in the unit cell and N is the number of unit cell. The kinematically 3s of the (one on each branch) can produce scattering of light of frequency ω_0 in a given direction. Thus, the scattered field will consist of components at $\omega_0\mp\omega_{\mathrm{q}}$ where ω_{q} are the 3s frequencies at which a vertical line at $|\mathbf{q}| = \left|\mathbf{k}_0\text{-}\mathbf{k}_{\mathrm{s}}\right| \approx 2|\mathbf{k}_0|\sin\frac{1}{2}\varphi$ intersects the 3*s* branches of the dispersion curve.

It is significant to decompose $\delta\varepsilon_{\mathrm{ij}}(\mathbf{r},t)$ in terms of Fourier components in frequency ω and in wave vector $\mathbf{q}$ according to

$$\delta\varepsilon_{\mathrm{ij}}(\mathbf{q},\omega)=\frac{1}{2\pi V}\iint_{-\infty}^{\infty}\delta\varepsilon_{\mathrm{ij}}(\mathbf{r},t)\exp(i\mathbf{q}.\mathbf{r}\text{-}i\omega t)\,d^3\mathbf{r}dt$$

$$=\frac{1}{2\pi}\int_{-\infty}^{\infty}\delta\varepsilon_{\mathrm{ij}}(\mathbf{q},t)\mathrm{e}^{-i\omega t}dt \tag{2.4}$$

From the second-quantized theory of lattice dynamics, the same results are obtained and each normal mode $\{\mathbf{q},\omega\}$ is described in terms of a number of quanta (phonons) of energy of $\hbar\omega$ and crystal momentum $\hbar\mathbf{q}$. A light scattering event is produced by the creation or annihilation of a phonon as depicted in Fig. 2.2.

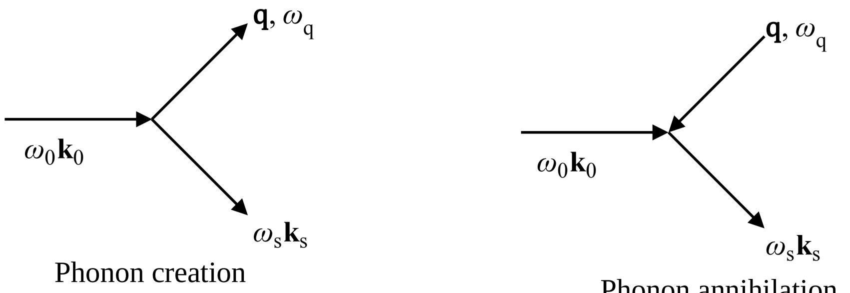

Phonon creation
(Stokes event)

Phonon annihilation
(anti-Stokes event)

Fig. 2.2. Typical diagram for the first order photon-phonon scattering.

The conservation of momentum and energy between the photons and phonons yields for Stokes event

$$\mathbf{k}_{\mathrm{s}} = \mathbf{k}_0\text{-}\mathbf{q} \tag{2.5}$$

$$\omega_{\mathrm{s}} = \omega_0 - \omega_{\mathrm{q}}$$

For anti-Stokes event

$$\mathbf{k}_{\mathrm{s}} = \mathbf{k}_0 + \mathbf{q}$$
$$\omega_{\mathrm{s}} = \omega_0 + \omega_{\mathrm{q}} \qquad (2.6)$$

The spectral power density of the scattered light is obtained from Eq. (2.4) by

$$I_{\mathrm{ij}}(\mathbf{q},\omega) \propto \left|\delta\varepsilon_{\mathrm{ij}}(\mathbf{q},\omega)\right|^2 \propto \frac{1}{2\pi}\int_{-\infty}^{\infty} dt\, \mathrm{e}^{-i\omega t} \langle\delta\varepsilon_{\mathrm{ij}}(\mathbf{q},t)\delta\varepsilon_{\mathrm{ij}}(\mathbf{q},0)\rangle$$
$$\propto [n(\omega)+1]\mathrm{Im}\delta\chi_{\mathrm{ij}}(\mathbf{q},\omega) \qquad (2.7)$$

In Eq. (2.7), the second identity is the result of the Wiener-Khinchine theorem and the angle brackets represent ensemble (thermal) average. The third identity is the fluctuation-dissipation theorem, where χ_{ij} is the dielectric susceptibility, $n(\omega)$ is the Bose-Einstein population factor and is given by $n(\omega) = \frac{1}{\exp\left(\frac{\hbar\omega}{k_{\mathrm{B}}T}\right)-1}$, in which k_{B} is the Boltzmann constant and $\hbar$ is the Dirac constant.

It is readily seen from Eq. (2.7) that the spectral power density of scattered light is proportional to the Furier transform of the time correlation function of the fluctuation of the dielectric tensor $\delta\varepsilon_{\mathrm{ij}}(\mathbf{q},t)$. Therefore, the mechanism underlying the phase transition in solids is contained in the time correlation function $\langle\delta\varepsilon_{\mathrm{ij}}(\mathbf{q},t)\delta\varepsilon_{\mathrm{ij}}(\mathbf{q},0)\rangle$. The order parameter, polarization P in the case of ferroelectric materials, can be approximately characterized by two quantities the coherence length and the correlation time. It is important to note that the spectral intensity is proportional to the imaginary part of the dielectric susceptibility. It is very useful when analyze a spectrum.

2.2 Brillouin scattering

2.2.1 General theory of Brillouin scattering

Since the values of the wave vector **q** are very small, the components due to the acoustic modes, which are measured by the Brillouin scattering, appear at frequencies very much lower than those of optic modes. The optic modes are measured by Raman scattering spectra. The main difference between Brillouin and Raman scattering comes from the dispersion relation of the quasi-particle generated. We talk about a Brillouin process if the frequency is zero for $\mathbf{q} = 0$ and about a Raman process if $\omega(\mathbf{q} = 0) \neq 0$. Since the long wavelength acoustic modes involve in-phase motion of all atoms in the unit cell, the atomic displacements are almost constant over the distances on the order of ≈ 100 unit cell, so that one may discuss these modes in terms of an elastic continuum model.

In Brillouin scattering, the Stokes and anti-Stokes doublet symmetrically positioned about the unshifted line occur as a result of the Bragg-like scattering by propagating sound waves in a solid. The condition of Bragg-like scattering can be expressed as

$$\lambda = 2\Lambda \sin\frac{\phi}{2}$$

where λ is the wavelength of the light in the medium, ϕ is the scattered angle and Λ is the wavelength of the propagating sound wave. The Brillouin scattering components are then as result of a Doppler shift $\Delta\omega$

give rise to the movement of the atomic grating via sound wave propagation. Thus, the $\Delta\omega$ is then given by

$$\Delta\omega = \omega_s - \omega_0 = \pm 2\frac{cv\omega_0}{n}\sin\frac{1}{2}\phi$$

$$= \pm 2\, vn|\mathbf{k}_0|\sin\frac{1}{2}\phi = \pm 4\,\frac{\pi n}{\lambda_0}v\,\sin\frac{1}{2}\phi \qquad (2.8)$$

where ω_0 and ω_s are the frequency of the incident and scattered light, respectively. n is the refractive index of the medium and $\mathbf{k}_0$ is the wave vector of the incident light. In 1922, Brillouin was first derived the Eq. (2.8) and shows that the frequency shifts are linear function of $\sin\frac{1}{2}\phi$, and a maximum shift is obtained for back scattering geometry ($\phi = \pi$).

In the long wavelength limit, for a particular **q**, the polarization and frequencies of the three acoustic modes are estimated by the elastic constants C_{iklm} through the equation of motion;

$$\rho\dot{\mathbf{u}} = C_{iklm}\frac{\partial^2\mathbf{u}_m}{\partial\mathbf{r}_k\partial\mathbf{r}_l}\ , \qquad (2.9)$$

where $\mathbf{u}(\mathbf{r},t)$ is the local displacement vector. The solution of Eq. (2.9) is considerably simplified by the restrictions placed on the elastic constants by crystal symmetry.[9] The plane wave solutions to Eq. (2.9) can be found for a given **q**, and one can be obtained 3 modes, usually of mixed polarization. One can find pure one longitudinal mode and two pure transverse modes only for special directions of **q**.

The optical coupling between dielectric tensor and strain can be solved completely in terms of the Poockel's elasto-optic or photoelastic constants P_{mn}.[9] In 6-component notation, the reciprocal dielectric tensor B_{m} is distorted by the strain field X_{n} following $\Delta B_m = P_{mn}X_n$. However, in Brillouin scattering, the $\mathbf{q}\rightarrow 0$ limit of the acoustic modes correspond to rigid translation of the crystal as a whole, and cannot perturb the dielectric constant. The Brillouin effect is only observed in the limit $\mathbf{q} \neq 0$. As a result, unlike the Raman scattering, the Brillouin scattering tensors will depend on the direction of **q** as well as $\boldsymbol{E}_0$ and $\boldsymbol{E}_{\mathrm{s}}$. Thus, we cannot generate a single set of scattering tensors comparable to Raman scattering tensors, but are compelled to calculate the scattering tensors for every direction of **q**. The Brillouin scattering tensors for all crystal in different directions of **q** were reported in Ref. 10.

2.2.2 Brillouin scattering tensors and selection rules

Assuming plane wave solutions of the form $\mathbf{u}_i = \mathbf{u}_i^0\exp i(\mathbf{q}\cdot\mathbf{r} - \omega t)$, and substituting it into the Eq. (2.9) leads to

$$\left[C_{iklm}\mathbf{q}_k\mathbf{q}_l - \rho v^2\delta_{im}\right]\mathrm{u}_m^0 \qquad (2.10)$$

Eqs. (2.10) have non-trivial solutions only if the secular determinant vanishes

$$\left|C_{iklm}\mathbf{q}_k\mathbf{q}_l - \rho v^2\delta_{im}\right| = 0$$

where $\mathbf{q}_k$ and $\mathbf{q}_l$ are the components of **q**. If the elastic constants, C_{iklm} of a crystal are known, then the Eq. (2.10) can be solved for any direction of **q**, and will give three eigenvalues of velocity v_{i} (i = 1 ,2, 3). Each v_{i} can be put back into Eq. (2.10), and displacement eigenvectors associated with each v_{i} can be obtained.

If **q** is chosen in a high symmetry direction, then the displacement eigenvectors will be perpendicular or parallel to **q**, corresponding to two transverse (T) and one longitudinal (L) modes. The displacement vectors can be neither perpendicular nor parallel to **q** for general **q-**directions results in mixed polarization modes. The mixed polarization modes are indicated by the QT (quasi-transverse) or the QL (quasi-longitudinal) to show that displacement vector is more nearly perpendicular or parallel to **q**.

In the long wavelength limit, the distortion of the local dielectric constant is induced by the local strain through the elasto-optic or photoelastic effect. The multiplication of the 6-component stain by the 6 × 6 Pockel's tensor gives a 6-component ΔB that can be converted to 3 × 3 form $\Delta B_{\alpha\beta}$. If the xyz-axes are chosen to correspond to the principle axes of the dielectric tensor, then the ΔB_{ij}, which are related to change in the dielectric tensor $\varepsilon_{\mathrm{ij}}$, can be expressed as:[8]

$$\delta\varepsilon_{\mathrm{ij}} = -\varepsilon_{0\mathrm{ii}}\varepsilon_{0\mathrm{jj}}\Delta B_{\mathrm{ij}} \tag{2.11}$$

Therefore, one can obtain the distortion in the dielectric tensor produced by an acoustic wave by a tensor

$$\left\lfloor \delta\varepsilon_{\mathrm{ij}} \right\rfloor = \mathbf{qu}\boldsymbol{T} \tag{2.12}$$

where the element T_{ij} of the tensor $\boldsymbol{T}$ is $\varepsilon_{\mathrm{ii}}\varepsilon_{\mathrm{jj}}$ times $\Delta B_{\mathrm{ij}}/\mathbf{qu}$. The Rayleigh ratio (differential cross section per unit volume) is derived from the excess dipole moment per unit volume $p_{\mathrm{i}}(\mathbf{r}) = \delta\varepsilon_{\mathrm{ij}}E^0_{\mathrm{j}}/4\pi$. If we assume that the excitation of each acoustic mode is in thermal equilibrium at temperature T, then:

$$<(\mathbf{qu})^2> = k_B T/2V\rho v^2 \tag{2.13}$$

Therefore, for the Rayleigh ratio of the jth acoustic mode (j = 1,2,3) with velocity v_{j}, assuming e_0 and e_{s} be unit vectors in the direction of the polarization of the incident and scattered fields,[5,11,12] we have

$$R^{\mathrm{j}} = \frac{kT\pi^2}{2\lambda_{\mathrm{s}}^4\rho v_{\mathrm{j}}^2}\left[e_{\mathrm{s}}.T^{\mathrm{j}}.e_0\right]^2\left(\frac{n_{\mathrm{s}}}{n_0}\right), \tag{2.14}$$

where λ_{s} is the wavelength of the scattered light.

For scattering geometries in which sound waves propagate in high symmetry directions, however, the structure of the ***T***-tensors is sufficiently simple so that selection rules can be deduced without specifying the numerical values of the elastic constants. The scattering tensors for a number of high symmetry directions in each of the crystal classes have been competed previously in the literature.[5,7,13]

2.3 Raman scattering

In crystals, Raman scattering is induced owing to the fluctuations of polarizability tensor $\alpha_{\mathrm{ij}}(\mathbf{r},\mathrm{t})$ or dielectric permeability $\Delta\varepsilon_{\mathrm{ij}}(\mathbf{r},\mathrm{t})$ modulated by the lattice vibrations.[6,14] The vibrations of lattice can be described in terms of phonon energy, $\hbar\omega$, and momentum, $\hbar\mathbf{q}$. Due to the translational symmetry, the wave vector **q** of lattice vibrations can take only N discrete values for a crystal with N unit cells and s atoms in each unit cell. According to lattice dynamics, there are 3s normal modes each of them is a linear superposition of 3s Cartesian displacements of atoms in the unit cell for each value of **q**.[6,8] In the midst of the 3s normal modes, 3 are acoustic modes and the left 3s-3 are optic modes. Depending on the energy state of the molecule, Raman scattering can be described by Jablonski diagram as shown Fig. 2.3. When light interacts with the molecule and distorts the electron clouds around the nuclei to form a short lived high energetic complex state (virtual sate). When this occurs, there are the three potential outcomes.

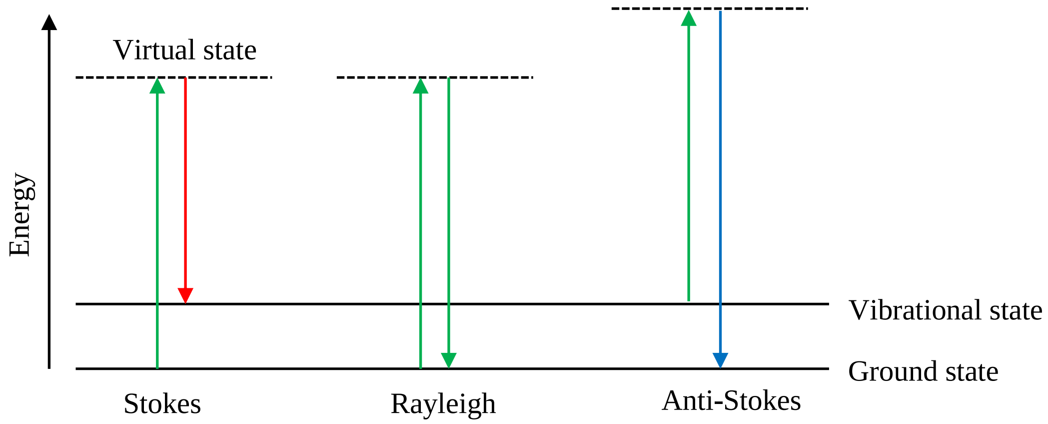

Fig. 2.3. Jablonski diagram showing the transition of energy for Raleigh and Raman scattering.

First, the molecule is initially in its ground state. After excitation, the molecule can relax back down to the ground state and emit a photon of equal energy to that of the incident photon; this scattering process is regarded as an elastic process and is also referred to as Rayleigh scattering. Second, the molecule is initially in its ground state. After excitation, the molecule can relax to a real phonon state and emit a photon with less energy than the incident photon; this scattering process is referred as Stokes scattering. The third potential outcome is that the molecule, already in an excited phonon state, is excited to a higher virtual state, and then relaxes back down to the ground state emitting a photon with more energy than the incident photon; this scattering process is called anti-Stokes scattering.

Based on the quantum theory of dispersion, Placzek has given a rigorous theory of the Raman effect. The light scattering process can be visualized as the absorption of an incident photon of frequency ω_0 by a molecule in a given initial state, thus raising the molecule to a “virtual” state from which it immediately returns to a final state emitting the scattered photon. As the polarizability α_{ij} relates an electric field to a polarization by $P_\mathrm{i} = \alpha_\mathrm{ij} E_\mathrm{j}$, and the polarizability α_ij can be expanded in a power series of normal coordinates:[14]

$$\alpha_\mathrm{ij} = \left[\alpha_\mathrm{0j}\right]_0 + \sum_k \left[\frac{\partial \alpha_\mathrm{ij}}{\partial Q_k}\right]_0 Q_\mathrm{k} + \sum_{k,l} \left[\frac{\partial^2 \alpha_\mathrm{ij}}{\partial Q_k \partial Q_l}\right]_0 Q_k Q_l + \ldots \qquad (2.15)$$

where Q_k and Q_l are normal coordinates. By ignoring the tensor notation and writing the time dependence of phonon modes as $\cos \omega_\mathrm{q} t$, $\alpha = \alpha_0 + A \cos \omega_\mathrm{q} t$ for the first terms. Thus, under the electric field of the incident light with frequency ω_0, the polarization can be expressed as:

$$P = \left(\alpha_0 + A \cos \omega_\mathrm{q} t\right)\left(E_0 \cos \omega_0 t\right)$$

$$= \alpha_0 E_0 \cos \omega_0 t + \frac{1}{2} A E_0 \left[\cos\left(\omega_0 + \omega_\mathrm{q}\right) t + \cos\left(\omega_0 - \omega_\mathrm{q}\right) t\right] \qquad (2.16)$$

The first term on the right hand side of the Eq. (2.16) causes emission at just the incident light frequency and is referred as the Rayleigh scattering or an elastic scattering, the two terms in the brackets will result in emission at ω_0-ω_q and ω_0+ω_q are known as Stokes and anti-Stokes radiation, respectively.

The experimentally confirmed laws of Raman scattering are as follows:

(a) The pattern of Raman lines are expressed as frequency shifts from the exciting line, and the shifts are independent of the exciting frequency.

(b) The pattern of Raman frequency shifts is symmetrical about the exciting line. However, the lines on the high-frequency side of the exciting line (anti-Stokes lines) are always less intense than the corresponding lines on the low-frequency side (Stokes lines). The ratio of the intensities of corresponding anti-Stokes and Stokes lines is $\frac{I_a}{I_s} = \exp(\frac{-\hbar\omega}{k_B T})$.

(c) A given Raman line shows a degree of polarization that depends both on the origin of the line and on the experimental arrangement.

2.3.1 Raman selection rules

The wave vector transfer of light scattering is $\mathbf{q} = \frac{4\pi n}{\lambda_0}\sin(\frac{\varphi}{2})$, that is the order of 105 cm^{-1}, while the phonon wave vector ranges (0, π/d) and π/d is typically of the order of 108 cm^{-1}. Thus, Raman scattering only measures phonons of wave vectors lying very close to the Brillouin zone center, Γ point (except second order scattering). Loudon[1] reviewed the Raman scattering theory and developed a level of Raman tensors for different crystal systems. The calculation of the magnitude of Raman scattering effect is very complicated. On the other hand, the selection rules can be obtained directly from the point symmetry of the crystal. We can use the susceptibility tensor χ_{ij} instead of the polarizability α_{ij} in the case of crystal. The susceptibility can then be extended with respect to the normal coordinates Q_k and one can be obtained in analogy with α_{ij} in[15]

$$\chi_{\mathrm{ij}} = \left(\chi_{0\mathrm{j}}\right)_0 + \sum_k \left[\frac{\partial\chi_{\mathrm{ij}}}{\partial Q_k}\right]_0 Q_k + \sum_{k,l}\left[\frac{\partial^2\chi_{\mathrm{ij}}}{\partial Q_k \partial Q_l}\right]_0 Q_k Q_l + \ldots \qquad (2.17)$$

where the sum runs over all normal coordinates. $\frac{\partial\chi_{\mathrm{ij}}}{\partial Q_k}$ is a component of the derived polarizability tensor, which is also known as the Raman tensor. Since every vibrational state must transform an irreducible representation of the crystal point group, and only those normal modes that transform as one of the six components of χ_{ij} will have a nonzero $\left[\frac{\partial\chi_{\mathrm{ij}}}{\partial Q_k}\right]_0$. Thus the Raman selection rules can be stated as[14]

A Raman mode of frequency ω will be allowed whenever the normal modes transforms as one or more of six symmetry terms $x_i x_j$, where $(1 \leq i, j \leq 3)$.

The character tables for the 32 crystallographic point groups are listed in elsewhere[5,9] from which one can easily find transformation properties of different irreducible representations. Therefore, Raman active modes and relative Raman tensor components can be selectively measured by choosing different scattering geometries. There are several ways to find the symmetry species for zone center phonons and one of the standard method is the factor group analysis method.[16,17]

2.4 Dielectric spectroscopy

For an isotropic and linear dielectrics, the time dependent dielectric displacement D(t) and polarization P(t) are related to the time dependent electric field E(t) through the susceptibility χ as:

$$D(\mathrm{t}) = \varepsilon E(\mathrm{t}), \qquad (2.18\mathrm{A})$$

$$P(t) = \chi E(t), \qquad (2.18\mathrm{B})$$

where $\varepsilon = 4\pi\chi+1$, is the dielectric permittivity. In the dynamical case, the dielectric displacements and polarization will cease when the frequency ω of the time dependent electric field of amplitude, E^0 [$E(\mathrm{t}) = E^0\cos\omega t$] is high enough, because the motions of the microscopic particles cannot follow the changes in the filed fast enough. In this case, $D(\mathrm{t})$ can also be described with ω, an amplitude, D^0, and a phase difference, δ, with respect to the electric field as:

$$D(\mathrm{t}) = D^0\cos\left(\omega t\text{-}\delta\right), \tag{2.19}$$

Thus, the value of phase difference changes by the variation of the frequency of the electric field. When the frequency is too low, δ becomes zero reaching to quasi-static state. The $D(\mathrm{t})$ can be divided into two parts, one in phase with $E(\mathrm{t})$ and other having a phase difference of $\pi/2$:

$$D(\mathrm{t}) = D^0\cos\delta\,\cos\omega t + D^0\sin\delta\,\sin\omega t, \tag{2.20}$$

defining $\cos\delta = \frac{\varepsilon'(\omega)E^0}{D^0}$, $\sin\delta = \frac{\varepsilon''(\omega)E^0}{D^0}$, the $D(\mathrm{t})$ can be expressed as

$$D(t) \;=\; \varepsilon'(\omega)E^0\, cos\omega t + \varepsilon''(\omega)E^0\, sin\omega t \tag{2.21}$$

where $\varepsilon'(\omega)$ and $\varepsilon''(\omega)$ are the real and imaginary parts of the frequency dependent of the complex dielectric constants $\varepsilon^*(\omega)$. Equations (2.20) and (2.21) are equivalent if we take $D^0 = \sqrt{\varepsilon'^2+\varepsilon''^2}$ and $\tan\delta = \frac{\varepsilon''}{\varepsilon'}$. $\varepsilon'(\omega)$ is assumed the generalization of the dielectric permittivity for sinusoidally varying fields and $\varepsilon''(\omega)$ determines the energy loss in the dielectrics. The typical frequency dependent behavior of $\varepsilon'(\omega)$ and $\varepsilon''(\omega)$ for all polar compounds in condensed phase is displayed in Fig. 2.4.

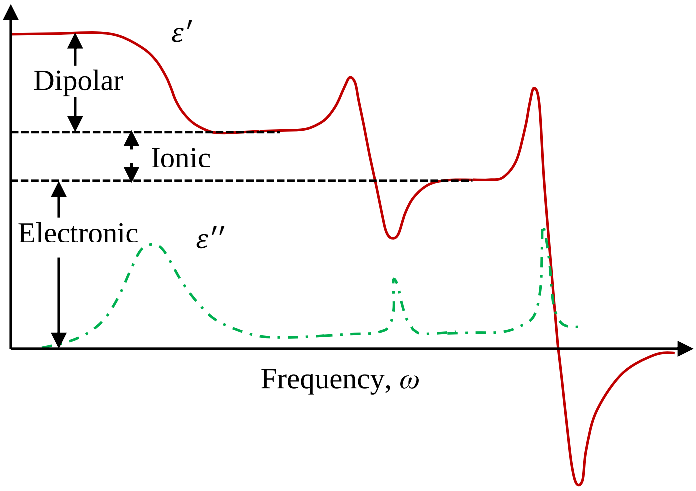

Fig. 2.4. Typical illustration of dielectric dispersion and loss tangent of polar compound.

In different frequency regions, the frequency dependence of the dielectric constant and loss factor are different. At low frequencies, $\varepsilon'(\omega)$ is equal to the static dielectric constant ε' and $\varepsilon''(\omega)$ is zero. As the frequency increases, $\varepsilon'(\omega)$ decreases rather slowly at first, whereas there are sharp increases followed by a decrease in the higher frequencies of the electromagnetic waves (IR, visible light, and UV). The $\varepsilon''(\omega)$ has peaks in the neighborhood of the frequencies where $\varepsilon'(\omega)$ changes. The non-equilibrium effects appearing with increase in frequency come from the electric polarization which is built up of three parts, the electronic, atomic, and orientation polarization, and each part corresponding with the motions of electrons, atoms, and molecules and ions, respectively, with different characteristic of times. In the orientationl polarization range, the broad absorption peaks (Fig. 2.4) indicates that no discrete energy level exist for the rotational motion of the molecules owing to manifold interactions. Owing to this reason, the orientationl polarization is characterized by the relaxation process and the induced polarization by a number of resonance process. The complex dielectric permittivity can be expressed in terms of relaxation (with relaxation time τ) as:

$$\varepsilon^{*}(\omega) = \varepsilon_{\infty} + \frac{\varepsilon\text{-}\varepsilon_{\infty}}{1+i\omega\tau} \tag{2.22}$$

with real and imaginary part as

$$\varepsilon'(\omega) = \varepsilon_{\infty} + \frac{\varepsilon\text{-}\varepsilon_{\infty}}{1+\omega^{2}\tau^{2}}\ , \tag{2.23}$$

$$\varepsilon''(\omega) = \frac{(\varepsilon\text{-}\varepsilon_{\infty})\omega\tau}{1+\omega^{2}\tau^{2}}\ , \tag{2.24}$$

To account for the broader peaks in $\varepsilon''(\omega)$ more realistically, it is considered that different parts of the orientational polarization decline with the distribution of relaxation times with the distribution function $g(\tau)$:

$$\varepsilon^{*} = \varepsilon_{\infty} + (\varepsilon\text{-}\varepsilon_{\infty}) \int_{0}^{\infty} \frac{g(\tau)d\tau}{1+i\omega\tau}\ , \tag{2.25}$$

with

$$\int_{0}^{\infty} g(\tau)d\tau = 1\ , \tag{2.26}$$

The presence of the dielectric dispersion in the complex dielectric response is one of the important signatures of the relaxor ferroelectric materials. Therefore, the study of dielectric properties is very important to clarify the relaxor nature of the relaxor ferroelectric materials.

In this study, the complex dielectric constant was measured using a home-made furnace and an impedance/gain-phase analyzer (SI 1260). The dielectric properties were also studied using a LCR meter (Agilent 4263B).

2.5 Instrumentation of inelastic light scattering

2.5.1 Brillouin scattering spectroscopy

2.5.1.1 Properties of Fabry-Perot interferometer

In 1899, C. Fabry and A. Perot designed the Fabry-perot interferometer (FPI) with a significant improvement over the Michelson interferometer. The FPI is used when a high resolution spectroscopy where a resolution of MHz to GHz is required. The FPI consists of two plane mirrors, mounted accurately parallel to one another, with an optical spacing L_1 between them. For a given L_1, the interferometer will transmit only certain wavelengths λ as defined by

$$T = \frac{\tau_{0}}{1+\left(\frac{4F^{2}}{\pi^{2}}\right)\sin^{2}\left(\frac{2\pi L_{1}}{\lambda}\right)}\ , \tag{2.27}$$

where τ_0 (< 1) is the maximum possible transmission determined by losses in the system, and F, the finesse, is a quality factor depending primarily on the flatness and mirror reflectivity. Equation (2.27) shows that only those wavelengths satisfying

$$L_1 = \frac{1}{2} m\lambda, \tag{2.28}$$

for integral values of *m*, can be transmitted. The condition is illustrated schematically in Fig. 2.5.

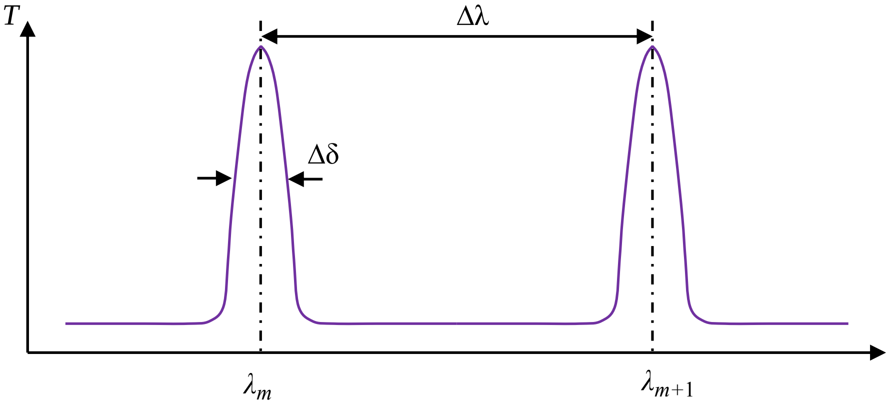

Fig. 2.5. Two successively transmitted wavelengths from a single FPI.

The finesse *F*, which is related to the spacing between successive transmitted wavelengths $\Delta\lambda$ (known as the free spectral range, FSR) and the width $\Delta\delta$ of a given transmission peak, can be expressed by the following relation:

$$F = \Delta\lambda / \Delta\delta, \tag{2.29}$$

Since the FPI is used as a spectrometer by varying the spacing L_1, therefore it can scan the light intensity at different wavelengths. However, at a given spacing, the measured intensity is the sum of the intensities at all wavelengths satisfying Eq. (2.28).

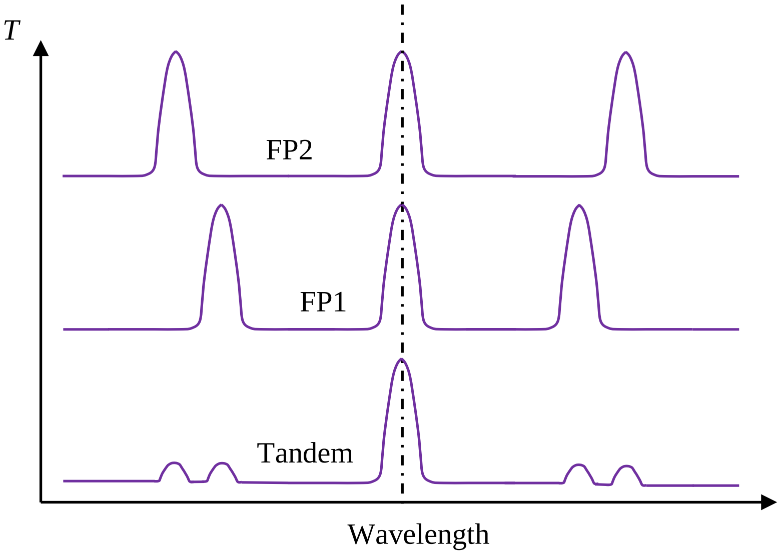

Fig. 2.6. The transmission properties of FP2 and FP1 and FPs in series.

Thus, an unambiguous interpretation of the spectrum is impossible unless it is known a priori that the spectrum of the light lies entirely within a wavelength spread $<\Delta\lambda$. It is true that since

$$\Delta\lambda = \lambda^2/2L_1 \qquad (2.30)$$

It is apparent from Eq. (2.30) that one may make $\Delta\lambda$ arbitrarily by decreasing L_1. However, $\Delta\delta$ increases proportional to $\Delta\lambda$ and so the resolution decreases. In fact Eq. (2.29) shows that the finesse F is just the ratio between FSR, $\Delta\lambda$ and the resolution $\Delta\delta$. In practice, due to limitations on the quality of mirror substrates and coatings, the F cannot be made much greater than about 100. Therefore, the relationship between FSR and resolution is fixed within limits determined by the achievable values of F.

2.5.1.2 Tandem interferometer

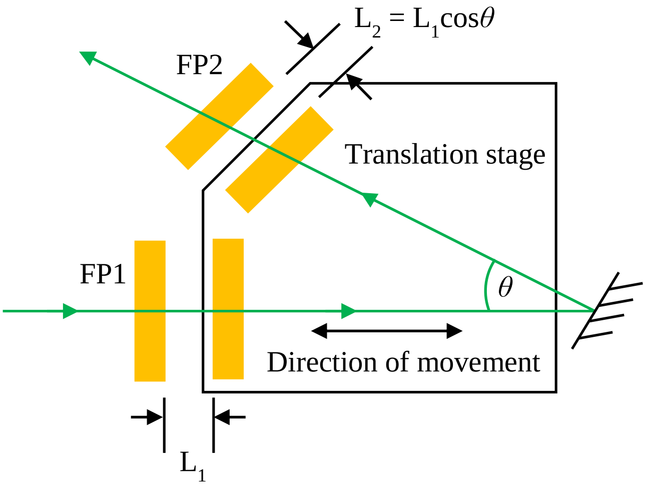

Fig. 2.7. A practical design of a tandem FP interferometer.

Based on the concept of a scanning stage, it is possible to improve the functionality of FPI by the combination of two interferometers on the single scanning stage to obtain both statically and dynamically stable synchronisation. The most useful arrangement is a Vernier system as shown in Fig. 2.7, where the spacing of the second interferometer L_2 is close to L_1. The wavelengths transmitted by the combination simultaneously satisfy the following condition

$$L_1 = \frac{1}{2}m\lambda \text{ and } L_2 = \frac{1}{2}n\lambda \qquad (2.31)$$

for integral values of m and n. The combined transmitted light passing successively through both FP1 and FP2 is illustrated in Fig. 2.6. in which the spacing L_1 and L_2 are independently set so as to transmit a given wavelength λ. The neighboring transmission peaks do not coincide; however, the FSR of FP1 do the transmission peaks coincide again after several times. Small "ghosts" of intervening transmission peaks remain since the transmission of either interferometer as show in Eq. (2.27) never falls exactly to zero. Therefore, the FSR of the tandem system is increased considerable factor over that of the single interferometer maintaining the similar resolution $\Delta\delta$. In order that the first ghost is not too noticeable one should chose L_1 and L_2 in a way that $F > L_1/(L_1\text{-}L_2)$. The optimum value of L_2/L_1 is around 0.95.

It is necessary to scan the two interferometers synchronously by changing the spacing L_1 and L_2 simultaneously to use the tandem interferometer system as a spectrometer. It is apparent from Eqs. (2.28) and (2.31) that to scan a given wavelength increment, the changes δL_1 and δL_2 must satisfy the condition as follows:

$$\frac{\delta L_1}{\delta L_2} = \frac{L_1}{L_2} \tag{2.32}$$

The magnitude of δL_1 and δL_2 are typically 1 to a few μm. The principle of the scanning tandem FP is seen in Fig. 2.7, which was designed by the Sandercock. The first interferometer FP1 is organized to lie in the direction of the movement of the translation stage, where one mirror sits on the translation stage and the other on a separate angular orientation device. The second interferometer FP2 lies with its axis at an angle θ to the direction of scan, where one mirror is mounted on the translation stage in close proximity to the mirror of FP1 and the other mirror for adjustment purposes. The relative spacing of the mirrors is set so that that the movement of the translation stage to the left would bring both sets of mirrors into simultaneous contact. On the other hand, the movement of the translational stage to the right sets the spacing to L_1 and $L_1\cos\theta$. Therefore, a scan of δL_1 of the translation stage produces a change of spacing δL_1 in FP1 and $\delta L_1\cos\theta$ in FP2. In other words, the two interferometers scan synchronously and Eq. (2.32) is satisfied.

2.5.1.3 Optical system for a Sandercock six pass tandem interferometer

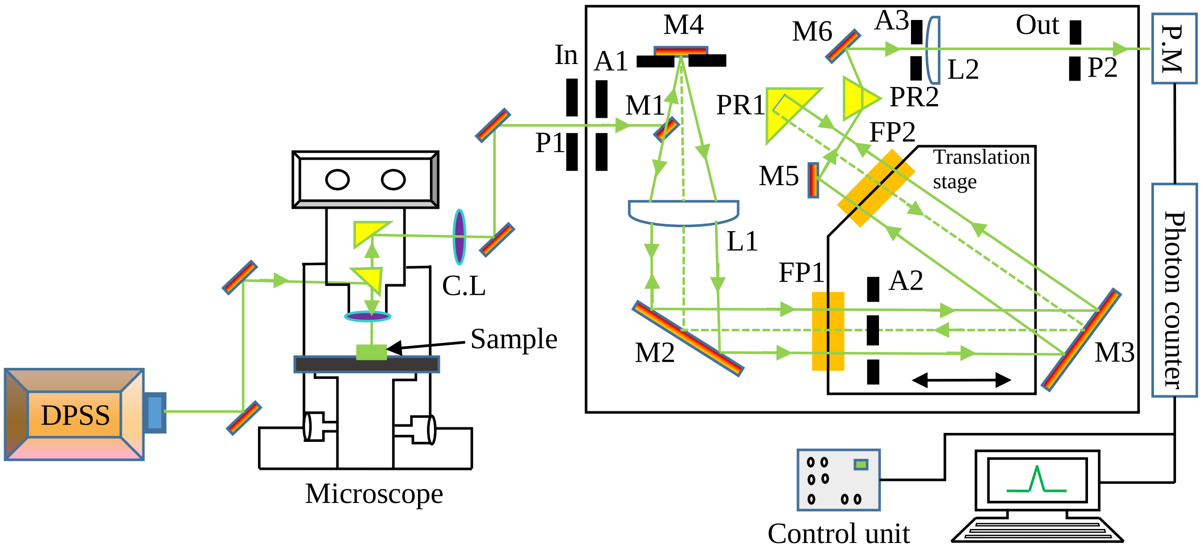

Fig. 2.8. Optics for a Sandercock 3+3 pass tandem interferometer equipped with microscope and photo multiplier.

The Optical arrangement, which was designed by Sandercock[18,19] using the combination of two interferometers FP1 and FP2, of Brillouin scattering experiment is illustrated in Fig. 2.8. In this study, an optical microscope is employed for backward scattering geometry. The diode pumped solid state (DPSS) laser with 532 nm wavelength is introduced into the optical microscope with the aid of small mirror to focus the sample. The scattered light is collected by the objective lens and enter into the FP interferometer through the adjustable pinhole P1. The aperture A1 then defines the cone of light which is accepted. The mirror M1 reflects the light towards the lens L1, and after the collimation, it redirects via mirror M2 to FP1. The redirected light is then passed through aperture 1 of the mask A2 and is directed via mirror M3 to FP2. After transmission through FP2, the light strikes the 90º prism PR1 and is reflected downwards and returned parallel to itself towards FP2 and it continues through the aperture 2 of A2 to FP1. After transmission through FP1, the light is passed through the lens L1 and underneath of the mirror M1, and is focused onto the mirror M4. The mirror M4 returns the light through lens L1, and after again collimation the light is directed to FP1 via the mirror M2. The combination of lens L1 and mirror M4 lying at its focus is known as a catseye, and is optically equivalent to a corner cube but has the advantage that it also acts as a spatial filter that removes undesirable beams such as the beams reflected from the rear surfaces of the interferometer mirrors. After the final pass through the interferometers, the light is directed to the prism PR2 via the mirror M5. The combination of prism PR2, lens L2, and the output pinhole P2 forms a bandpass filter with a width determined by the size of the pinhole. The mirror M6 sends the light onto the photomultiplier through the aperture A3, lens L2 and output pinhole P2. Finally, the scattered signal is recorded by a multichannel analyzer (MCA). In fact, every optical component including the two FPs inside the box of the interferometer has adjustable screws for convenient operation, we have thus followed the six pass light optics without explaining in detail of the optical adjustment. Special techniques such as stabilization, isolation vibration, and insurance of linear scan are employed and realized by the control unit.

2.5.2 Raman scattering

In Raman scattering experiments, the spectral dispersion is performed by a double or triple grating monochromator to enhance contrast so that Raman modes in the vicinity of the laser excitation frequency can be observed. The laser with high collimation and narrow bandwidth is used as a Raman excitation source, which provides much higher spectral source purity, intensity, polarization, and directionality. The detection of the dispersed component is usually done by a photon counting techniques with the aid of a photomultiplier (P.M) tube, and can achieve sensitivities on the order of one photon per second in the ultraviolet and visible spectral regions.

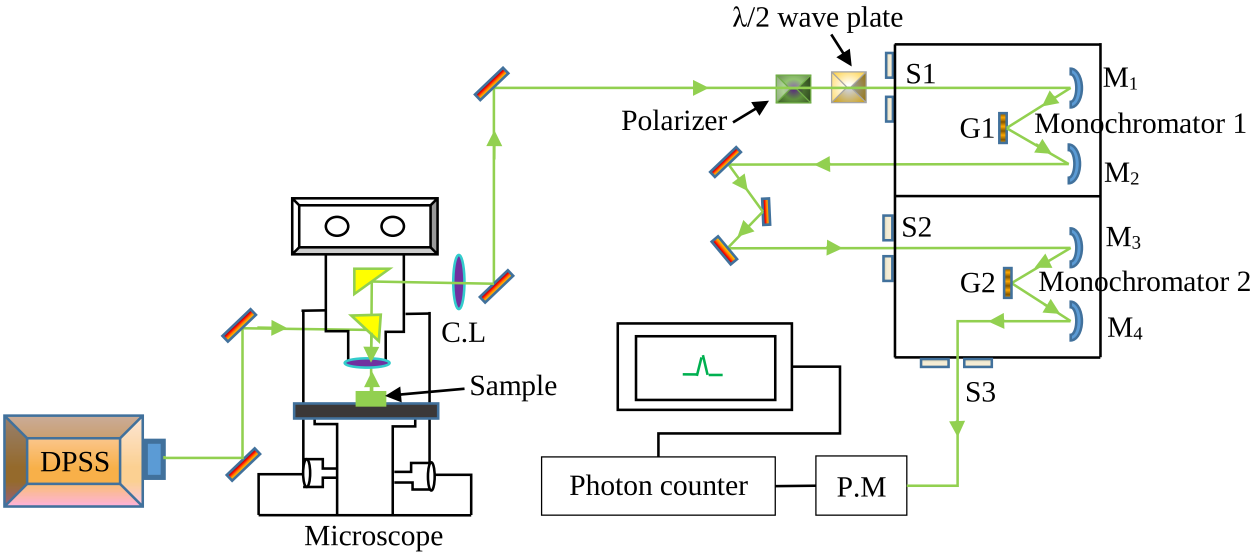

Fig. 2.9. A schematic set up of a double monochromator in Cherny-Tuners arrangement equipped with microscope and P.M tube.

In general, a modern Raman spectroscopy is equipped with multiple monochromators, and can be operated either in a subtractive or in an additive mode. Figure. 2.9 displays the schematic diagram of a double monochromator in an additive mode for a Cherny-Turner arrangement equipped with the microscope and P.M tube. The two gratings, three slits, and four concave mirrors are required in this configuration. By the gratings G1 and G2, the incoming light is two times additively dispersed and scanning occurs by synchronous rotation of both gratings. The suppression of stray light and resolution are greatly improved compared to that of a single monochromator. A third monochromator can be arranged behind the exit slit for further improvement of spectral resolution and the system called as a triple monochromator system. The third monochromator must be turned to be synchronous with the other two gratings. The triple monochromator system is often used for spectroscopic analyses in the immediate vicinity of a very strong line such as a laser line. It is very advantageous to study the low frequency relaxation process and soft mode dynamics in ferroelectric materials. In this case the third monochromator operates with a wide slit and a sharp cut off towards the laser line.

In the case of subtractive mode, the first two monochromators have oppositely directed spatial dispersions. This means that after passing the first two monchromators the light that satisfies the bandpass condition is refocused on the exit slit that serves as the entrance slit of the third monochromator. Only the latter provides the spatial dispersion. In the case of additive mode configuration, the output slit is wide, the linear dispersion and the resolution are higher than that of the subtractive mode configuration. The detector can only record a small part of the spectrum in this configuration. On the other hand, the output slit is narrow, the linear dispersion and the resolution are low in the subtractive mode configuration but the detector can record a much large part of the spectrum.

In this study, a diode pumped solid state (DPSS) laser with a wavelength of 532 nm and a power of about 100 mW was used as an excitation source. The light beam is introduced into the optical microscope with the aid of small mirror to focus the sample. The scattered light is then collected by objective lens using backward geometry, and analyzed using double (Horiba-JY, U-1000) and single (Lucir) monochromator spectrometer of additive dispersion. The temperature of the specimen was controlled by the heating/cooling stage (Linkam, THMS600) with ±0.1 K accuracy over all temperatures.

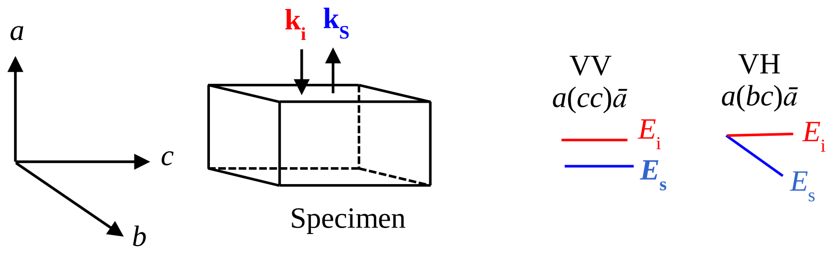

Fig. 2.10. Schematic illustration of VV and VH scattering geometry.

For transparent crystals, the study of the polarization dependence of Raman spectra is very important to clarify the symmetry properties of the Raman modes. Therefore, an analyzer is usually inserted to choose the polarizations of the scattered light. As a convention rule, the scattering geometries are described by the Porto's notation like $\boldsymbol{a(b,c)d}$; where $\boldsymbol{a}$ and $\boldsymbol{b}$ represent the direction of the propagation of incident and scattered light $\mathbf{k}_i$, $\mathbf{k}_s$; $\boldsymbol{c}$ and $\boldsymbol{d}$ are the directions of polarization of incident and scattered light, respectively. In general, all the Raman active modes will appear in a single scattering geometry in the case of ceramic samples. In the present study, Raman spectra were carried out using $a(cc)\bar{a}$ (VV) and

$a(cc)\bar{a}$ (VH) scattering geometry. The schematic diagram of VV and VH scattering configurations at back scattering geometry is shown in Fig. 2.10, where a and $\bar{a}$ denote the directions of the propagation of incident ($\mathbf{k}_i$) and scattered ($\mathbf{k}_s$) light, respectively. In the case of VV scattering the directions of the polarization of incident and scattered light are parallel to each other represented by, for example, *cc*. However, in the case of VH scattering the directions of the polarization of incident and scattered light are perpendicular to each other, for example, along *c* and *b* axes, respectively represented by *bc*.

References

[1]R. Loudon, Adv. Phys. **13**, 423 (1964).

[2]Z. Iqbal and F. J. Owens, *Vibrational Spectroscopy of Phase Transitions*, (Academic press, 1981).

[3]W. Hayes and R. Loudon, *Scattering of Light by Crystals*, (Dover Pulications, Inc. Mineola, New York, 1978).

[4]Blink and B. Zeks, *Soft Modes in Ferroelectrics and Anti-ferroelectrics*, (American Elsevier Publishing Company, 1974).

[5]H. Z. Cummins and P. E. Schoen, *Laser Handbook*, (North-Holland, 1972).

[6]H. Z. Cummins and A. P. Levanyuk, *Light Scattering Near Phase Transitions*, (North Holland, Amsterdam, 1983).

[7]W. Cochran, Adv. Phys. **9,** 387 (1960); **10,** 401 (1961).

[8]M. Born and K. Huang, *Dynamical Theory of Crystal Lattices*, (Oxford University Press, London, 1962).

[9]J. F. Nye, *Physical Properties of Crystals*, (Oxford University Press, London, 1957).

[10]R. Vacher and L. Boyer, Phys. Rev. B **6**, 639 (1972).

[11]I. L. Fabelinskii, *Molecular Scattering of Light*, (Plenum Press, New York, 1968).

[12]D. F. Nelson and M. Lax, Phys. Rev. B **3**, 2778 (1971).

[13]L. D. Landau and E. M. Lifshitz, *Statistical Physics*, (Pergamon press, 1980).

[14]G. Burns, *Introduction to Group Theory with Applications*, (Academic Press, New York, 1977).

[15]H. Kuzmany, *Solid-State Spectroscopy*, (Springer-Verlag, Berlin Heidelberg, 1998).

[16]J. C. Decius and R. M. Hexter, *Molecular Vibrations in Crystals*, (McGrew Hill company, 1977)

[17]D. M. Adams and D. C. Newton, Tables of factor group analysis Beckman-RIIC Ltd., Sunley House, 4 Bedford Park, Croydon CR9 3LG, 1970.

[18]JRS scientific instruments *Tandem Fabry-perot Interferometer: Operating Manual.*

[19]J. R. Sandercock, *Light Scattering in Solids III: Recent Results* (Spinger-Verlag Berlin, New York, 1982).

Chapter 3

Experimental Study of Polar-Nanoregions in $KTa_{1-x}Nb_xO_3$ Single Crystals

3 *Relaxor-like Dynamics and Polar-Nano Regions in Ferroelectric $K(Ta_{1-x}Nb_x)O_3$ Crystals*

3.1 Introduction

The oxide ferroelectrics with the perovskite structure are one of the most active research fields for investigating the role of the polar nanoregions (PNRs) in relation to a relaxor ferroelectric (RFE) phase transition. Among them the relaxor-like ferroelectrics $KTa_{1-x}Nb_xO_3$ (KTN) with homovalent B-site cations are better suited for studying the dynamical anomalies associated to PNRs, because of its structural simplicity in comparison with the lead-based RFEs with heterovalent B-site cations. The KTN is of particular interest in its technological importance for optical applications owing to its high quadratic electro-optic coefficient and excellent photorefractive effect in the vicinity of the Curie temperature (T_C),[1,2] which are attributed to the presence of local polar structure called PNRs. Therefore, the study of the role of local structure is very important to enhance the functionality of ferroelectric materials.[3]

In KTN, Nb ions that replace Ta ions go off-center in the B-site, and therefore they induce PNRs.[4] The microscopic origin of the off-center displacements of Nb ions was rationalized by the pseudo Jahn-Teller effect (PJTE).[5] The off-centering of Nb ions in KTN was described by an eight site model in which the Nb ions move among the equivalent eight [111] directions.[6] In relaxor-like ferroelectrics, the main parameter of understanding the paraelectric cubic to ferroelectric tetragonal phase transition behavior is the dynamic properties related to the temperature evolution of the dynamic and static PNRs. The static PNRs appears below the intermediate temperature, T^*, and the rapid growth of PNRs occurs. Therefore, it is important to study the dynamic properties of KTN to clarify the nature of the ferroelectric phase transition and the dynamics of the PNRs. The different types of measurements, such as acoustic emission,[7] infrared absorption,[8] Raman scattering,[9,10] Brillouin scattering,[11] as well as refractive index and linear-birefringence,[12] were investigated to clarify the dynamics of the PNRs in the cubic phase of KTN crystals. To the best of our knowledge, no result was reported regarding to the local symmetry of PNRs, which is the physical origin of the elastic anomalies and critical slowing down in high quality KTN single crystals. In the present study, the dynamics of the PNRs were studied by Brillouin scattering to clarify the elastic anomaly in the GHz range caused by the coupling of acoustic phonons with the PNRs and their slowing down. The microscopic origin of the central peak (CP) in the cubic phase of the KTN/0.40 crystal was discussed on the basis of the results of the angular dependence of Raman scattering. The local symmetry breaking in the paraelectric cubic phase was also studied by Raman scattering.

3.2 Experimental method of inelastic light scattering

The $KTa_{0.60}Nb_{0.40}O_3$ (KTN/0.40) single crystal grown by the top seeded solution growth method (TSSG)[13] was cut into $4.0\times3.2\times1.0$ mm^3 size pieces along the *a*, *b*, and *c* axes in the cubic coordinate system. The largest (100) surfaces of the crystal were polished to optical grade for Brillouin and Raman scattering. The Brillouin scattering was measured by a Sandercock-type 3+3 passes tandem Fabry-Perot interferometer at a back scattering geometry.[14] The free spectral ranges (FSR) of the spectrometer were fixed at 75 GHz for the longitudinal acoustic (LA), transverse acoustic (TA) mode and at 300 GHz for the central peak (CP) measurements.

The temperature dependence of Raman spectra were measured using a double monochromator (Horiba-JY, U-1000) with the resolution 1 cm^{-1} at a back scattering geometry. A polarization rotation device (Sigma Koki) equipped with a broadband half-waveplate (Kogakugiken) was used to obtain the angular dependence of Raman spectra. The angular dependence of Raman spectra were recorded by a single monochromator (Lucir) combined with a charge coupled device (CCD, Andor) and the *xyz* mapping stage (Tokyo Instruments) installed in the microscope (Olympus). A diode-pumped solid state laser (DPSS) with a wavelength of 532 nm was used to excite the sample for Brillouin and Raman scattering. The temperature of the sample was controlled by a heating/cooling stage (Linkam, THMS600) with the temperature stability of ±0.1 K accuracy over all temperatures.

3.3 Results and discussion on inelastic light scattering

3.3.1 Acoustic anomaly and central peak

The Brillouin scattering spectra of FSR = 75 GHz observed at selected temperatures are shown in Fig. 3.1(a). Each spectrum consists of doublet peaks of the longitudinal acoustic (LA) and transverse acoustic (TA) modes. In the broadband spectra of FSR = 300 GHz, a CP was observed as shown in Fig. 3.1(b). The breaking of Brillouin selection rule is clearly revealed by TA mode which inactive in the cubic symmetry at the back scattering geometry.[15]

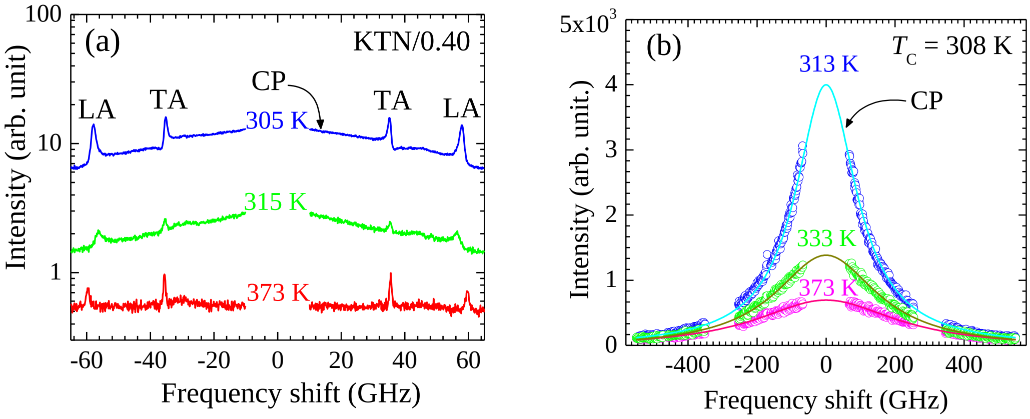

Fig. 3.1. Brillouin scattering spectra at selected temperatures of a KTN/0.40 single crystal measured with the FSR (a) 75 GHz and (b) 300 GHz. The solid lines in (b) indicate the curves fitted by the Voigt function.

The LA and TA sound velocities were determined from the frequency shifts of the LA and TA modes using Eq. (2.8). The temperature dependences of the LA and TA sound velocities are shown in Figs. 3.2(a) and 3.2(b), respectively. The observed LA and TA sound velocities are related to the elastic constants C_{11} and C_{44} in a cubic coordinate, respectively.[15] The LA velocity shows a remarkable softening in the vicinity of the T_C = 308 K, while the TA velocity shows only a slight softening and a small discontinuity at T_C, reflecting the nature of a slightly first order phase transition. The softening of the LA velocity near the Curie temperature and marked increase in the sound attenuation were observed in various lead-based perovskite relaxors such as $0.65Pb(Mg_{1/3}Nb_{2/3})O_3$-$0.35PbTiO_3$ (PMN-35PT), $0.70Pb(Sc_{1/2}Nb_{1/2})O_3$-$0.30PbTiO_3$ (PSN-30PT), $0.85Pb(Zn_{1/3}Nb_{2/3})O_3$-$0.15PbTiO_3$ (PZN-15PT), $0.65Pb(In_{1/2}Nb_{1/2})O_3$-$0.35PbTiO_3$ (PIN-35PT), etc.[16-19] Such softening of the velocity and the increase in the attenuation in the cubic phase are caused by the piezoelectric coupling of the strain polarization fluctuations in the non-centrosymmetric PNRs below the T_B.[20]

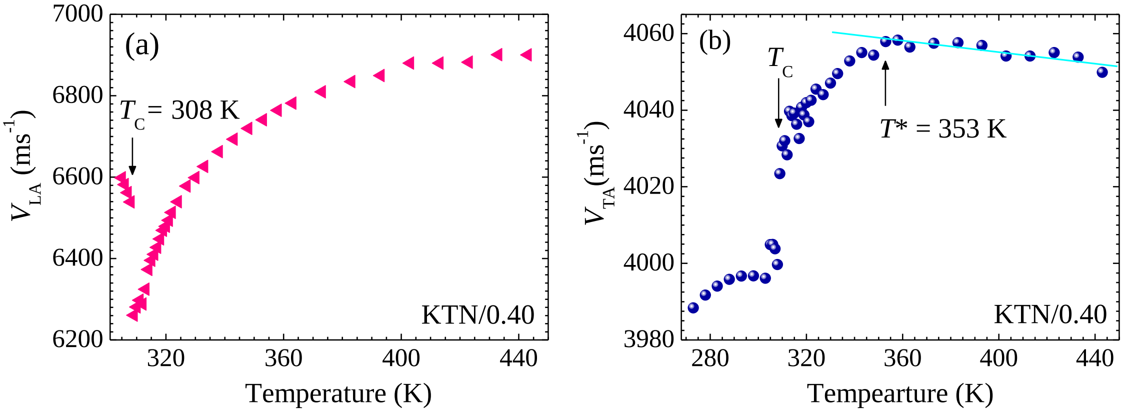

Fig. 3.2. The temperature dependences of (a) longitudinal velocity of the LA mode, and (b) transverse velocity of the TA mode in a KTN/0.40 single crystal.

The remarkable increase in the absorption coefficient of the LA mode towards T_C = 308 K was clearly observed as shown in Fig. 3.3(b). The plot of the sound attenuation shows the clear deviation at about 353 K from the constant temperature dependence at high temperatures as shown in the inset of Fig. 3.3(b). This temperature was assigned as the intermediate temperature (T^*), at which the rapid growth of PNRs begins. The increase in the LA mode absorption below the intermediate temperature indicates the start of rapid growth of the dynamic PNRs at T^*. The sudden growth of PNRs also induces the significant softening of the V_{TA} and the remarkable increase of the CP intensity from T^* to T_C as shown in Figs. 3.2(b) and 3.3(a), respectively. A similar remarkable softening of C_{11} was reported in Ref. 21. When the reported density of 6078.65 kg/cm^3 and the refractive index 2.33 (at the wavelength of 532 nm) of KTN/0.40 are used,[22,23] the observed values at 298 K are the elastic constant $C_{11} = 2.69\text{x}10^{11}$ N/m^2, and $C_{44} = 0.97\text{x}10^{11}$ N/m^2. The LA and TA sound velocities are 6.65 km/s and 3.99 km/s, respectively. The values of the longitudinal sound velocity are in good agreement with the values of KTN/0.32 reported in Ref. 11.

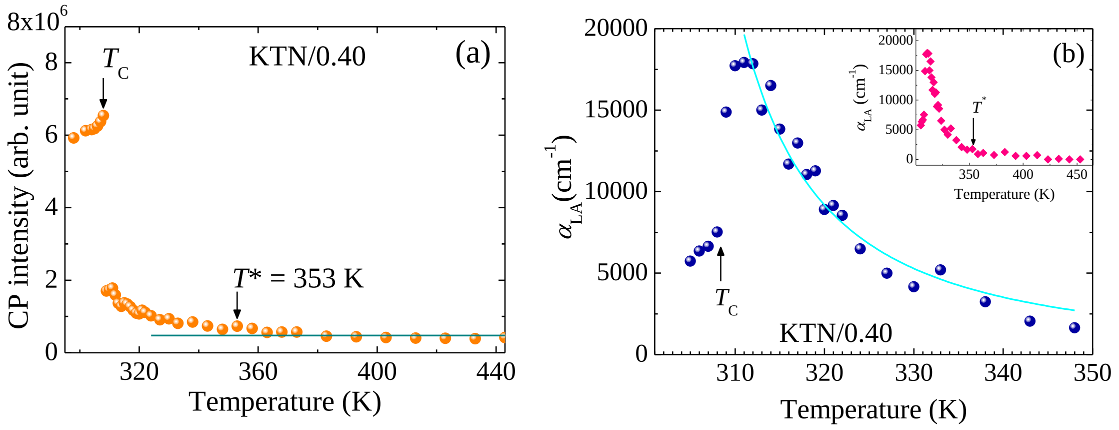

Fig. 3.3. (a) Temperature dependence of the CP intensity of the KTN/0.40 single crystal. (b) Longitudinal sound attenuation in a KTN/0.40 crystal as a function of temperature. The solid lines in (a) and (b) are the guide to eyes and best fit result obtained by Eq. (3.3), respectively. The inset shows the plot of large scale to show T^*.

In relaxor-like ferroelectrics, the anomalous changes in the acoustic properties can be described by the Landau theory assuming the coupling between order parameter and strain in the free energy expression. In general, the Landau expression for the free energy, F of ferroelectrics can be consisted of three parts: the first part is associated with order parameter i.e., polarization P in the present case, the second part is associated with the elastic energy, and finally the coupling term between the order parameter and strain, x. The effective elastic constant C_{ij} due to the change in polarization, driven by the change in strain, can be described by the following expression:[24]

$$C_{\mathrm{ij}} = C_{\mathrm{ij}}^{\infty} - \sum_{k,l} \left(\frac{\partial^2 F}{\partial x_i \partial P_k}\right) \left(\frac{\partial^2 F}{\partial P_k \partial P_l}\right)^{-1} \left(\frac{\partial^2 F}{\partial x_j \partial P_l}\right) \qquad (3.1)$$

where C_{ij}^{∞} is the bare elastic constant independent of P, of which the temperature dependence is determined by the lattice anharmonicity. In the relaxor-like phase of KTN, there is no macroscopic spontaneous polarization i.e. $<P> = 0$ owing to the random orientations of PNRs, we expect the quadratic piezoelectric coupling between the order parameter and strain would dominate the coupling terms in the free energy below T_{B}. The change in elastic constant owing to the quadratic piezoelectric coupling can be expressed as[25]

$$\Delta C = C - C^{\infty} = \gamma <P^2> \chi \qquad (3.2)$$

where $<P^2>$ is the mean value of the squared local polarization of PNRs, γ is the piezoelectric coupling coefficient and χ is the susceptibility for the order parameter. The classical Landau theory for the second-order phase transition predicts only a steplike anomaly for C(T) at the phase transition temperature. In contrast, the local polarizations appear at T_{B} and they gradually grow with decreasing temperature down to T_{C} in relaxor-like ferroelectrics. Albeit the average polarization is zero, their appearance contributes to the decrease of the elastic constants owing to the quadratic nature of the piezoelectric interaction. This decrease would evolve continuously without any abrupt change until the local polarization of PNRs is saturated upon cooling. Therefore, a significant softening and a clear anomaly in both the V_{LA} (related to C_{11}) and V_{TA} (related to C_{44}) corresponding to the T_{C}, which is attributed to the coupling of the LA and the TA modes with fluctuation of local polarization in PNRs. These characteristics have been observed in many relaxors and relaxor-based systems, for example PZN-xPT systems.[26]

The mean-field theory of the sound attenuation anomaly was carried out by Landau and Khalatnikov and shows that this anomaly arises due to coupling between the strains and order parameter.[27] Based on the mean-field approximation, Levanyuk *et al.* found the temperature dependence of the sound attenuation in the following form with the critical exponent of 1.5 in the case of the order-disorder phase transition.[28]

$$\alpha = \alpha_1 \left(T - T_0\right)^{-n} . \qquad (3.3)$$

In order to explain the anomalous behavior and order-disorder nature of the phase transition, we have fitted the sound attenuation between T_{C} and T_{C}+40 K using Eq. (3.3) as shown in Fig. 3.3(b). A good consistency between the experimental data and the fitting result was obtained with the exponent of 1.5, reflecting the order-disorder nature of the phase transition of the high quality KTN/0.40 single crystal. The parameters obtained by fitting the sound attenuation are given in Table 3.1. However, the observed sound attenuation is well fitted by the theoretical line indicating that the anomaly arises due to coupling between the LA phonons and polarization fluctuations in the PNRs.

Table 3.1. Parameters obtained from fitting sound attenuation of a KTN/0.40 single crystal.

α_1($\times 10^6$) (cm^{-1})	T_0 (K)	n
1.03 ± 0.10	296.83 ± 1.05	1.5

The critical slowing down is known as the typical phenomenon of the order-disorder phase transition. Currently, the diversive nature of the relaxation time of the polarization fluctuations in the ferroelectric phase transitions were observed by the broadband Brillouin scattering.[18,20] As shown in Fig. 3.3(a), the CP intensity increases with a decrease in temperature and its intensity becomes a maximum at $T_{C.}$ Upon cooling from high temperature, the increase of the intensity of the CP demonstrates the increase of the correlation among PNRs. The insights about the strong correlations between the local polarizations of PNRs and strain were revealed by various measurement such as neutron scattering, acoustic emission, Raman and Brillouin scattering. Based on the temperature evolution of Raman and diffuse neutron scattering on PMN, PZN and PZN-0.045PT, Toulouse *et al*. reported that the T* exist between T_B and T_C.[29] The existence of the T* was reflected in the anomalous variations in the intensity and frequency of the optical Raman modes and the CP. In typical relaxor, Brillouin scattering study reported that the significant increase in the acoustic damping and the CP intensity begin to take place around T*.[16-19,30] According to Toulouse *et al.*[29] the temperature region between T_B and T* can be marked with the formation of short lived correlations between the off-centered ions, which result in the formation of small dynamic PNRs, while the region between T* and T_C is characterized by the coupling between the adjacent PNRs and their aggregation to form the larger static PNRs. In the present study, the remarkable increase in the damping of the LA mode was observed below the T*, at which rapid growth of PNRs begins, which also induces the significant softening of V_{TA} and remarkable increase in the CP intensity. The relaxation time was determined by the CP width using the following equation:[30]

$$\pi \Gamma_{CP} \tau_{CP} = 1, \tag{3.4}$$

where τ_{CP} and Γ_{CP} are the relaxation time and width of the CP, respectively. The temperature dependence of the inverse relaxation time [Fig. 3.4(a)] shows a linear dependence between T_C and 357 K, which indicates the fact that a cubic-tetragonal ferroelectric phase transition is the order-disorder type. The critical slowing down in the vicinity of T_C is given by

$$\frac{1}{\tau} = \frac{1}{\tau_0} + \frac{1}{\tau_1}\left(\frac{T\text{-}T_C}{T_C}\right) \tag{3.5}$$

In the temperature range of the cubic phase between T_C and T_C+49 K, the observed values are τ_0 = 1.61 ps and τ_1 = 14.8 ps. The value of τ_0 can be attributed to intrinsic lattice defects.[31] It is worthy to compare the value of τ_0 for other relaxor system which exhibited the order-disorder nature of the ferroelectric phase transition in the vicinity of T_C. The value of τ_0 is similar to that reported for PZN-0.15PT.[32] From these result one can conclude that an order-disorder mechanism contributes to the slowing down of the dynamics PNRs in a KTN/0.40 single crystal. Upon cooling, the CP intensity drastically increases towards

T_C below T*, indicating the rapid growth of the volume fraction of PNRs,[6,11] which also induces the softening of the LA phonon velocity and the rapid increase in the attenuation from T^* to T_C.

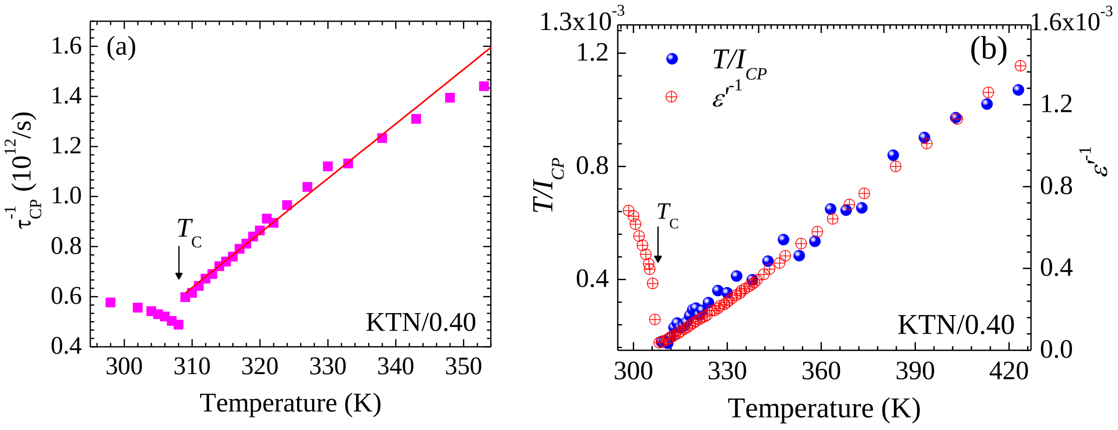

Fig. 3.4. The temperature dependence of (a) the inverse of the relaxation time determined from the CP width, where the solid line shown in (a) is result fitted using Eq. (3.5). (b) Temperature dependence of T/I_{CP} (closed circles) and the inverse dielectric constant (open circles) at the frequency of 1 kHz.

We also studied the temperature dependence of the inverse of the susceptibility determined by the CP intensity and compared this result with the inverse dielectric constant as shown in Fig. 3.4(b). The CP intensity I_{CP} is related to the static susceptibility, $\chi(0)$, by the equation, $I = k_B T \chi(0)$, where k_B denotes the Boltzmann constant. The ratio of the slope just below and above T_C is about -3.2 which is less than -2 (that for the second order transition). Therefore, this phase transition is slightly first order which is in agreement with Courdille *et al.* and Triebwasser's for x = 40% and x = 46% crystals, respectively.[33,34]

To discuss the temperature evolution of the dynamic nature of the PNRs, the average size of the dynamic PNRs, l_{PNR}, was estimated by multiplying the relaxation time by the sound velocity of the LA mode because the maximum of the characteristics length of the strain fluctuations is given by the propagation length within the relaxation time.[35] Upon cooling, the average size of the dynamic PNRs increases towards T_C as shown in Fig. 3.5, reflecting the growth of the PNRs up to the percolation limit in which the reorientation is completely suppressed.[36] At an intermediate temperature T^*, the size is about 4.5 nm, which is in agreement with the size of a dynamic polar cluster of 4-6 nm.[11]

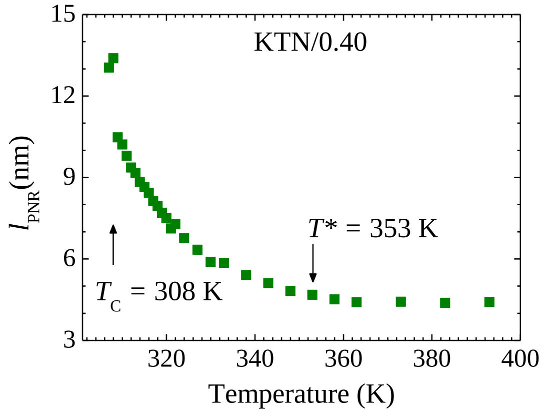

Fig. 3.5. The mean size of the dynamic PNRs as a function of temperature.

3.3.2 Temperature dependence of Raman scattering spectra

The precursor dynamics in the KTN/0.40 single crystal were also investigated by Raman scattering. The temperature dependence of reduced VV and VH Raman spectra of the KTN/0.40 single crystal is shown in Fig. 3.6. At 300 K, the presence of the strong first order TO_2 mode at around 196 cm^{-1} in both VV and VH spectra and TO_3 mode at around 279 cm^{-1} in the VH spectrum suggests that the KTN/0.40 crystal does not belong to the cubic $Pm\bar{3}m$ symmetry at room temperature (RT), which is in good agreement with the phase diagram.[37,38] The detailed mode assignment of the KTN crystals were reported in Refs. 39 and 40.

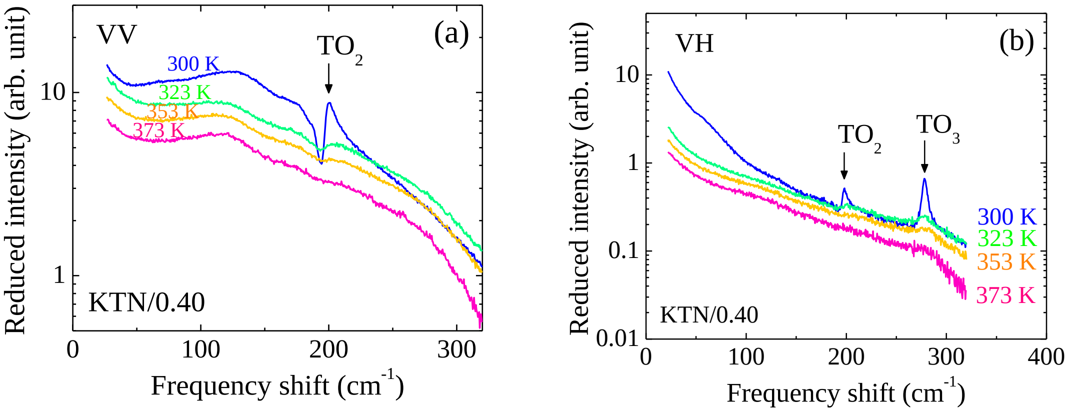

Fig 3.6. Reduced (a) $a(cc)\bar{a}$ (VV) and (b) $a(bc)\bar{a}$ (VH) Raman spectra of the KTN/0.40 single crystal at some selected temperatures.

The reduced intensity of the Stokes component, $I^{r}(\omega)$, was calculated by

$$I^{r}(\omega)=\frac{I(\omega)}{\omega[n(\omega)+1]} \quad , \tag{3.6}$$

where $n(\omega)=\frac{1}{\exp\left(\frac{\hbar\omega}{k_B T}\right)-1}$.

$I(\omega)$ and $n(\omega)$ are the observed Raman intensity and the Bose-Einstein population factor, respectively. In order to investigate the temperature dependence of a CP, which is related to the relaxation process of dynamic PNRs, all spectra in the frequency range between 20 cm^{-1} ~ 320 cm^{-1} were fitted by a Lorentzian central peak, the damped harmonic oscillator (DHO) model, and the third order polynomial with a Fano function given by[41,42]

$$I^{r}(\omega)=\frac{2A_{CP}}{\pi}\frac{\Gamma_{CP}}{4\omega^2+\Gamma_{CP}^2}+\sum_i\frac{A_i\Gamma_i\omega_i^2}{\left(\omega^2-\omega_i^2\right)^2+\omega^2\Gamma_i^2}+I_B(\omega)+\frac{I_0(q+\varepsilon)^2}{(1+\varepsilon^2)} \quad , \tag{3.7}$$

where $I_B(\omega)=P\left(\omega-\omega_{TO2}\right)^3+Q\left(\omega-\omega_{TO2}\right)^2+R\left(\omega-\omega_{TO2}\right)+S$.

Here A_{CP} and Γ_{CP} are intensity and width of the CP, respectively. A_i, Γ_i, and ω_i are the intensity factor, the damping constant and the mode frequency of the ith Raman active mode, respectively. I_0 is intensity of the Fano like asymmetric peak (TO_2 mode), q is the asymmetry parameter, $\varepsilon=2\left(\omega-\omega_{TO2}\right)/\Gamma_{TO2}$ is the reduced energy and Γ_{TO2} is its width. P, Q, R, and S are constants.

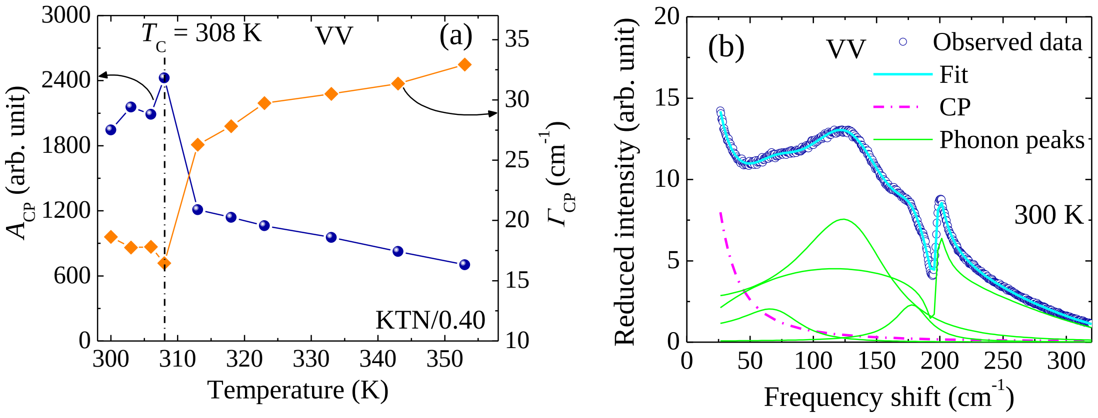

Fig 3.7. (a) Temperature dependence of reduced intensity and width of the CP of the KTN/0.40 single crystal approximated by Lorentzian function using the Eq. (3.7). The example of approximation is shown in (b).

The temperature evolution of the reduced intensity, A_{CP}, and the width, Γ_{CP}, of the CP observed at VV scattering is displayed in Fig. 3.7(a). The existence of the CP is a direct consequence of the relaxation process of the local polarization fluctuations. Due to the fast relaxation process, the CP is weak and broad.[43] Its slowing down causes the growth and narrowing of the CP. In the vicinity of the T_C, the temperature dependence of the CP in the KTN/0.40 crystal [Fig. 3.7(a)] is very similar with those of PZN,[41] and $Pb(Mg_{1/3}Nb_{2/3})O_3$ (PMN)[44] crystals, and this fact suggests the applicability of the model[41,44] explaining the CP by the relaxational motion of PNRs and its progressive motion restriction upon cooling. It is worth noting that both A_{CP} and Γ_{CP} show the clear anomaly in the vicinity of the T_C = 308 K as shown in Fig. 3.7(a). As can be seen in Fig. 3.7(a), the CP intensity increases towards the T_C upon cooling, demonstrating the increase of the correlation among PNRs. In addition, the Γ_{CP}, which is inversely proportional to the relaxation time, becomes narrower significantly towards the T_C, indicating the slowing down of the precursor dynamics.

3.3.3 Angular dependence of Raman scattering spectra

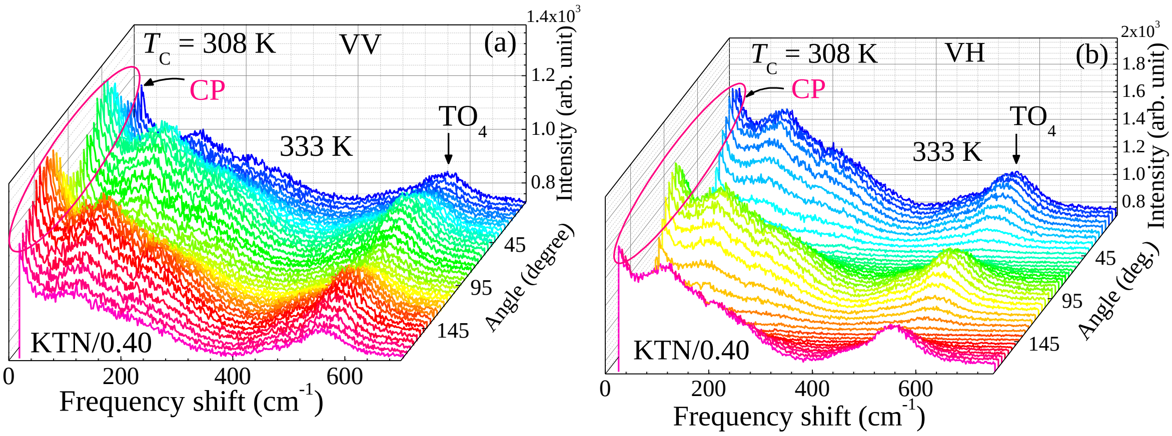

Fig. 3.8 Angular dependence of (a) $a(cc)\bar{a}$ (VV) and (b) $a(bc)\bar{a}$ (VH) Raman spectra of the KTN/0.40 crystal measured in a cubic phase.

For the better understanding of the microscopic origin of the CP in the KTN/0.40 crystal, we studied the angular dependence of both VV and VH spectra in the paraelectric cubic phase as shown in Fig. 3.8. The Raman spectra clearly changed periodically with the rotation of the plane of the polarization. In particular, the intensity of the CP changed markedly with the rotation of the plane of the polarization, and the variation of the intensity is mutually opposite between the VV and VH spectra (Fig. 3.8). To clarify the origin of the CP caused by PNRs, we performed the Raman tensor calculation considering the local symmetry of PNRs. In PMN, the local symmetry of the PNR was reported as rhombohedral *R3m* on the basis of the neutron pair distribution function (PDF) analysis.[45] There are three Raman active modes, $A_1(z)$, $E(-x)$ and $E(y)$ of the *R3m* symmetry with the following Raman tensors:[46]

$$A_1(z) = \begin{pmatrix} a & 0 & 0 \\ 0 & a & 0 \\ 0 & 0 & b \end{pmatrix},\ E(-x) = \begin{pmatrix} 0 & -c & -d \\ -c & 0 & 0 \\ -d & 0 & 0 \end{pmatrix},\ E(y) = \begin{pmatrix} c & 0 & 0 \\ 0 & -c & d \\ 0 & d & 0 \end{pmatrix} \qquad (3.8)$$

The angular dependence was calculated using the Raman tensor by

$$\overline{R}^{-1}\cdot\overline{C}^{-1}\cdot\left(A_1(z)\mathrm{or}E(y)\mathrm{or}E(-x)\right)\cdot\overline{R}\cdot\overline{C} \quad , \qquad (3.9)$$

where $\overline{R}=\begin{pmatrix} 1 & 0 & 0 \\ 0 & \cos\theta & -\sin\theta \\ 0 & \sin\theta & \cos\theta \end{pmatrix}$

and $\overline{C}$ is the transformation matrix corresponding to the Raman tensor modification and θ is the rotation angle of the experimental coordinates.[46] It is well established that local rombohedral regions are oriented randomly along the eight equivalent polarization directions. For this reason, the angular dependence was calculated in the multidomain states in which the contributions of all eight domains are summed up equally. It is important to note that the variation of the CP intensity (Fig. 3.9) of the KTN/0.40 crystal in the cubic phase is similar to the behavior of PNRs with $A_1(z)$ symmetry.[46] One can obtain the values of the intensity of the *cc* (VV) and *bc* (VH) components for $A_1(z)$ and $E(x,y)$ symmetries of PNRs after the transformation of Raman tensor components using Eq. (3.9) as follows:

$$I^{cc}_{A_1(z)} \propto \frac{8}{9}[4|a|^2+4|a||b|\cos\varphi+|b|^2+(|a|^2-2|a||b|\cos\varphi+|b|^2)\sin^2 2\theta] \quad , \qquad (3.10)$$

$$I^{bc}_{A_1(z)} \propto \frac{8}{9}(|a|^2-2|a||b|\cos\varphi+|b|^2)\cos^2 2\theta \quad , \qquad (3.11)$$

$$I^{cc}_{E(x,y)} \propto \frac{8}{3}\sin^2\theta\,[2|d|^2+|c|^2+3|c|^2\cos^2\theta]+\frac{8}{9}\left[(5|c|^2+16|d|^2)\cos^4\theta-2(|c|^2+5|d|^2)\cos^2\theta+|c|^2+2|d|^2\right], \qquad (3.12)$$

$$I^{bc}_{E(x,y)} \propto \frac{2}{3}[3|c|^2\cos^2 2\theta+|c|^2+2|d|^2]+\frac{2}{9}[(5|c|^2+16|d|^2)\sin^2 2\theta+4|c|^2+2|d|^2] \ , \qquad (3.13)$$

where $\varphi = \arg(b)-\arg(a)$ stands for the phase difference of the two independent components of the Raman tensor of the A_1(z) symmetry of PNRs.

The angular dependence of the observed intensity, I_{CP}, of the CP obtained from VV and VH spectra is shown in Figs. 3.9(a) and 3.9(b), respectively. As shown in Fig. 3.9, the variation of the intensity of the CP with the rotation angle exhibits the sinusoidal tendency, reflecting the anisotropy of Raman scattering of the KTN/0.40 crystal. The theoretical fits were performed via Eqs. (3.10) and (3.11), which demonstrate the phase difference between the different Raman tensor components contributing to the susceptibility of the polarized angle.

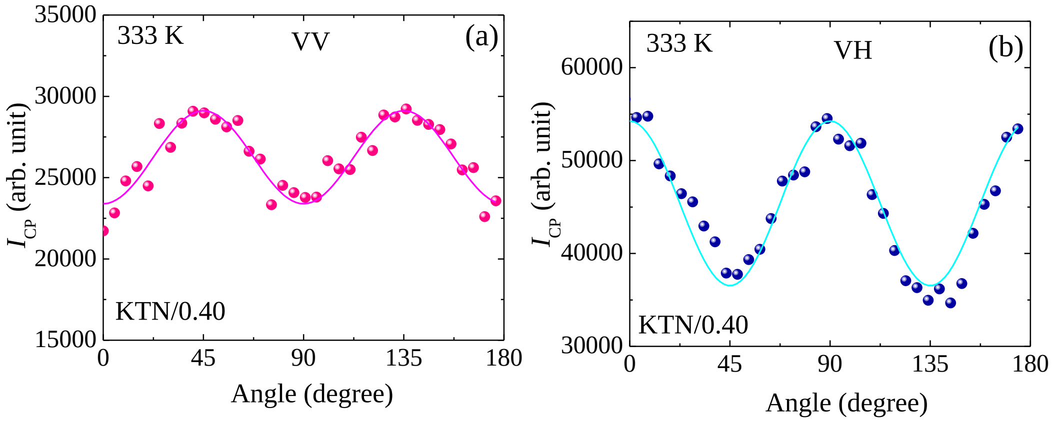

Fig. 3.9. The intensity of the CP observed in (a) VV and (b) VH spectra as a function of the rotation angle. The solid lines in (a) and (b) are best results fitted by Eqs. (3.10) and (3.11), respectively.

The observed intensity variation of the CP measured at both VV and VH scattering was well fitted by Eqs. (3.10) and (3.11), respectively, implying that the CP in the paraelectric cubic phase of the KTN/0.40 crystal stem from $A_1(z)$ symmetry of PNRs with a rhombohedral polar *R3m* symmetry. The best-fitted results for obtaining phase difference between different components of the Raman tensor for the $A_1(z)$ symmetry are listed in Table 3.2.

Table 3.2. The best fit results of the anisotropy ratio and the phase difference between different Raman tensor components of PNRs with A_1(z) symmetry.

	A_1(z) symmetry	
	VV	VH
Anisotropy ratio, $\lvert b/a \rvert$	0.15	0.18
Phase difference	0.52 π	0.52 π^a

^{a}Fixed parameter

It is seen that the anisotropy ratio and the phase difference of the A_1(z) symmetry of PNRs are similar even for different polarization geometries. These results suggest that the phase difference exist between different Raman tensor components, and the phase difference and related anisotropic properties appear in both VV and VH scattering. The similar phase difference and anisotropic property in both VV and VH scattering were also reported in the A_1 mode of the GaN by Lin *et al.*.[47] The value of the phase difference between various vibrating components of the $A_1(z)$ symmetry of PNRs is in good agreement with the values reported for $PbTiO_3$ single crystal and $SmBa_2Cu_3O_7$ thin films.[48,49] The significant effect of the phase difference on the intensity of the A_{1g}-like phonons was reported in Ref. 49.

3.3.4 Local symmetry breaking observed by Raman scattering

Raman scattering of the KTN/0.40 was measured as a function of temperature to study the local symmetry breaking in the cubic phase. Recently, Raman scattering of the typical relaxor,

$Pb(Zn_{1/3}Nb_{2/3})O_3$–$PbTiO_3$ (PZN-PT), with a perovskite structure was studied in the cubic phase to clarify the local symmetry breaking due to the existence of PNRs with a rhombohedral $R3m$ symmetry.[50,51] According to the Raman selection rule, the first order Raman mode is not allowed in the cubic phase with the $Pm\bar{3}m$ symmetry. However, the first order TO_2 and TO_3 modes are still prominent in a cubic phase (Fig. 3.6). Figure 3.10(a) shows the temperature dependence of reduced intensity, A_{TO3}, and width, Γ_{TO3}, of the TO_3 mode of the KTN/0.40 single crystal.

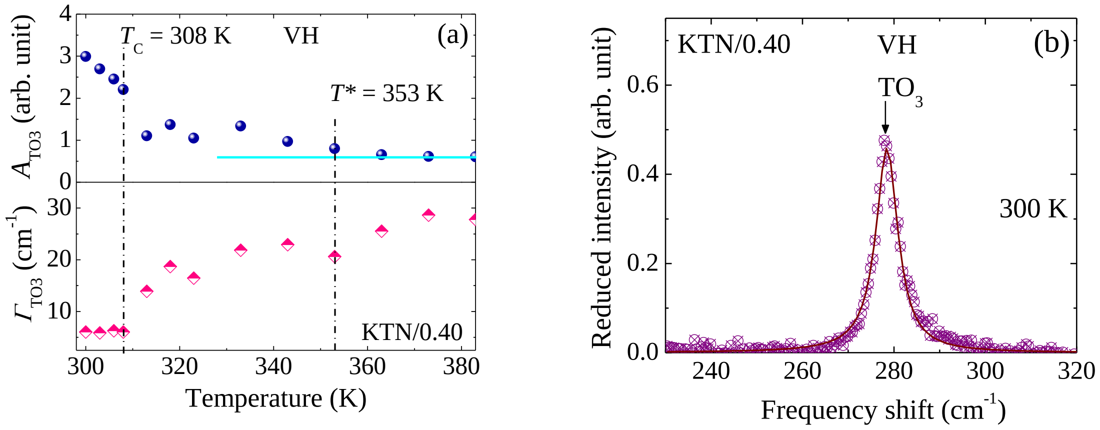

Fig. 3.10. (a) Temperature dependence of reduced intensity and width of the TO_3 of the KTN/0.40 single crystal. The solid line in (a) is guide to eyes. (b) Example of fit of the TO_3 mode by DHO model, where the solid line is the best-fitted line by the DHO function.

It is significant that the intensity of the TO_3 mode decreases rapidly as the T_C is approached. Above the T_C, the TO_3 mode continues to decrease slowly in intensity showing anomaly around the $T^* \sim 353$ K, where the dynamic to static transition of PNRs begins. The value of the characteristic temperatures is consistent with the Brillouin scattering results. It is also important to note that the Γ_{TO3} exhibits noticeable changes associated with these precursor effects as shown in the lower part of the Fig. 3.10(a). Therefore, the existence of the weak intensity of the TO_3 in a cubic phase indicates the local symmetry breaking caused by the existence of PNRs with rhombohedral symmetry.

In order to clarify local symmetry of PNRs, which was responsible for the breaking of local symmetry in the cubic phase of KTN crystals, we also analyze the angular dependence of Raman spectra. Since the intensity of the TO_3 mode was too weak in angular dependence of Raman spectra (Fig. 3.8), therefore we were mainly concerned about the TO_4 mode. The example of fit in the frequency range between 400 and 730 cm^{-1} fitted by the damped harmonic oscillator (DHO) function is shown in Fig. 3.11(a). The dotted (~ 470 cm^{-1}) and dashed (~ 575 cm^{-1}) bands denote the modes of second order scattering, whereas the solid band (~ 540 cm^{-1}) indicates the first order scattering of the TO_4 mode.[39] The angular dependence of the TO_4 mode intensity is plotted by the solid circles in Fig. 3.11(c). The observed intensity of the TO_4 mode was well fitted using the Eq. (3.11) for $A_1(z)$ symmetry of PNRs. The fitted curve reproduces the observed intensity variation revealing that the TO_4 mode in the paraelectric phase stems from the $A_1(z)$ symmetry of the PNRs with a rhombohedral $R3m$ symmetry.[52] Therefore, in the cubic symmetry, the KTN is considered to be composed of at least locally distorted PNRs with $R3m$ in the cubic matrix with $Pm\bar{3}m$ symmetry below the Burn temperature.

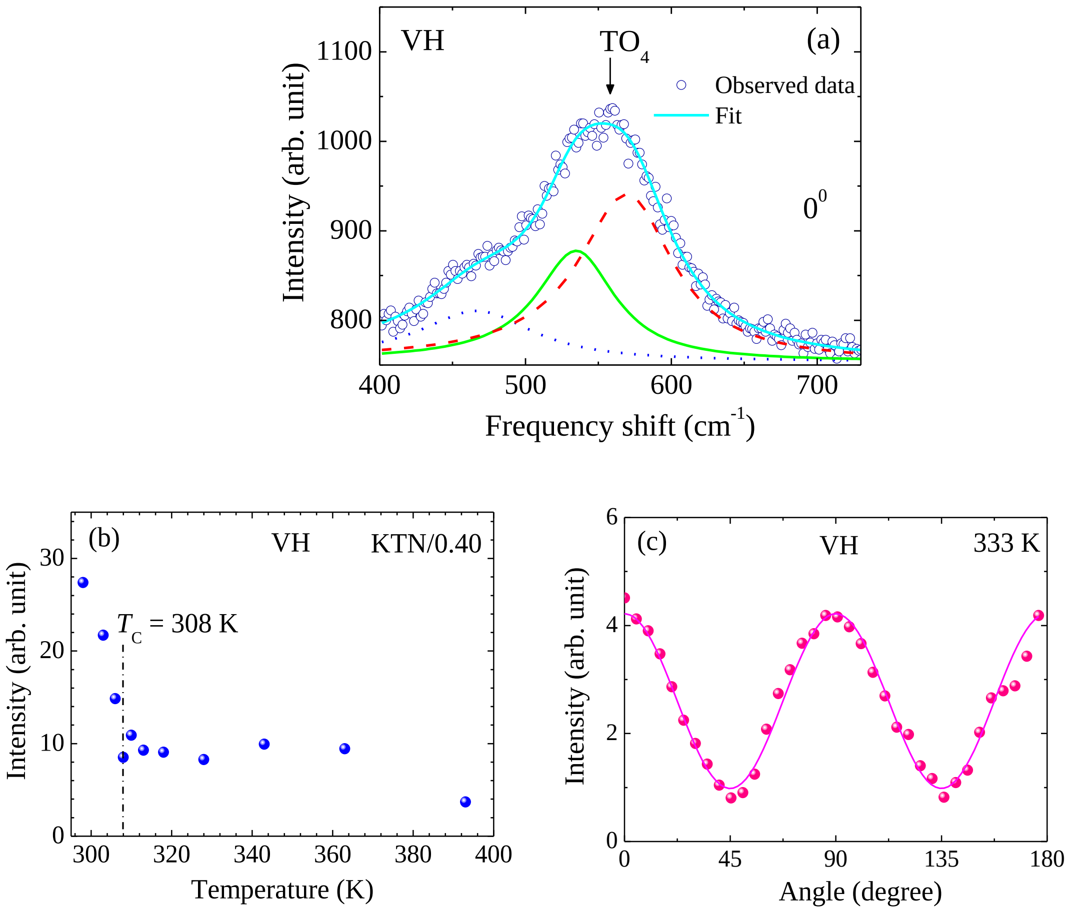

Fig. 3.11. (a) The example of fit of Raman spectra in the frequency range between 400 and 730 cm^{-1} by the DHO model. (b) The temperature dependence of the TO$_4$ mode intensity of the KTN/0.40 single crystal. (c) The angular dependence of the TO$_4$ mode intensity, where the observed intensity is denoted by the solid symbols. The solid line denotes the calculated intensity of the $A_1(z)$ symmetry of the PNRs.

3.4 Summary

The relaxor-like dynamics related to PNRs have been investigated in the ferroelectric phase transition of $K(Ta_{1-x}Nb_x)O_3$ crystals with $x = 0.40$ using Brillouin and Raman scatterings. According to the analysis of the angular dependence of Raman scattering, the microscopic origin of the CP in the cubic phase of KTN crystals was attribute to PNRs with $A_1(z)$ symmetry with a polar rhombohedral symmetry. The phase difference Raman tensor components of $A_1(z)$ symmetry of PNRs was determined. The breaking of local symmetry due to the existence of PNRs was observed by the appearance of the first order Raman scattering in the cubic phase, which is inactive in accordance to the Raman selection rule. The significant softening of the velocity and the increase in attenuation of the LA mode were observed in the vicinity of the Curie temperature, T_C = 308 K. The increase in the LA mode attenuation was clearly observed below the intermediate temperature, T^* = 353 K, indicating the start of the rapid growth of the dynamic PNRs, which also induced the remarkable softening of the TA mode and increase in the intensity of the CP. The evolution of the dynamic PNRs was discussed based on the size growth with temperature, and below T^*, it rapidly increases towards T_C up to the percolation limit. The order-disorder nature of the ferroelectric phase transition is clearly observed by the critical slowing down towards T_C by the temperature variation of the broad central peaks. By Raman scattering, the soft mode behavior of KTN/0.40 was not observed. Therefore, it is concluded that the nature of the phase transition of KTN/0.40 is purely order-disorder.

References

[1]Y. C. Chang, C. Wang, S. Yin, R. C. Hoffman, and A. G. Mott, Opt. Lett. **38,** 4574 (2013).

[2]J. E. Geusic, S. K. Kurtz, L. G. Van Uitert, and S. H. Wemple, Appl. Phys. Lett. **4,** 141 (1964).

[3]D. A. Keen, IUCrJ **3,** 8 (2016).

[4]O. Hanske-Petitpierre, Y. Yakoby, J. Mustre De Leon, E. A. Stern, and J. J. Rehr, Phys. Rev. B **44,** 6700 (1991).

[5]V. Polinger, Chem. Phys. **459,** 72 (2015).

[6]J. P. Sokoloff, L. L. Chase, and L. A. Boatner, Phys. Rev. B **41,** 2398 (1990).

[7]E. Dul'kin, S. Kojima, and M. Roth, Euro. Phys. Lett. **97,** 57004 (2012).

[8]A. Pashkin, V. Železný, and J. Petzelt, J. Phys.: Condens. Matter **17,** L265 (2005).

[9]O. Svitelskiy and J. Toulouse, J. Phys. Chem. Solids **64,** 665 (2003).

[10]J. Toulouse, P. DiAntonio, B. E. Vugmeister, X. M. Wang, and L. A. Knauss, Phys. Rev. Lett. **68,** 232 (1992).

[11]R. Ohta, J. Zushi, T. Ariizumi, and S. Kojima, Appl. Phys. Lett. **98,** 092909 (2011).

[12]W. Kleemann, F. J. Schäfer, and D. Rytz, Phys. Rev. Lett. **54,** 2038 (1985).

[13]W. A. Bonner, E. F. Dearborn, and L. G. Van Uitert, Ceram. Bull. **44,** 9 (1965).

[14]S. Kojima, Jpn. J. Appl. Phys. **49,** 07HA01 (2010).

[15]R. Vacher and L. Boyer, Phys. Rev. B **6,** 639 (1972).

[16]F. M. Jiang and S. Kojima, Phys. Rev. B **62,** 8572 (2000).

[17]S. Kojima and J.-H. Ko, Curr. Appl. Phys. **11,** S22 (2011).

[18]V. Sivasubramanian, S. Tsukada, and S. Kojima, J. Appl. Phys. **105,** 014108 (2009).

[19]S. Kojima, S. Tsukada, Y. Hidaka, A. A. Bokov, and Z.-G.Ye, J. Appl. Phys. **109,** 084114 (2011).

[20]S. Tsukada and S. Kojima, Phys. Rev. B **78,** 144106 (2008).

[21]L. A. Knauss, X. M. Wang, and J. Toulouse, Phys. Rev. B **52,** 13261 (1995).

[22]A. Reisman and E. Banks, J. Am. Chem. Soc. **80**, 1877 (1958).

[23]F. S. Chen, J. E. Geusic, S. K. Kurtz, J. G. Skinner, and S. H. Wemple, J. Appl. Phys. **37**, 388 (1966).

[24]J. C Slonczewski and H. Thomas, Phys. Rev. B **1,** 3599 (1970).

[25]G. A. Smolenskii, N. K. Yushin, and S. I. Smirnov, Sov. Phys. Solid State **27,** 492 (1985).

[26]J-H. Ko, D. H. Kim, and S. Kojima, Phys. Rev. B **77,** 104110 (2008).

[27]L. D. Landau and E. M. Lifshitz, *Physical Kinetics* (Nauka, Moscow, 1979) English translation: Pergarnon Press, Oxford.

[28]A. P. Levanyuk, S. A. Minyukov, and M. Vallade, J. Phys. I France **2,** 1949 (1992).

[29]J. Toulouse, F. Jiang, O. Svitelskiy, W. Chen, and Z.-G. Ye, Phys. Rev. B **72** (2005) 184106.

[30]S. Kojima and J.-H. Ko, Curr. Appl. Phys. **11** (2011) S22.

[31]A.Hushur, S. Gvasaliya, B. Roessli, S.Lushnikov, and S. Kojima, Phys. Rev. B **76,** 064104 (2007).

[32]K. K. Mishra, V. Sivasubramanian, A. K. Arora, and D. Pradhan, J. Appl. Phys. **112**, 114109 (2011).

[33]J. M. Courdile, J. Dumas, S. Ziolkiewicz, and J. Joffrin, J. Phys. (Paris) **38,** 1519 (1977).

[34]S. Triebwasser, Phys. Rev. **114,** 63 (1959).

[35]S. Kojima and S. Tsukada, Ferroelectrics **405,** 32 (2010).

[36]R.Pirc and R. Blinc, Phys. Rev. B **76,** 020101 (2007).

[37]S. Triebwasser, Phys. Rev. **114,** 63 (1959).

[38]D. Rytz and H. J. Scheel, J. Cryst. Growth **59,** 468 (982).

[39]S. K. Manlief and H. Y. Fan, Phys. Rev. B **5,** 4046 (1972).

[40]G. E. Kugel, M. D. Fontana, and W. Kress, Phys. Rev. B **35,** 813 (1987).

[41] J. Toulouse, F. Jiang, O. Svitelskiy, W. Chen, and Z.-G. Ye, Phys. Rev. B **72,** 184106 (2005).

[42] Y. Yacoby, Z. Physik B **31,** 275 (1978).

[43] K. H. Michel, J. Naudts, and B. D. Raedt, Phys. Rev. B **18,** 648 (1978).

[44] O. Svitelskiy, J. Toulouse, G. Yong, and Z.-G. Ye, Phys. Rev. B **68,** 104107 (2003).

[45] I.-K. Jeong, T. W. Darling, J. K. Lee, Th. Proffen, R. H. Heffner, J. S. Park, K. S. Hong, W. Dmowski, and T. Egami, Phys. Rev. Lett. **94,** 147602 (2005).

[46] H. Taniguchi, M. Itoh, and D. Fu, J. Raman spectrosc. **42,** 706 (2011).

[47] H. C. Lin, Z. C. Feng, M. S. Chen, Z. X. Shen, I. T. Ferguson, W. and Lu, J. Appl. Phys **105,** 036102 (2009).

[48] Y. Fujii, M. Noju, T. Shimizu, H. Taniguchi, M. Itoh, and I. Nishio, Ferroelectrics **462,** 8 (2014).

[49] T. Strach, J. Brunen, B. Lederle, J. Zegenhagen, and M. Cardona, Phys. Rev. B **57,** 1292 (1998).

[50] M. S. Islam, S. Tsukada, W. Chen, Z.-G. Ye, and S. Kojima, J. Appl. Phys. **112,** 114106 (2012).

[51] H. J. Trodahl, N. Klein, D. Damjanovic, N. Setter, B. Ludbrook, D. Rytz, and M. Kuball, Appl. Phys. Lett. **93,** 262901 (2008).

[52] M. M. Rahaman, T. Imai, J. Miyazu, J. Kobayashi, S. Tsukada, M. A. Helal, and S. Kojima, J. Appl. Phys. **116,** 074110 (2014).

Chapter 4

Effects of Li-Doping in $KTa_{1-x}Nb_xO_3$ Single Crystals

4.1 *The Li-Doping Effect on Polar-Nanoregions in $K(Ta_{1-x}Nb_x)O_3$ Single Crystals*

4.1.1 Introduction

The Li-doping effect on the $KTaO_3$ is one of the current topics in materials science. The quantum paraelectricity was suppressed and a ferroelectricity appeared by the Li-doping.[1,2] In $K_{1-y}Li_yTaO_3$ (KLT), there is the critical Li concentration $y_C = 0.022$ above which the KLT undergoes a ferroelectric transition at T_C, and below the concentration y_C it freezes into a dipole glass state at the glass transition temperature, T_g.[2] Cai *et al*. reported that such a drastic change in transition behavior of KLT across the y_C attributed to the piezoelectric character of PNRs, which ultimately drives the structural transition, with a critical level of local polarization.[2] Therefore, the Li-doped KTN can be an interesting system for investigating the effects of Li ions on the precursor dynamics of the relaxor ferroelectric phase transition and thus also related physical properties. The shear components of piezoelectric response of the high quality Li-doped KTN single crystals were studied with the aim of applying these materials as transducers, actuators, and sensors.[3,4] Of late, the remarkable increase in capacitance and permittivity of the Li-doped KTN single crystal was observed by injecting electrons with the application of a voltage using titanium electrodes.[5] However, the extensive studies on the effect of Li ions on the phase transition behaviors of the Li-doped KTN are rather scarce, which will be indispensable for accelerating the application of these materials. In the present study, therefore, the Li-doped high quality KTN single crystals were studied to investigate the effect of Li-doping on PNRs and the lattice dynamical properties related to a relaxor ferroelectric phase transition in comparison with the non-doped KTN crystals.[6]

4.1.2 Experimental

The $K_{0.95}Li_{0.05}Ta_{0.73}Nb_{0.27}O_3$ (KLTN/0.05/0.27) single crystals used in the present study were grown by the top seeded solution growth (TSSG)[7] technique at NTT Corporation. The specimen was cut having the size of 4.0×3.2×1.2 mm^3 with the largest faces oriented perpendicular to the [100] direction. Micro-Brillouin spectra were measured at the backscattering geometry using a high-contrast 3+3 passes tandem Fabry-Perot interferometer.[8] The specimen was excited using a diode-pumped solid state (DPSS) laser with a wavelength of 532 nm and a power about 100 mW. The spectra were recorded using the free spectral range (FSR) of 75 GHz for the longitudinal acoustic (LA) and the transverse acoustic (TA) modes and 300 GHz for the central peak (CP) measurements. The specimen temperature was controlled using a cooling/heating stage (Linkam THMS600). The temperature stability of the specimen was within ±0.1 K over all temperatures. The dielectric properties were measured using an impedance/gain-phase analyzer (SI 1260, Solarto) combined with a home-made furnace and temperature controller (CHINO, KP 1000).

4.1.3 Results and discussion

4.1.3.1 Sound velocity and attenuation of Li-doped KTN

The Brillouin scattering spectra of a KLTN/0.05/0.27 single crystal at some selected temperatures in a narrow frequency range is shown in Fig. 4.1.1. As can be seen from the Fig. 4.1.1, the LA and TA modes appeared in each spectrum in the wide temperature range. In addition, a CP developed on cooling and its intensity showed the maximum around T_C. The qualitatively similar spectra were already reported in a high quality KTN/0.40 single crystal with no Li content.[6] Recently, Rahaman *et al.* reported the breaking of the Raman selection rule in the high quality KTN/0.40 single crystal by the observation of A_1(z) symmetry of PNRs with the rhombohedral polar symmetry using Raman scattering.[6]

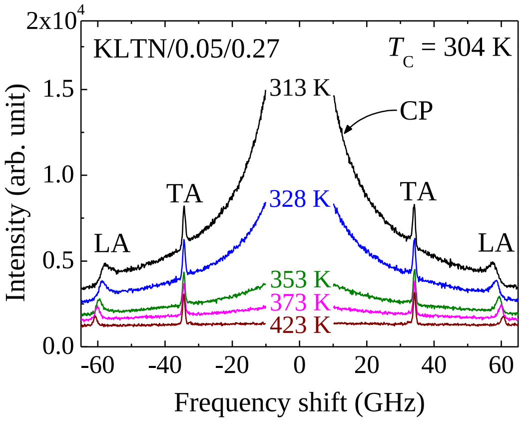

Fig. 4.1.1. Brillouin scattering spectra of a KLTN/0.05/0.27 single crystal measured in the FSR = 75 GHz at some selected temperatures.

The temperature dependences of the LA velocity, V_{LA}, and the TA velocity, V_{TA}, as well as the TA attenuation, α_{TA}, of the KLTN/0.05/0.27 single crystal were determined and plotted in Figs. 4.1.2(a) and 4.1.2(b), respectively. The observed sound velocities of the LA and TA modes are related to the elastic constants C_{11} and C_{44} in a cubic symmetry, respectively.[9]

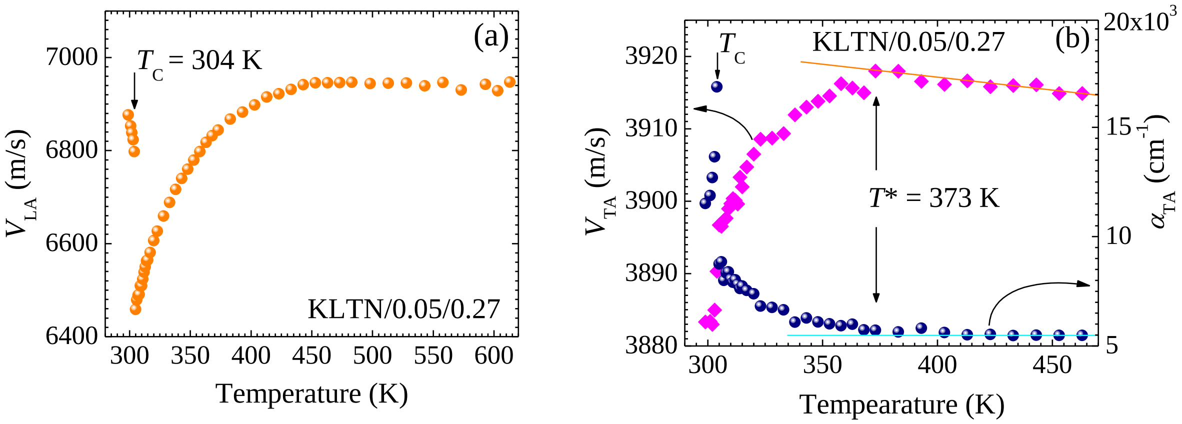

Fig. 4.1.2. Temperature dependence of (a) sound velocity of the LA mode and (b) sound velocity and attenuation of the TA mode in a KLTN/0.05/0.27 single crystal. The solid lines in (b) are guide to eyes.

Upon cooling, a significant softening of the V_{LA} and a clear anomaly in the vicinity of the T_C = 304 K were observed, while V_{TA} showed a small discontinuity and only the slight softening towards T_C, indicating the nature of a first order phase transition.[6] The nature of the first order ferroelectric phase transition of a high quality KTN single crystal was also reported by the ultrasonic measurement.[10] According to the phase diagram of KTN,[11] the expected T_C of the KTN/0.27 is about 222 K. However, in 5%Li-doped KTN (KLTN/0.05/0.27) the value of T_C is increased by 82 K, although the Nb concentrations are equal. The increase of the T_C indicates that the ferroelectric instability of KTN is enhanced by the Li-doping. Hofmeister *et al.* reported the marked increase of the T_C of the KTN/0.65 single crystal by the Li-doping.[12] The remarkable softening of the V_{LA} and V_{TA} can be caused by the piezoelectric coupling of LA and TA modes with the fluctuations of the local polarization in PNRs, respectively.[6,13] It is seen from Fig. 4.1.2 that the V_{LA} begins to soften at the higher temperature than that of the V_{TA}, implying that the piezoelectric interactions might be different between the LA and TA modes.[14] In addition, the V_{TA} showed a linear decrease upon heating above the T^* as shown in Fig. 4.1.2(b). Since the V_{TA} starts to soften at the T^* by the piezoelectric coupling between the fluctuating PNRs and the TA mode, therefore, noticeable coupling is not expected between the TA mode and fluctuating PNRs in the temperature range above the T^*.[14] The mild variation of the TA mode in this temperature range can be mainly dominated by the third order lattice anharmonicity as similar to thermal expansion. The lattice anharmonicity refers to the vibrational effects that do not follow simple harmonic motion. Such a behavior was also observed in PMN, $Pb(Mg_{1/3}Ta_{2/3})O_3$ (PMT), and $0.955Pb(Zn_{1/3}Nb_{2/3})O_3$-$0.045PbTiO_3$ (PZN-0.045PT) single crystals.[14] In a paraelectric phase below the $T^* \sim 373$ K, the CP intensity drastically increases toward T_C upon cooling, indicating the start of rapid growth of volume fraction of PNRs.[6,13] The sudden growth of PNRs also induces the significant softening of the V_{TA} and the remarkable increase of the α_{TA} from T^* to T_C as shown in Fig. 4.1.2(b). In the vicinity of the T_C, the softening of the sound velocity and the significant increase of the attenuation in a cubic phase owing to piezoelectric coupling between acoustic modes and polarization fluctuations in PNRs were observed in various lead-based relaxor.[14-16]

4.1.3.2 Li-doped effect on elastic constants and attenuation

The elastic constants were calculated from the sound velocities using the following equations:

$$C_{11} = \rho V_{LA}^2 \,, \qquad (4.1.1)$$

$$C_{44} = \rho V_{TA}^2 \,, \qquad (4.1.2)$$

where ρ is the density of a crystal. The value of density, ρ = 6630 kg/m^3, was used to calculate the elastic constants of KLTN/0.05/0.27,[3] whereas ρ = 6078.65 kg/m^3 was used for KTN/0.40.[17] The temperature dependences of the elastic stiffness constant C_{11} of the Li-doped and the non-doped KTN are shown in Fig. 4.1.3.

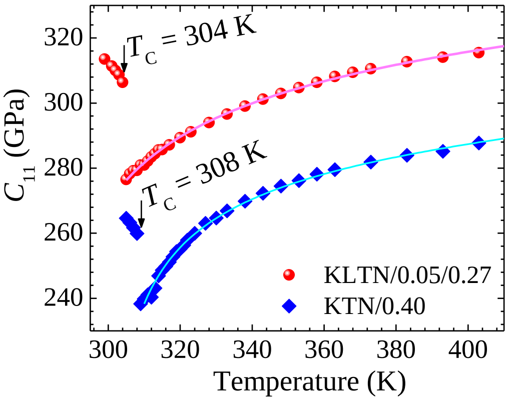

Fig. 4.1.3. Elastic constant C_{11} of both KLTN/0.05/0.27 and KTN/0.40 single crystals as a function of temperature. The solid lines are the best fit result obtained by Eq. (4.1.3).

At 298 K, the value of C_{11} of the KTN/0.40 was 269 GPa reported in Ref. 6, while for KLTN/0.05/0.27, C_{11} = 313 GPa. It is found that the value of the elastic constants of the Li-doped KTN is larger than that of the non-doped one in the whole temperature range. However, it is readily seen from Fig. 4.1.3 that the temperature region of the elastic anomaly was broadened by the Li-doping. This result indicates that Li-doping increases the temperature region on the growth of PNRs. In Li-doped KTN, therefore, the observed broadening of the elastic anomaly can be the evidence of the extension of the temperature region of the elastic anomaly in comparison to that of the non-doped KTN. In order to show the effects of Li ions in the KTN single crystals, we also studied the sound attenuation of the acoustic phonons. On fitting spectra using Lorentzian functions, it was difficult to make reliable data of the damping of the LA mode because of its asymmetric nature. Therefore, we were concentrated to the damping of the TA mode. Figure 4.1.4 shows the α_{TA} of the Li-doped and the non-doped KTN as a function of T/T_C. It is clearly seen from Fig. 4.1.4 that the α_{TA} increases by the Li-doping. This means that the TA phonons were markedly scattered by the Li-doping. These results suggest that the Li ions enhance the growth of PNRs. It is significant that the temperature interval between T_C and T^* was increased by the Li-doping as shown in Fig. 4.1.4. The extension of the temperature interval between T_C and T^* can be attributed to the enhanced stability of PNRs, induced by Li ions. The enhanced stability of PNRs by the Li-doping induces the broadening of elastic anomaly, which can be the evidence of the enhanced relaxor nature of 5%Li-doped KTN single crystals.

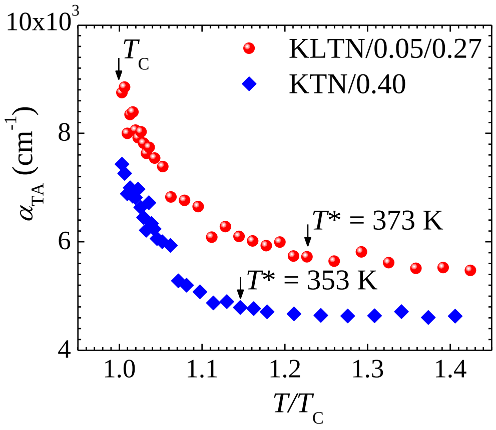

Fig. 4.1.4. The attenuation of the TA mode in the KLTN/0.05/0.27 and KTN/0.40 single crystals as a function of T/T_C.

4.1.3.3 Critical index of elastic constant

In order to rationalize the remarkable elastic anomaly by the PNRs, the C_{11} curves of the KLTN/0.05/0.27 and KTN/0.40 single crystals (Fig. 4.1.3) were fitted by the following equation:[18-20]

$$C_{11} = A_1 + A_2 T - A_3 (T - T_0)^{-n}. \qquad (4.1.3)$$

The anharmonic behavior is described by the second term. The third term describes the critical softening due to polarization fluctuations in PNRs, where A_3 is the amplitude of the elastic anomaly. The value of the critical exponent n was predicted to be 1.5 for one dimensional fluctuations, 1.0 for two dimensional fluctuations and 0.5 for three dimensional fluctuations.[10] The temperature, T_0 extrapolated in a cubic phase was determined by fitting the V_{LA} with the equation reported by Kashida *et al.*[21] The parameters obtained by the fitting of C_{11} are given in Table 4.1.1. A good consistency between the experimental data and the fitting result was obtained with an exponent of 0.5 indicating three dimensional fluctuations of polarization in a cubic phase. The fitting results are in good agreement with the values reported in Ref. 18.

Table 4.1.1. Fitting parameters of C_{11} to Eq. (4.1.3) for the KLTN/0.05/0.27 and KTN/0.40 single crystals.

	A_1 (GPa)	A_2 (GPa)	A_3 (GPa)	T_0 (K)	n
KLTN/0.05/0.27	326.68 ± 5.20	0.053 ± 0.011	358.92 ± 10.50	276	0.5
KTN/0.40	285.78 ± 7.56	0.064 ± 0.018	242.55 ± 8.49	297	0.5

It is worthy to compare the value of the A_3 of the Li-doped KTN with the non-doped KTN. The amplitude of the anomalous part was markedly increased by the Li-doping as shown in Table 4.1.1. In Li-doped KTN, the remarkable increase of the amplitude of the elastic anomaly can be the clear evidence of the extension of the temperature region of the elastic anomaly in comparison to that of the non-doped KTN. It is also found from Table 4.1.1 that the lattice anharmonicity is decreased by the Li-doping. To show the effects of Li ions on the nature of the phase transition, we compare the values of the difference between T_C and T_0 i.e., $\Delta T = T_C - T_0$ in the case of Li-doped and non-doped KTN. In the case of a second order phase transition, it holds that $T_C = T_0$, while for a first order phase transition $T_0 < T_C$. In both cases, the lower value of T_0 in comparison to T_C (Table 4.1.1) is the clear indication of the first order nature of a ferroelectric phase transition. However, it was seen that the value of ΔT markedly increased by the Li-doping. This result demonstrates that the first order nature of a ferroelectric phase transition is enhanced by the Li-doping

4.1.3.4 Central peak and size of dynamic PNR

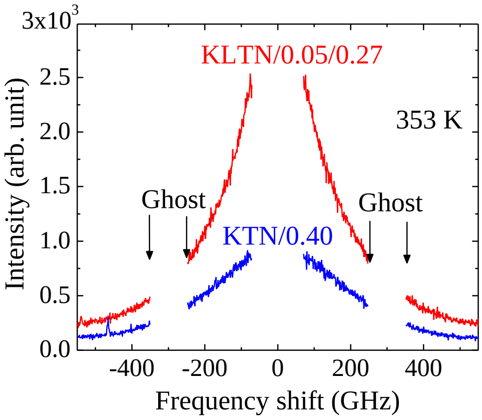

Fig. 4.1.5. The CP spectra of the KLTN/0.05/0.27 and the KTN/0.40 single crystals measured in the FSR = 300 GHz at 353 K.

In order to have a better understanding of the effects of Li ions, we also study the temperature dependence of the CP, which is related to the relaxation process of polarization fluctuations in PNRs. The CP spectra of the KLTN/0.05/0.27 and KTN/0.40 single crystals at 353 K are shown in Fig. 4.1.5. The CP spectrum was fitted by the Voigt function centered at zero. At high temperatures in the cubic phase, the Brillouin spectra of the CP were almost flat and did not show any significant change during the temperature variation. However, the CP developed upon cooling as shown in Fig. 4.1.6. In relaxor-like ferroelectrics, the CP which begins to appear well above T^* is attributed to the relaxational dynamics of PNRs.[6,13] As shown in Fig. 4.1.6, the increase of the intensity of the CP upon cooling reflects the increase of the correlation among PNRs. It was found that the CP intensity became stronger by the Li-doping as shown in Fig. 4.1.6. The marked increase of the CP intensity of the Li-doped KTN is due to the growth of PNRs, which is induced by Li ions.

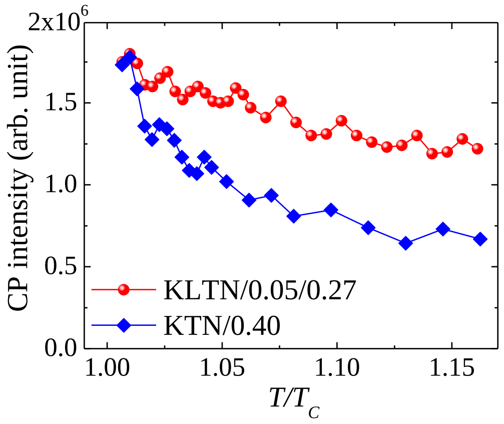

Fig. 4.1.6. The intensity of the CP of the KLTN/0.05/0.27 (solid circles) and KTN/0.40 (solid diamonds) single crystals as a function of T/T_C.

In order to clarify the effects of the Li-doping on PNRs, we estimated the size of the dynamic PNR of the Li-doped KTN crystals and compared with the non-doped one. In RFEs, the dynamic PNRs play the dominant role in the high frequency local dynamics on a nanometer length scale. The size of a dynamic PNR, l_{PNR}, was estimated by the equation, $l_{PNR} = V_{LA} \times \tau_{CP}$, because the characteristic length of polarization flipping can be given by the propagation length of local strain in the period of relaxation time.[22]

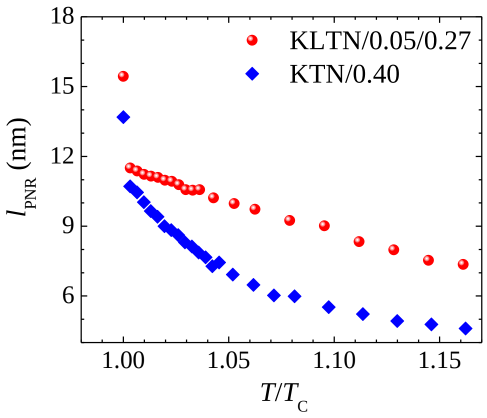

Fig. 4.1.7. Size of a dynamic PNR of the KLTN/0.05/0.27 and KTN/0.40 crystals as a function of T/T_C.

The relaxation time, τ_{CP}, was determined from the FWHM (full width at half maximum) of the CP by the relation, $\pi \times (\text{CP FWHM}) \times \tau_{CP} = 1$.[23] Figure 4.1.7 shows the l_{PNR} of the Li-doped and the non-doped KTN as a function of T/T_C. It is apparent from Fig. 4.1.7 that the size of the dynamic PNR markedly increased by the Li-doping. Therefore, it is concluded that the intense CP of the Li-doped KTN in comparison to that of the non-doped KTN can be attributed to the enhanced growth of PNRs, which is induced by Li ions.

4.1.3.5 Dielectric anomaly

To confirm the enhanced relaxor nature of KTN by the Li-doping, we also performed the comparative study of the dielectric properties between 5%Li-doped and non-doped KTN single crystals. The inverse of the real part of the dielectric constant of KTN/0.40 and KLTN/0.05/0.26 crystals is displayed in Fig. 4.1.8.

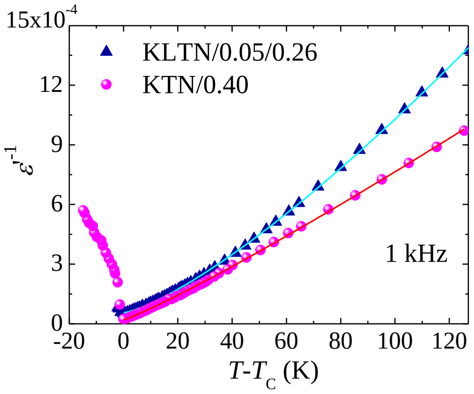

Fig. 4.1.8. The real part of the complex dielectric constant of KTN/0.40 and KLTN/0.05/0.26 single crystals measured at 1 kHz as a function of normalized temperature. The solid lines denote the best fitted lines with the Eq. (4.1.6).

The dielectric constants of KTN/0.40 and KLTN/0.05/0.26 crystals attain a maximum at about 308 K and 294 K, respectively, which correspond to the T_C. These values are consistent with the Brillouin scattering results. It is found that the T_C of the KLTN/0.05/0.26 crystal is lower than that of the KLTN/0.05/0.27 crystal. The lower value of the T_C of the KLTN/0.05/0.26 crystal is due to the lower Nb concentrations. Above T_C, the temperature dependence of the dielectric constant was extensively studied to characterize the dielectric relaxation behavior of RFEs.[24-26] Unlike, in normal ferroelectrics whose dielectric constant above the T_C follows the well-known Curie-Weiss law $1/\varepsilon = (T-T_C)/C$, where C is the Curie constant; in RFEs this law was observed only at temperatures higher than the T_B.[26,27] Below the T_B, the dielectric constant in the paraelectric phase of the relaxor-like ferroelectrics can be explained using Eq. (1.12). As can be seen in Fig. 4.1.8, the inverse of the dielectric constant of both Li-doped and non-doped KTN crystals is well fitted by the Eq. (1.12), indicating relaxor-like behavior of the KTN and the Li-doped KTN single crystals. To clarify the effect of Li-doping on relaxor natures of KTN crystals, it is worthy to compare the values of fitting parameters (Table 4.1.2) obtained by the Eq. (1.12).

Table 4.1.2. The obtained fitting parameters for the dielectric constant of KTN/0.40 and KLTN/0.05/0.26 single crystals using Eq. (4.1.6).

	ε_m	$T_m = T_C$ (K)	γ	δ
KLTN/0.05/0.27	18040	294	1.31 ± 0.005	3.45 ± 0.068
KTN/0.40	50106	308	1.12 ± 0.006	1.51 ± 0.074

It is apparent from Table 4.1.2 that the parameters denoting the degree of diffuseness of the phase transition are markedly increased by the Li-doping in KTN, implying the enhanced relaxor nature of KTN induced by the Li-doping. This may be attributed to the enhanced growth of PNRs, which is induced by the Li ions.

4.2 *Site Occupancy of Li Ions in 5%Li-Doped K(Ta$_{1-x}$Nb$_x$)O$_3$ Single Crystals Proved by Inelastic Light Scattering and First-Principles Calculation*

4.2.1 Introduction

The understanding of the doping effect of the perovskite oxide ferroelectrics is one of the most attractive topics, which is important for both fundamental physics and engineering related to their outstanding functionality.[28-30] Recently, there has been a great deal of interest and challenge to understand the doping effect of oxide ferroelectric materials, especially, investigating the relationship among the site occupancy, charge and size mismatch of the cations at the crystallographic equivalent sites, which are the origins of the relaxor nature of relaxor ferroelectrics (RFEs).[31,32]

Nowadays, the Li-doped KTN is an interesting system for investigating the effects of the Li ions on the physical properties related to a ferroelectric phase transition. The dielectric, piezoelectric, and electro-optic properties were reported on the Li-doped high quality KTN crystals by assuming the site occupancy of Li ions at A-site.[33-35] In our knowledge, there are no optical or X-ray evidences for the site occupancy of the Li ions at A-site for the Li-doped KTN. By considering the ionic size Samara *et al.* reported that the Ca dopant in KTN the substitution occurs at B-site.[36] Such a site occupancy of cations in perovskite oxides becomes one of current topics of applied physics, for example, in SnTiO$_3$, the occupancy of Sn ions at A- and B- sites was discussed from the energy point of view by first-principles calculations.[37] In this study, we discuss the site occupancy of Li ions in 5%Li-doped KTN single crystals on the basis of the observation of the elastic anomaly and the slowing down using the Brillouin scattering, the change of local symmetry of PNRs by Raman scattering and the first-principles calculations.

4.2.2 Methodology

4.2.2.1 Experimental

For angular dependence of Raman scattering spectra, a polarization rotation device (Sigma Koki) equipped with a broadband half-waveplate (Kogakugiken) was used. The Raman spectra were measured at a back scattering geometry using a single-monochromator (Lucir) combined with a charge coupled device (CCD, Andor) and the xyz mapping stage (Tokyo Instruments) installed in the microscope (Olympus). The two volume Bragg gratings so called "ultra narrow-band notch filters" (OptiGrate) were used to reduce the strong elastic scattering. A diode-pumped solid state (DPSS) laser with a wavelength of 532 nm was used to excite the sample which was inserted in a compact heating/cooling stage (Linkam THMS600).

4.2.2.2 Theoretical

The first-principles calculations were carried out using the density functional theory (DFT)[38,39] based CASTEP code.[40,41] The ultrasoft pseudopotential formalism of Vanderbilt was used to simulate the interactions of valence electrons with ions cores within the generalized gradient approximation (GGA), and the electron wave function was expanded in plane waves up to an energy cutoff of 500 eV. In

CASTEP, the choice of exchange-correlation functions (ECFs) is crucial for precision in energy calculation. Since the experimental lattice parameters of the KTN/0.27 crystal were not available, therefore, before calculating the total energy of Li-doped KTN/0.27 (x = 0.27) single crystals, a geometry optimization of KTN/0.33 crystal was carried out by Broyden-Fletcher-Goldfarb-Shannon (BFGS) algorithm using various ECFs to obtain the best cell parameters and compared with the experimental one. The ECF which induced the best results of KTN/0.33 was used to calculate the total energy of Li-doped KTN/0.27 crystals. All the structures were relaxed during geometry optimization. The 14×14×14 Monkhorst-Pack mesh was employed for the sampling of the Brillouin zone. The tolerance of energy, force, and displacement was 5×10^{-6} eV/atom, 0.01 eV/Å, and 5×10^{-4} Å during geometry optimization, respectively. The optimized equilibrium lattice parameter of the KTN/0.33 single crystal with different ECFs is listed in Table 4.2.1.

Table 4.2.1. The optimized lattice parameter the KTN/0.33 single crystal calculated with different ECFs and compared with the experimental data reported in Ref. 42.

Space group	Pseudopotential	ECF	Lattice parameter, a (Å)	Expt.^{16}
$Pm\bar{3}m$	Ultrasoft	PBE	4.03669	3.99279
	Ultrasoft	RPBE	4.10256	
	Ultrasoft	PW91	4.02924	
	Ultrasoft	WC	3.97921	
	Ultrasoft	PBESOL	3.97782	

4.2.3 Results and discussion

4.2.3.1 Acoustic anomaly

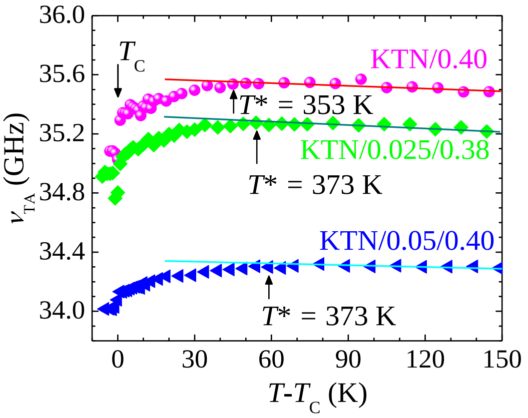

Fig. 4.2.1. The TA frequency shift of KTN/0.40, KLTN/0.025/0.38, and KLTN/0.05/0.27 single crystals as a function of normalized temperature. The solid lines are guide to eyes.

For better understanding the Li-doping effects in KTN, the comparative study among the non-doped KTN/0.40, 2.5%Li-dope KTN/0.38 (KLTN/0.025/0.38) and KLTN/0.05/0.27 single crystals was performed using Brillouin and Raman scattering. The temperature dependences of the TA frequency shift,

υ_{TA}, of KTN/0.40, KLTN/0.025/0.38, and KLTN/0.05/0.27 crystals are shown in Fig. 4.2.1. It is worth noting that the υ_{TA} shows the linear temperature behaviors at very high temperatures. While upon cooling the υ_{TA} starts to deviate from the high temperature linearity, reaches a maximum value near the $T^* \sim 373$ K and 353 K for the Li-doped and the non-doped KTN, respectively. For further cooling they show a significant softening towards T_C. The remarkable softening of the υ_{TA} just above T_C is caused by the piezoelectric coupling between the fluctuating PNRs and the TA/LA phonons.[6,13] These behaviors are very similar to those observed in the relaxor ferroelectric PZN-0.045PT and the PZN-0.09PT single crystals.[14] It was also found that the acoustic damping of the LA phonon of KTN/0.40 begins to increase below the $T^* \sim 353$ K upon cooling.[6] In addition, the clear anomalies of the υ_{TA} were observed at $T_C = 304$ K, 308 K and 319 K of KLTN/0.05/0.27, KTN/0.40, and KLTN/0.025/0.38 crystals, respectively as shown in Fig. 4.2.1. According to the phase diagram of KTN,[11] the expected T_C of KTN/0.27 and KTN/0.38 crystals is about 222 K and 297 K, respectively. However, the value of T_C is increased about 82 K and 22 K in KLTN/0.05/0.27 and KLTN/0.025/0.38 crystals, respectively, albeit the concentrations of Nb are equal. The increase of the T_C indicates that the Li-doping stabilizes the ferroelectricity of KTN. The significant increase of the T_C of the KTN/0.65 single crystal by the Li-doping was also reported in Ref. 12. It is significant that acoustic phonons were markedly scattered by the Li-doping, thus the attenuation increase while υ_{TA} slightly decreases by the Li ions as shown in Fig. 4.2.1. This fact suggest that Li-doping enhance the growth of PNRs.[43] It is also important to note that the temperature interval between T_C and T^* was gradually increased by the Li-doping as shown in Fig. 4.2.1. The extension of this temperature region can be attributed to the enhanced stability of PNRs, induced by the Li ions.

4.2.3.2 Critical slowing down

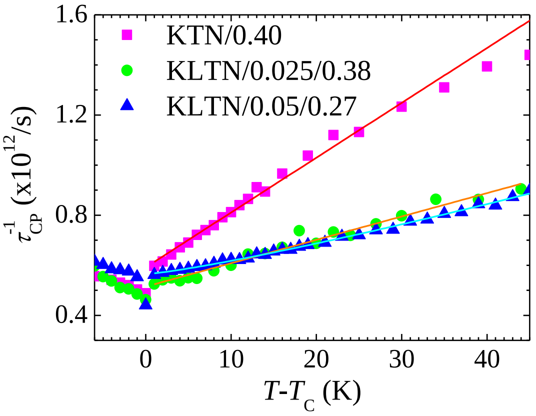

Fig. 4.2.2. The inverse of the relaxation time determined from the CP width in KTN/0.40, KLTN/0.025/0.38, and KLTN/0.05/0.27 single crystals as a function of normalized temperature. The solid lines are the fitted lines by the Eq. (4.2.1).

The temperature dependences of the inverse relaxation time determined from the width of the CP in the Li-doped and the non-doped KTN single crystals are shown in Fig. 4.2.2. It was seen that the inverse of the relaxation time showed the stretched-type slowing down only in the 5%Li-doped KTN, while 2.5%Li-doped KTN and the non-doped KTN showed the normal critical slowing down. Such a stretched-type slowing down behavior of the relaxation time under the influence of random fields might be described by the following empirical relation:[22]

$$\frac{1}{\tau}=\frac{1}{\tau_0}+\frac{1}{\tau_1}\left(\frac{T\text{-}T_C}{T_C}\right)^{\beta}, \quad (\beta \geq 1) \text{ for } T > T_C \tag{4.2.1}$$

where β is the stretched index related to the random fields. β = 1.0 means the normal critical slowing down without random fields and it assumes values > 1 depending on the strength of the random fields. The observed relaxation time (Fig. 4.2.2) is well fitted by the Eq. (4.2.1) implying the order-disorder nature of the ferroelectric phase transition.[18,19] The best fitted results using Eq. (4.2.1) are listed in Table 4.2.2. The observed value of the β more than 1.0 in 5%Li-doped KTN can be attributed to the enhanced random fields by the Li-doping. The microscopic origin of the enhanced random fields in 5%Li-doped KTN can be the hetero-valence charge disorder at B-site, which is induced due to the partial occupancy of Li ions at B-site.

Table 4.2.2. The best fitted parameters obtained from the inverse relaxation time using Eq. (4.2.1) for KTN/0.40, KLTN/0.025/0.38, and KLTN/0.05/0.27 single crystals.

	τ_0 (ps)	τ_1 (ps)	β	T_C (K)
KTN/0.40	1.63 ± 0.021	14.78 ± 0.03	1.0	308
KLTN/0.025/0.38	1.90 ± 0.025	2.32 ± 0.078	1.0	319
KLTN/0.05/0.27	1.77 ± 0.009	4.83 ± 0.09	1.18 ± 0.03	304

4.2.3.3. Angular dependence of Raman scattering spectra

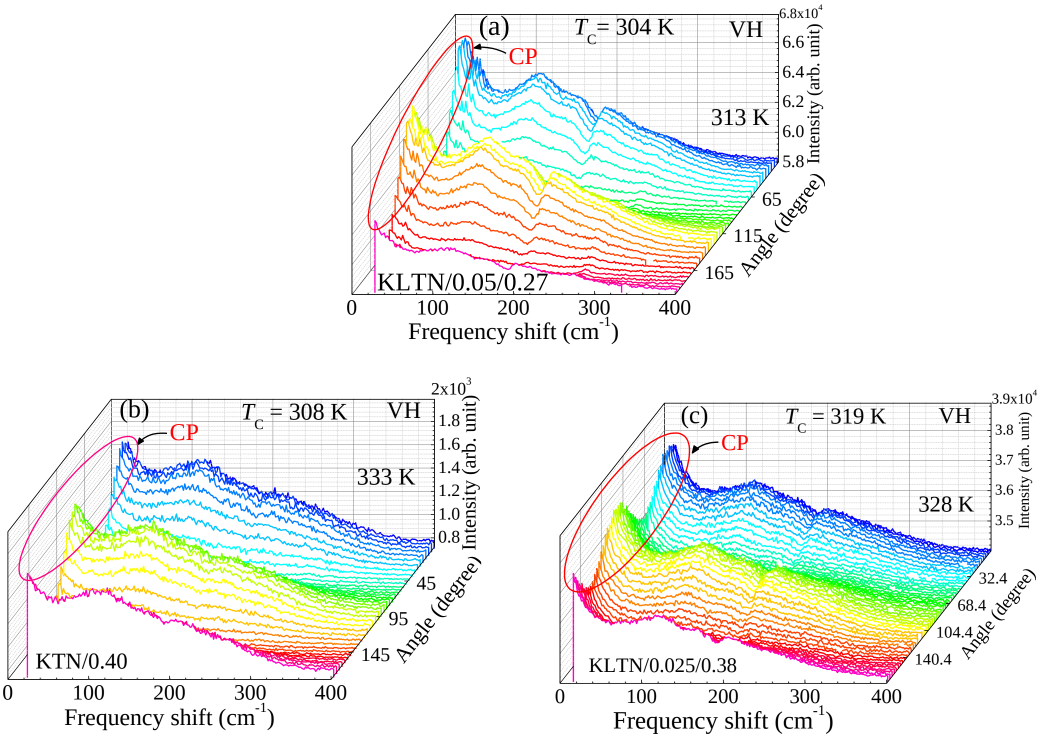

Fig. 4.2.3. Angular dependence of $a(bc)\bar{a}$ (VH) Raman scattering spectra of (a) KLTN/0.05/0.27, (b) KTN/0.40, and (c) KLTN/0.025/0.38 single crystals measured in the cubic phase.

In order to have a better understanding the partial occupancy of Li ions in 5%Li-doped KTN crystals, we also performed comparative study between Li-doped and non-doped KTN crystals by Raman scattering. The angular dependence of $a(bc)\bar{a}$ (VH) Raman scattering spectra in the cubic phase of KTN/0.40, KLTN/0.025/0.38, and KLTN/0.05/0.27 crystals is shown in Fig. 4.2.3. By the rotation of the plane of polarization, the angular dependence of Raman spectra exhibits the sinusoidal tendency, implying the anisotropy of Raman scattering of both non-doped and Li-doped KTN crystals. In particular, the remarkable variation of the CP intensity of Li-doped and non-doped KTN single crystals was observed with the rotation of the plane of polarization. It is worth noting that the variation of the intensity of the CP observed in VH scattering was in phase between non-doped and 2.5%Li-doped KTN, while the variation of the intensity of the CP was out of phase between 5%Li-doped and non-doped KTN crystals (Fig. 4.2.3). To figure out the physical origin of the CP of non-doped and Li-doped KTN crystals, all spectra were fitted by the Eq. (3.7). The angular dependence of the observed intensity of the CP of the KTN/0.40, KLTN/0.025/0.38, and KLTN/0.05/0.27 single crystals is displayed in Fig. 4.2.4.

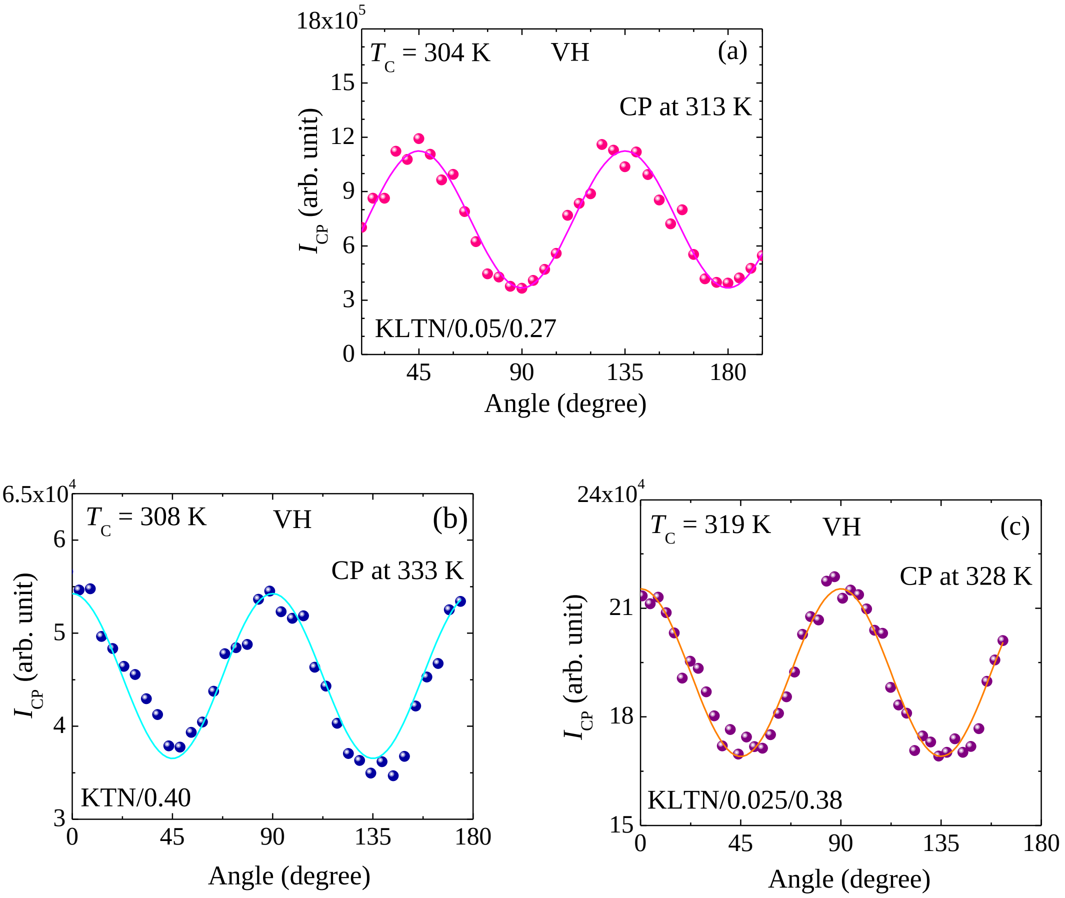

Fig. 4.2.4. The integrated intensity of the CP of (a) KLTN/0.05/0.27, (b) KLTN/0.40, and (c) KLTN/0.025/0.38 single crystals measured in the cubic phase. The solid line in (a) is the best fitted line using the Eq. (3.13). The solid lines in (b) and (c) denote the best results fitted by the Eq. (3.11).

In KTN/0.40 and KLTN/0.025/0.38 single crystals, the intensity of the CP obtained from the VH spectra is well fitted by the Eq. (3.11), while the change of the intensity of the CP of the KLTN/0.05/0.27 crystal is fitted by the Eq. (3.13) as shown in Fig. 4.2.4. A good consistency between experimental data and the fitting result by the theory via Eqs. (3.11) and (3.13), implying that the CP in the cubic phase of

KTN/0.40 and KLTN/0.025/0.38 crystals stem from the A_1(z) symmetry of PNRs, while in the case of KLTN/0.05/.27 crystal the CP comes from the $E(x,y)$ symmetry of PNRs with a rhombohedral *R3m* symmetry. By Brillouin scattering, the intense CP of the KLTN/0.05/0.27 single crystal was observed in comparison to that of the non-doped one, which attributed to the growth of PNRs.[43] The angular dependence of Raman scattering results suggests that the intense CP of the KLTN/0.05/0.27 crystal can be due to the transformation of local symmetry of PNRs in addition to the growth of PNRs. In KTN/0.28, Sokoloff *et al.* reported that the CP intensity caused by the *E*-symmetry fluctuations is more intense than the *A*-symmetry fluctuations.[44]

It is significant to clarify the microscopic origin of the change of local symmetry of PNRs in KLTN/0.05/0.27 single crystal. The PNRs in KTN can be induced only by off-center displacements of Nb ions at the B-site corresponding to one set of atomic displacements, hence the $A_1(z)$ symmetry of PNRs is reasonable in the case of KTN crystals. On the other hand, in Li-doped KTN crystals, it is believed that off-center displacements of Li ions occur along the equivalent [100] directions at the A-site. The off-center displacements of Li ions along equivalent [100] directions at A-site was reported in Refs. 2 and 45. However, the local [100] displacements are correlated in the medium range with the [111] displacements, and on an average Li ions for the [100], [010], and [001] displacements is along an equivalent [111] directions.[46] In KLTN/0.025/0.38, the doping of small amount of Li in KTN may comprise an additional polarization due to the off-center displacements of Li ions at A-site. This additional polarization is cooperative with the neighboring polar clusters resulting in a larger polar cluster that suppress the phonon frequency as shown in Fig. 4.2.2.[47] Therefore, up to 2.5%Li doping in KTN, the invariant local symmetry of PNRs may due to the occupancy of Li ions at A-site only. In 5%Li-doped KTN, the stretched type critical slowing down near T_C was observed by the strong random fields and we speculated that a few percentage of Li ions may be occupied at B-site. Hence, it is expected that there is a strong interactions between Li and Nb ions in a fluctuating PNRs corresponding to two sets of atomic displacements result in the $E(x,y)$ symmetry of PNRs in 5%Li-doped KTN crystals. These results are similar to those observed in a PMN single crystal, in which off-center displacements of cations occur at both A- and B-site whereas charge disorder exist at B-site.[48]

4.2.3.4 First-principles calculation on the site occupancy of Li ions

It is very important to discuss the microscopic origin of the enhanced random fields and transformation of local symmetry of PNRs in 5%Li-doped KTN on the basis of the structural viewpoint. In the non-doped KTN of the perovskite structure, the A-site is occupied by the larger K^{1+} ions (ionic radius 1.38 Å) and B site is occupied by smaller Ta^{5+} (ionic radius 0.64 Å) and Nb^{5+} ions (ionic radius 0.64 Å). The B-site cations have comparable sizes and homovalent, KTN possesses no charge disorder. Therefore, its random fields[49] is too weak to suppress the critical slowing down. In the Li-doped KTN, the Li^{1+} (ionic radius 0.76 Å) would be expected to substitute for K^{1+} at A-site owing to the similar chemistry between K^{1+} and Li^{1+}. However, the size consideration of the perovskite structure could make the A-site occupation slightly unfavorable.[36] Therefore, there is a probability of partial occupancy of Li ions at B-site. Since the energy of a unit cell is the key parameter for an equilibrium structure, therefore, the total energy of the Li-doped KTN/0.27 was evaluated by the first-principles calculations. As can be seen in Table 4.2.1, the calculated value of the lattice parameter of the KTN/0.33 with GGA/PBESOL is the good agreement with the experimental one among five ECFs. Therefore, the total energy of the KTN/0.27 by the Li-doping was carried out with the GGA/PBESOL. For better understanding the microscopic origin of the enhanced random fields, at first, the calculation of total energy of the KTN/0.27 was performed by the Li-doping at A-site. It is clearly seen from Fig. 4.2.5(a) that the total energy decreases by the Li-doping and exhibits minimum when the Li content was 4.9% at A-site (see the expanded view in the inset). This result can be the evident of the occupancy of Li ions at A-site only in 2.5%Li-doped KTN crystal.

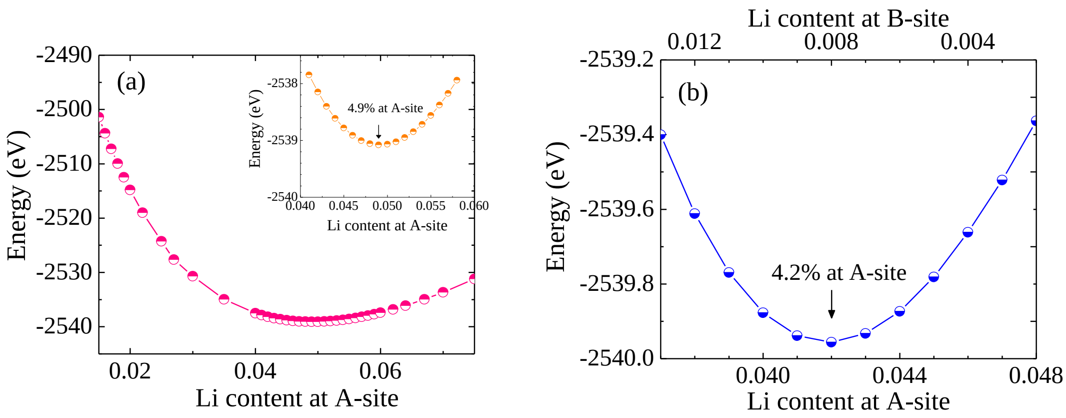

Fig. 4.2.5. The calculated total energy per formula unit vs. the Li content (a) at A and (b) at A and B-sites of the 5% Li-doped KTN single crystal.

However, the energy begins to increase above the 4.9%Li doing at A-site [Fig. 4.2.5(a)] and this result stimulate to investigate the partial occupancy of Li ions at B-site in 5%Li-doped KTN/0.27 crystal. In order to clarify the B-site occupancy of Li ions in part, we calculated the energy of the Li occupancy at both A and B-sites. It is significant that the total energy shows more minimum value when the substitution level was 4.2% at A-site and 0.8% at B-site as shown in Fig. 4.2.5(b). Based on this result we can propose that 0.8% Li ions occupy at B-site in the KLTN/0.05/0.27 single crystals. In the 5%Li-doped KTN, therefore, the strength of random fields increases essentially by the hetero-valence charge disorder at B-site, which suppresses the critical slowing down of the relaxation time near T_C and change the local symmetry of PNRs. This can also be the reason of the extension of the temperature region between T_C and T^* and the enhanced diffusive nature of the ferroelectric phase transition of the KLTN/0.05/0.27 single crystals. In RFEs, the suppression of the critical slowing down of the relaxation time by the random fields was reproduced by the stretched-type slowing down near T_C.[22] Since the random fields are implicated as the genesis of relaxor behavior,[50] the stretching of the slowing down by the random fields can be the manifestation of the enhanced relaxor nature of KLTN/0.05/0.27, which is mainly dominated by the partial occupancy of Li ions at B-site.

4.3 Summary

By the comparative study between 5%Li-doped KTN and non-doped KTN, the effects of Li-doping on KTN crystals were clearly observed by the broadening of elastic anomaly and stretching of slowing down by Brillouin scattering and the transformation of local $A_1(z)$ symmetry to $E(x,y)$ symmetry of PNRs by Raman scattering. In Li-doped KTN, the enhanced temperature interval of the elastic anomaly may be attributed to the fact that the random fields by doped Li ions increase the growth of PNRs. The significant increase of the size of the dynamic PNRs towards T_C was found by the Li-doping. The enhanced stability of PNRs by the Li-doping induces the broadening of elastic anomaly, which can be the evidence of the enhanced relaxor nature of 5%Li-doped KTN single crystals. By the Li-doping, the enhanced relaxor nature of KTN was also confirmed by the dielectric properties. By 5%Li-doping to KTN, the first-principles calculation revealed that 4.2%Li ions occupy at A-site, while the rest of 0.8%Li ions occupy at B-site in a stable equilibrium state. Therefore, the hetero-valence random occupation of 0.8%Li ions at B-site can be the microscopic origin for the increase of the random field strength, which suppresses the critical slowing down of the relaxation time near T_C and changes the local symmetry of PNRs.

References

[1]H. Schremmer, W. Kleemann, and D. Rytz, Phys. Rev. B **62,** 1896 (1992).

[2]L. Cai, J. Toulouse, L. Harrier, R. G. Downing, and L. A. Boatner, Phys. Rev. B **91**, 134106 (2015).

[3]Z. Zhou, J. Li, H. Tian, Z. Wang, Y. Li, and R. Zhang, J. Phys. D: Appl. Phys. **42**, 125405 (2009).

[4]J. Li, Y. Li, Z. Zhou, R. Guo, and A. Bhalla, Ferroelctrics **130**, 65 (2011).

[5]T. Imai, S. Toyoda, J. Miyazu, J. Kobayashi, and S. Kojima, Jpn. J. Appl. Phys. **53**, 09PB02 (2014).

[6]M. M. Rahaman, T. Imai, J. Miyazu, J. Kobayashi, S. Tsukada, M. A. Helal, and S. Kojima, J. Appl. Phys. **116**, 074110 (2014).

[7]W. A. Bonner, E. F. Dearborn, and L. G. Van Uitert, Ceram. Bull. **44**, 9 (1965).

[8]S. Kojima, Jpn. J. Appl. Phys. **49**, 07HA01 (2010).

[9]R. Vacher and L. Boyer, Phys. Rev. B **6**, 639 (1972).

[10]J. M. Courdile, J. Dumas, S. Ziolkiewicz, and J. Joffrin, J. Phys. (Paris) **38**, 1519 (1977).

[11]D. Rytz and H. J. Scheel, J. Cryst. Growth **59**, 468 (1982).

[12]R. Hofmeister, A. Yariv, and A. Agranat, J. Cryst. Growth **131**, 486 (1993).

[13]R. Ohta, J. Zushi, T. Ariizumi, and S. Kojima, Appl. Phys. Lett. **98**, 092909 (2011).

[14]J.-H. Ko, D. H. Kim, and S. Kojima, Phys. Rev. B **77**, 104110 (2008).

[15]T. H. Kim, J.-H. Ko, and S. Kojima, Jpn. J. Appl. Phys. **52**, 09KC01 (2013).

[16]S. Kojima and J.-H. Ko, Curr. Appl. Phys. **11**, S22 (2011).

[17]A. Reisman and E. Banks, J. Am. Chem. Soc. **80**, 1877 (1958).

[18]L. A. Knauss, X. M. Wang, and J. Toulouse, Phys. Rev. B **52**, 13261 (1995).

[19]R. O. Bell and G. Rupprecht, Phys. Rev. **129**, 90 (1963).

[20]J. O. Fossum and K. Fossheim, J. Phys. C: Solid State Phys. **18**, 5549 (1985).

[21]S. Kashida, I. Hatta, and A. Ikushima, J. Phys. Soc. Jpn. **34**, 997 (1973).

[22]S. Kojima and S. Tsukada, Ferroelectrics **405**, 32 (2010).

[23]S. Tsukada and S. Kojima, Phys. Rev. B **78**, 144106 (2008).

[24]A. A. Bokov and Z.-G. Ye, Solid State Commun. **116,** 105 (2000).

[25]Z.-Y. Cheng, R. S. Katiyar, X. Yao, and A. Guo, Phys. Rev. B **55**, 8165 (1997).

[26]A. A. Bokov and Z.-G. Ye, J. Adv. Dielectrics **2,** 1241010 (2012).

[27]D. Viehland, S.J. Jang, L.E. Cross, M. Wuttig, Phys. Rev. B **46,** 8003 (1992).

[28]K. M. Rabe, Ch. H. Ahn, and J.-M. Triscone, *Physics of Ferroelectrics*: *A Modern Perspective* (Springer. New York, 2007).

[29]O. Auciello, J. F. Scott, and R. Ramesh, Phys. Today **51**(7), 22 (1998).

[30]T. Imai, S. Yagi, S. Toyoda, J. Miyazu, K. Naganuma, M. Sasaura, and K. Fujiura, Appl. Phys. Express **4**, 022501 (2011).

[31]I. W. Chen, J. Phys. Chem. Solids **61**, 197 (2000).

[32]S. J. Butcher and N. W. Thomas, J. Phys. Chem. Solids **52,** 595 (1991).

[33]G. Bitton, Y. Feldman, A. J. Agranat, J. Non-Cryst. Solids **305**, 362 (2002).

[34]Z. Zhou, J. Li, H. Tian, Z. Wang, Y. Li, and R. Zhang, J. Phys. D: Appl. Phys. **42**, 125405 (2009).

[35]Y. Li, J. Li, Z. Zhou, R. Guo, and A. Bhalla, Ferroelectrics **425**, 82 (2011).

[36]G. A. Samara and L. A. Boatner, Phys. Rev. B **61**, 3889 (2000).

[37]H.Ye, R. Zhang, D. Wang, Y. Cui, J. Wei, C. Wang, Z. Xu, S. Qu and X. Wei, Int. J. Mod. Phys. B **27,** (2013) 1350144.

[38]P. Hohenberg and W. Khon, Phys. Rev. **136,** B864 (1964).

[39]W. Kohn and L. J. Sham, Phys. Rev. **136,** A1133 (1965).

[40]M. D. Segal, P. J. D. Lindan, M. J. Probert, C. J. Pickard, P. J. Hasnip, S. J. Clark, M. C. Payne, J. Phys.: Condens. Matter **14**, 2717 (2002).

[41]M. C. Payne, M. P. Teter, D. C. Allan, T. A. Arias, J. D. Joannopoulos, Rev. Mod. Phys. **64,** 1045 (1992).

[42]X. Wang, J. Wang, Y. Yu, H. Zhang, and R. I. Boughton, J. Cryst. Growth **293**, 398 (2006).

[43]M. M. Rahaman, T. Imai, J. Kobayashi, and S. Kojima, Jpn. J. Appl. Phys. **54,** 10NB01 (2015).

[44]J. P. Sokoloff, L. L. Chase, and L. A. Boatner, Phys. Rev. B **41**, 2398 (1990).

[45]R. Machado, M. Sepliarsky, and M. G. Stachiotti, Phys. Rev. B **86,** 094118 (2012).

[46]I.-K. Jeong, T. W. Darling, J. K. Lee, Th. Proffen, R. H. Heffner, J. S. Park, K. S. Hong, W. Dmowski, and T. Egami, Phys. Rev. Lett. **94,** 147602 (2005).

[47]M. M. Rahaman, T. Imai, J. Miyazu, J. Kobayashi, and S. Kojima, Ferroelectrics, **487**, 47 (2015).

[48]H. Taniguchi, M. Itoh, and D. Fu, J. Raman spectrosc. **42,** 706 (2011).

[49]G. A. Samara, J. Phys.: Condens. Matter **15,** R367 (2003).

[50]D. Phelan, C. Stock, J. A. Rodriguez-Rivera, S. Chi, J. Leão, X. Long, Y. Xie, A. A. Bokov, Z.-G. Ye, P. Ganesh, and P. M. Gehring, PNAS **111**, 1754 (2014).

Chapter 5

The Effect of Electric Field on Fano Resonance of Li-doped $KTa_{1-x}Nb_xO_3$ Single Crystals Investigated by Raman Scattering

5.1 Introduction

The Fano resonance is a general phenomenon which is rather well known, for example, photonics and nonlinear optics, but less documented in materials science. The phenomenon of a Fano resonance results from the interaction between a discrete state and continuum states showing an asymmetry of the spectral line shape.[1] The possible continuum states, that can interfere with the optical phonons and give rise to a Fano resonance, are the two acoustical phonon state,[2] another transverse optic (TO) phonon via acoustic phonons,[3] and the rapid polarization fluctuations in PNRs.[4,5] The Fano resonance in relaxor ferroelectrics $Ba(Zr_{1/2}Ti_{1/2})O_3$ (BZT) was caused by the interaction between the Zr and Ti sublattices studied by Wang *et al.*.[6] In ferroelectric semiconductor $Sn_2P_2Se_6$, the Fano resonance was attribute to the coupling between the central peak (CP) and the TO phonon.[7] Recently, Yoshino *et al.* reported that dynamical coupling between fast-relaxing Rabi oscillations (ROs) and slow-relaxing coherent longitudinal optic (LO) phonon resulting in a Fano resonance in CuCl semiconductor microcavities.[8]

In order to improve the functionality of ferroelectric materials, the investigation of the role of local structure called polar nanoregions (PNRs) is very important.[9] By inelastic light scattering, the dynamical aspect of PNRs was extensively studied in the cubic phase of the KTN crystals.[10-14] However, the microscopic origin of the Fano resonance at around 196 cm^{-1} in not only KTN but also Li-doped KTN crystals still remains unclear. In this study, we investigated the microscopic origin of the Fano resonance in Li-doped KTN crystals using the temperature, angular, and electric field dependences of Raman scattering. The broken symmetry was discussed on the basis of the evolution of the PNRs by the existence of the first order Raman modes in the cubic phase.

5.2 Experimental

The $K_{0.95}Li_{0.05}Ta_{0.73}Nb_{0.27}O_3$ (KLTN/0.05/0.27) and $K_{0.95}Li_{0.05}Ta_{0.74}Nb_{0.26}O_3$ (KLTN/0.05/0.26) single crystals used in the present study were grown by the top seeded solution growth technique at NTT Corporation. The crystals were cut having the size of 4.00×3.20×1.20 mm^3 and 4.00×3.18×1.00 mm^3 with the largest faces perpendicular to the [100] direction, respectively. In KLTN/0.05/0.26 crystal, the platinum electrodes were deposited on the faces perpendicular to the [100] direction to apply the electric field. The Raman scattering was measured at $a(cc)\bar{a}$ (VV) and $a(bc)\bar{a}$ (VH) configurations at a back scattering geometry. A diode pumped solid state (DPSS) laser with a wavelength of 532 nm was used to excite the samples. The temperature and electric field dependences of Raman spectra were measured using a double monochromator (Horiba-JY, U-1000) with the resolution of 1 cm^{-1}. The temperature of the sample was controlled by the heating/cooling stage (Linkam, THMS600) with ±0.1 K accuracy over all temperatures.

For the angular dependence of Raman scattering, the KLTN/0.05/0.27 crystal was put on the *xyz* mapping stage (Tokyo Instruments) inside the Linkam installed in the optical reflection microscope (Olympus). The linearly polarized light from DPSS was incident to the sample through a polarization rotation device (Sigma Koki) equipped with a broadband half-waveplate (Kogakugiken). The strong elastic scattering was highly reduced by two volume Bragg gratings so called "ultra narrow-band notch filters" (OptiGrate). The inelastic scattering light was dispersed by a single-monochromator (Lucir) and the dispersed component was detected using a charge coupled device (CCD, Andor).

5.3 Results

5.3.1 Temperature dependence of Raman scattering spectra

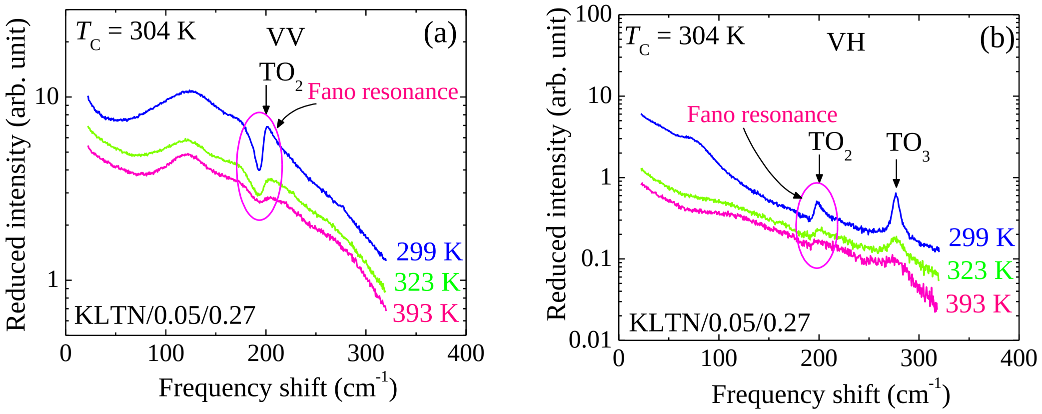

Fig 5.1. Reduced (a) $a(cc)\bar{a}$ (VV) and (b) $a(bc)\bar{a}$ (VH) Raman scattering spectra at some selected temperatures of the KLTN/0.05/0.27 single crystal.

In the analysis of Raman scattering spectra, the reduced intensity, $I^{r}(\omega)$, was calculated from the Stokes component of Raman scattering intensity using Eq. (3.6). In the reduced intensity, the effect of phonon population on spectra can be avoided. The temperature dependence of the reduced $a(cc)\bar{a}$ (VV) and $a(bc)\bar{a}$ (VH) Raman spectra of a 5%Li-doped KTN i.e., $K_{0.95}Li_{0.05}Ta_{0.73}Nb_{0.27}O_3$ (KLTN/0.05/0.27) single crystal is shown in Fig. 5.1. The existence of a prominent first order TO$_2$ mode at about 196 cm^{-1} in both VV and VH spectra and a TO$_3$ mode at around 277 cm^{-1} at 299 K demonstrates that the symmetry of the KLTN/0.05/0.27 single crystal is not cubic $Pm\bar{3}m$ symmetry at room temperature (RT). The detailed mode assignment of the KTN single crystals were studied in Refs. 15-18. According to the phase diagram of KTN,[19,20] a cubic phase is indeed expected for the non-doped KTN/0.27 crystal at RT. However, Li doping raises the Curie temperature (T_C) and the tetragonal phase with $P4mm$ symmetry was reported at RT in KLTN/0.05/0.27.[21] By Raman scattering, the effect of Li-doping on the phase transition of the KTN crystals was also reported by Prater *et al.*.[22]

To investigate the temperature dependence of a central peak (CP), which is related to the precursor dynamics, all Raman spectra were fitted using the Eq. (3.7). Figure 5.2(a) shows the example of fitted curves using Eq. (3.7). The temperature dependence of the reduced intensity, A_{CP}, and FWHM, Γ_{CP}, of the CP observed in the VV scattering spectrum is shown in Fig. 5.2(b). As can be seen in Fig. 5.2(b), the reduced intensity, A_{CP}, of the CP begins to increase below the intermediate temperature, T^* ~ 373 K, upon cooling, reflecting the rapid growth of the volume fraction of PNRs.[11,12,21] In Fig. 5.2(b), the temperature dependence of Γ_{CP}, which is inversely proportional to the relaxation time, becomes narrower remarkably towards the T_C upon cooling, implying the slowing down of the relevant polarization fluctuations in PNRs.

Therefore, the anomaly at around 373 K must reflects a significant change in the dynamical properties of the KLTN/0.05/0.27 crystal upon cooling.

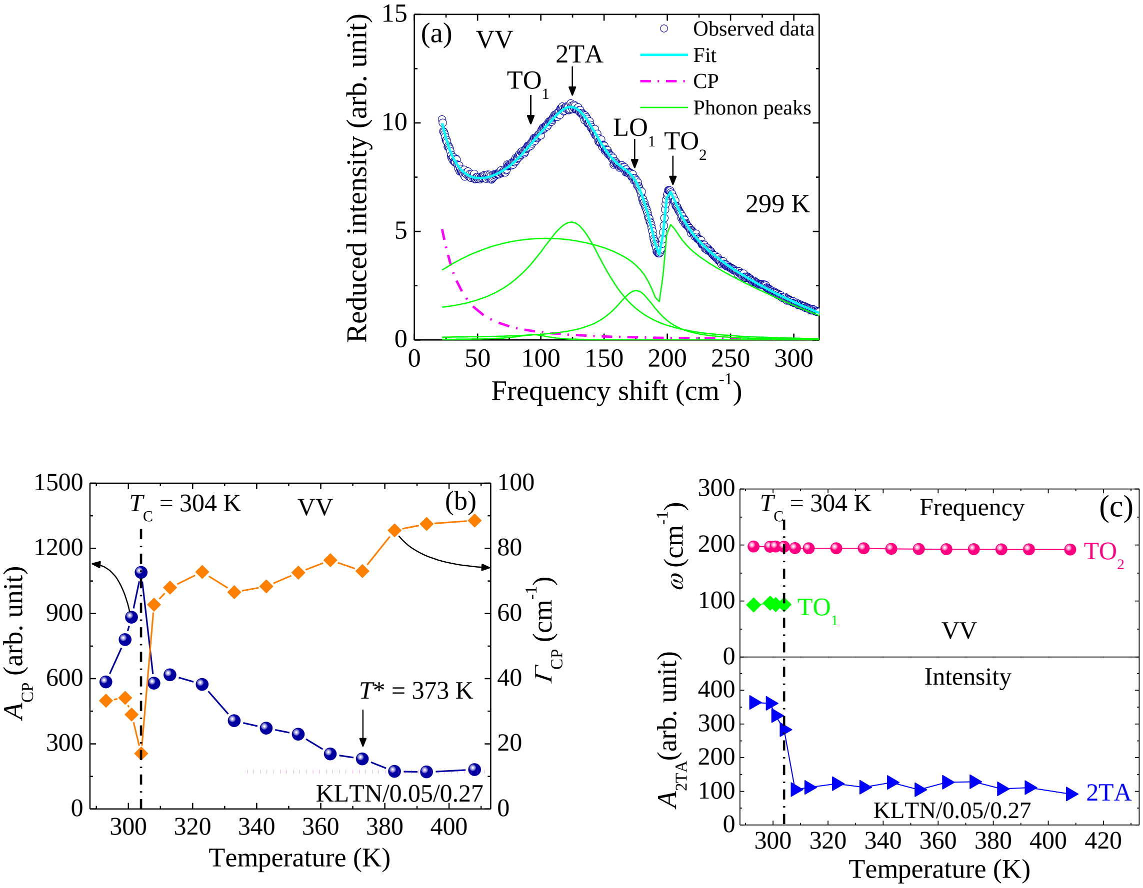

Fig. 5.2. (a) The example of a fitted Raman spectrum of the KLTN/0.05/0.27 single crystal using the Eq. (3.7). (b) Temperature dependence of the integrated reduced intensity and FWHM of the CP at the VV scattering. The dotted and dash-dotted lines in (b) are guide to eyes. (c) The frequency shift of the first order TO_1 and TO_2 modes (upper half) and the variation of the intensity of the 2TA mode (lower half) at the VV scattering of the KLTN/0.05/0.27 crystal as a function of temperature.

It is significant that both A_{CP} and Γ_{CP} exhibit a clear anomaly in the vicinity of the $T_{\mathrm{C}} = 304$ K. Moreover, the first order TO_1 mode in the VV spectra completely vanished at T_{C} upon heating [Fig 5.2(c)], which can be the clear indication of the phase transition of the KLTN/0.05/0.27 single crystal. The similar variation of the intensity and the Γ_{CP} of the CP associated with the precursor dynamics was also observed in $Pb(Zn_{1/3}Nb_{2/3})O_3$ (PZN) single crystal.[23] The values of the characteristic temperatures T_{C} and T^* are in good agreement with the values reported in Ref. 21. It is worth noting that the temperature dependence of the reduced intensity, I_0, of the Fano resonance decreases rather fast in the vicinity of the T_{C} upon heating, while it is still intense above the T_{C} [Figs. 5.3(a) and 5.3(b)], indicating the symmetry breaking caused by the dynamic PNRs. In a typical relaxor, the breaking of symmetry in the cubic phase due to the existence PNRs with rhombohedral *R3m* symmetry was also studied by Raman scattering.[24,25]

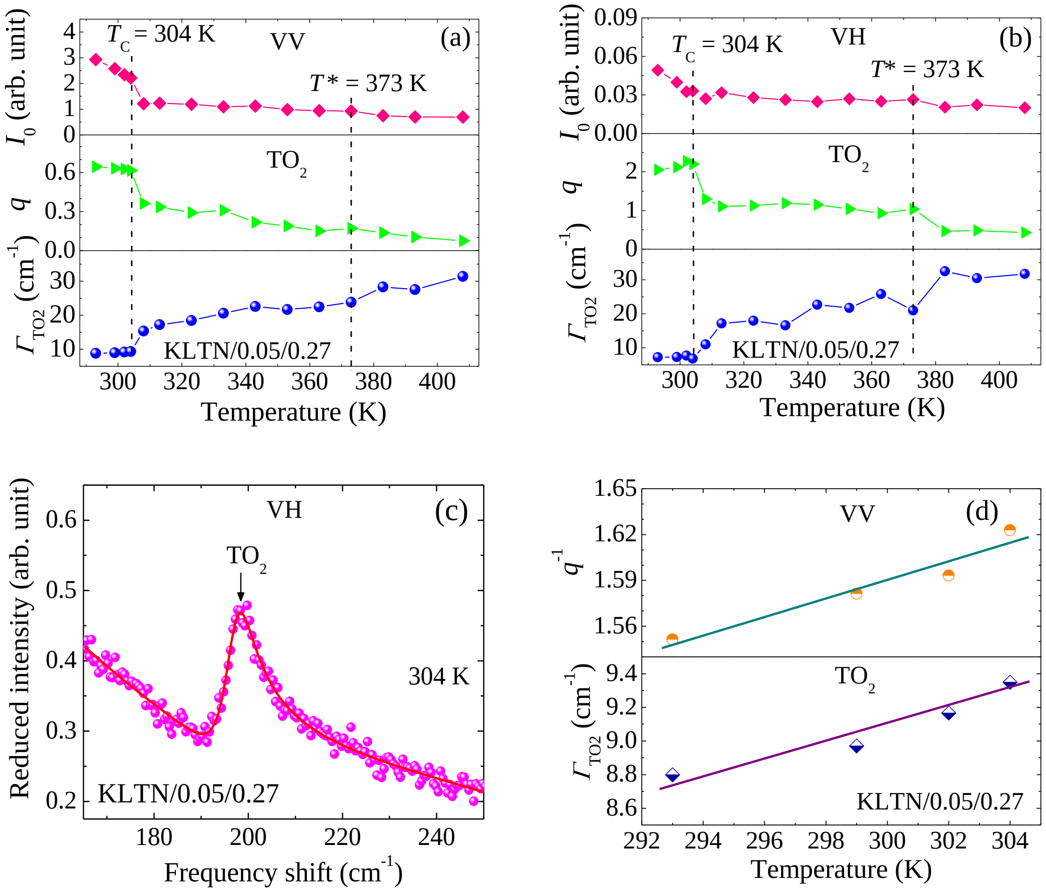

Fig. 5.3. The temperature dependence of reduced intensity, I_0, line shape parameter, q, and FWHM, Γ_{TO2} of the Fano resonance in (a) VV and (b) VH scattering spectra of the KLTN/0.05/0.27 crystal fitted by Eq. (3.7). The example of a fitted curve is shown in (c). (d) The temperature dependence of q^{-1} and Γ_{TO2} observed at the VV scattering geometry in the ferroelectric phase. The solid lines in (d) are guide to eyes.

It is also significant that the Γ_{TO2} shows the noticeable change associated with these precursor effects, therefore, the Fano resonance might be correlated with the PNRs. Since the polarization fluctuations of the PNRs give rise to the CP, hence, the coupling between the CP and the TO$_2$ phonon can a Fano resonance at about 196 cm^{-1} in Li-doped KTN crystals. The schematic illustration of the coupling phenomenon between CP and TO$_2$ phonon is shown in Fig. 5.4, where the broad CP induces by the fluctuating PNRs providing the continuum states, and sharp TO$_2$ phonon (Slater mode) gives a discrete state. The fluctuations of local polarizations in rhombohedral PNRs and the displacement pattern of the Slater mode are depicted in the left and right side in Fig. 5.4, respectively.

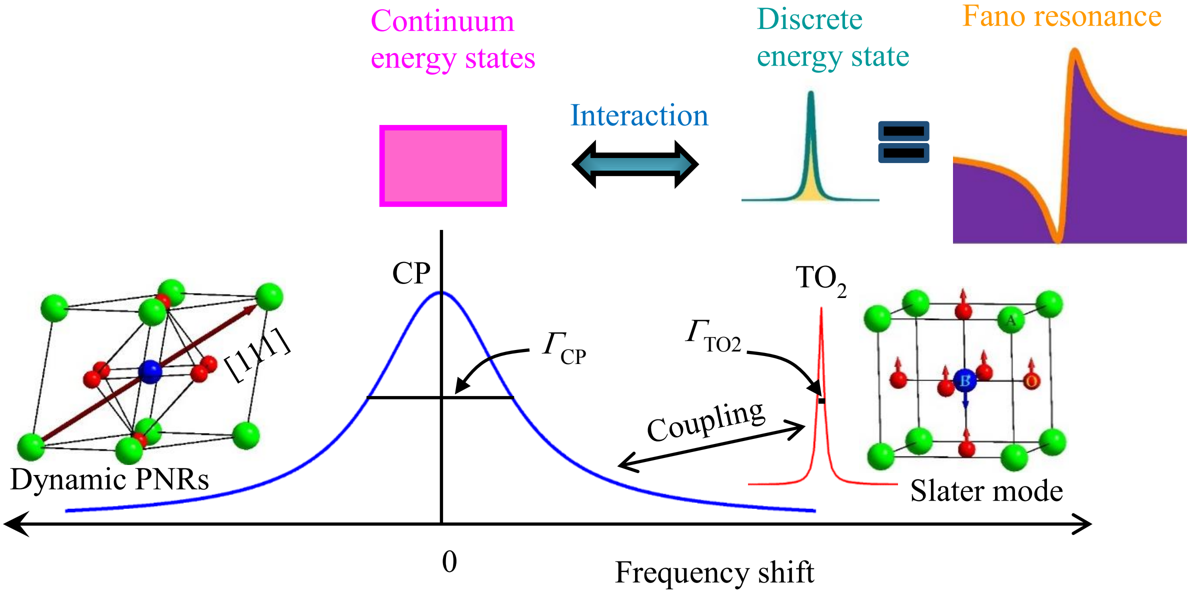

Fig. 5.4. A schematic illustration of the coupling between slow-relaxing CP (a broad spectrum indicates continuum states) and TO_2 phonon (a sharp spectrum indicates discrete state). The Γ_{CP} and Γ_{TO2} are the relaxation rates of the CP and TO_2 phonon, respectively, ($\Gamma_{CP} > \Gamma_{TO2}$). The displacement pattern of Slater mode is depicted in the right side, whereas dynamic PNRs is displayed in the left side. The local polarization in PNRs fluctuates along the equivalent [111] directions indicated by an arrow.

5.3.2 Angular dependence of Raman scattering spectra

For better understanding the physical origin of the Fano resonance in Li-doped KTN crystals, we analyzed the angular dependence of both VV and VH spectra in the cubic phase as shown in Figs. 5.5(a) and 5.5(b), respectively. The angular dependence of Raman spectra shows the periodic variation with the rotation of the plane of polarization, and the variation of the intensity was out of phase between VV and VH spectra. We are mainly concerned about the microscopic origin of the Fano resonance. In order to clarify the physical origin of the CP and the Fano resonance in the cubic phase, the angular dependence of Raman spectra was analyzed on the basis of Raman tensor calculations using Eq. (3.9) assuming the local symmetry of PNRs to The angular dependence of observed Raman intensity of the CP, I_{CP}, and the Fano resonance, I_{TO2}, in both VV and VH spectra in the cubic phase are plotted in Figs. 5.5(c) and 5.5(d), respectively. It is worth noting that the change of the intensity of the CP and the Fano resonance shows the similar dependence with the rotation of the plane of polarization. The change of the intensity of the CP and the Fano resonance observed at both VV and VH spectra is well fitted by the theory via Eqs. (3.12) and (3.13) as shown in Figs. 5.5(c) and 5.5(d), respectively. The fitted curves reproduce the observed intensity variations rather well, indicating that the CP and the Fano resonance in the cubic phase stem from the $E(x,y)$ symmetry of a rhombohedral $R3m$ symmetry of PNRs.

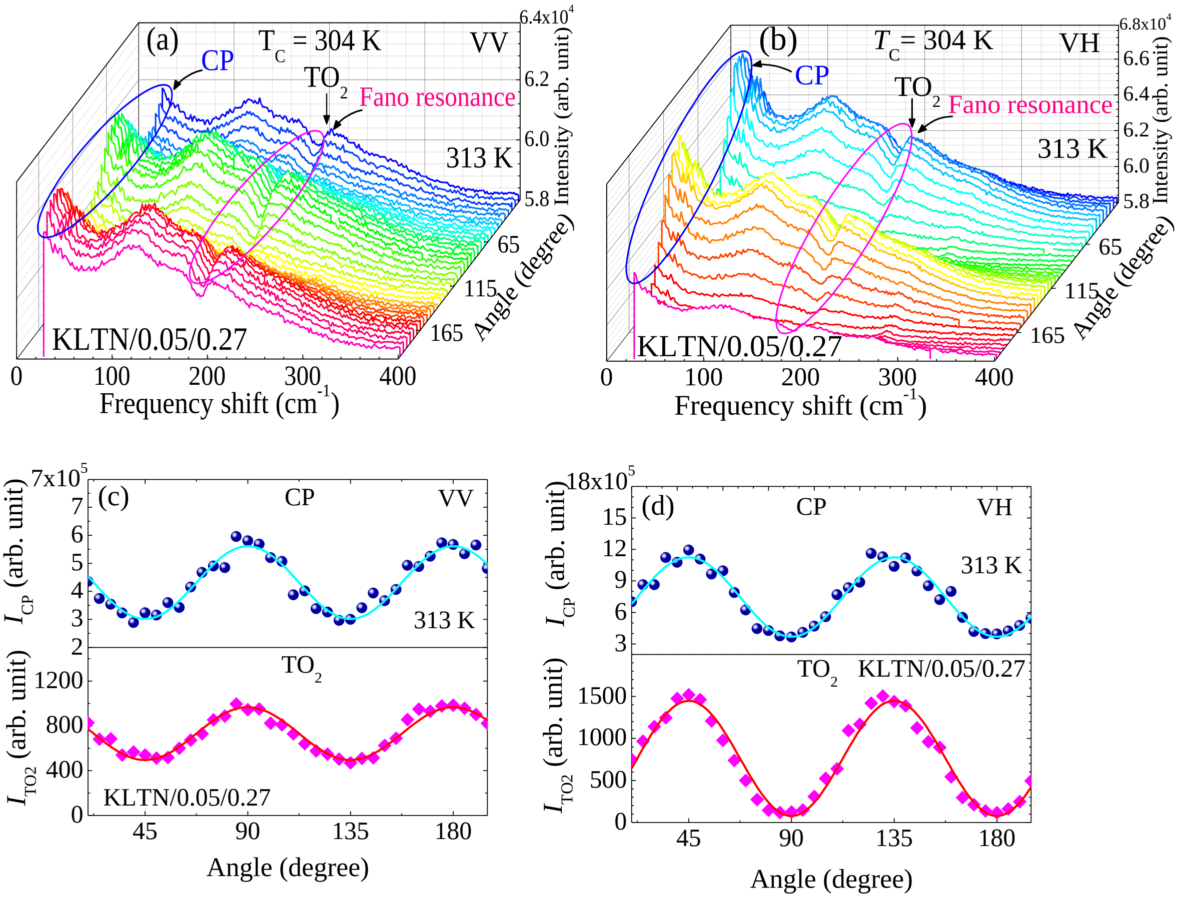

Fig. 5.5. Angular dependence of (a) VV and (b) VH Raman scattering spectra of the KLTN/0.05/0.27 single crystal measured at 313 K. The observed intensity of the CP (upper half) and the Fano resonance (lower half) in (c) VV and (d) VH spectra as a function of rotation angle. The solid lines in (c) and (d) are the best fitted curves using Eqs. (3.12) and (3.13), respectively.

5.3.3. Electric field induced Raman scattering spectra

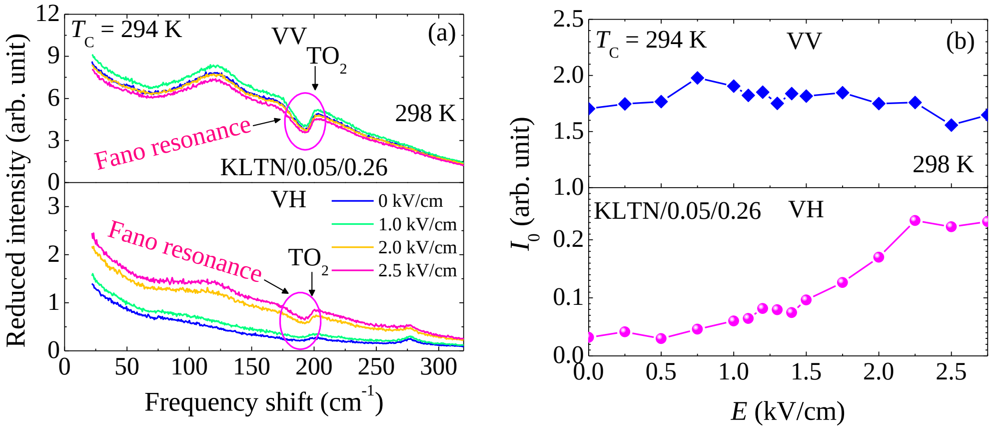

Fig 5.6. (a) Electric field dependence of both VV (upper half) and VH (lower half) Raman spectra of the KLTN/0.05/0.26 single crystal measured at 298 K. (b) The reduced intensity of the Fano resonance as a function of the electric field in both VV (upper half) and VH (lower half) spectra measured at 298 K.

In order to clarify the physical origin of the Fano resonance, the electric field dependence of Raman scattering spectra of the KLTN/0.05/0.26 single crystal was investigated above and below the T_C = 294 K. The lower value of the T_C of the KLTN/0.05/0.26 crystal than that of the KLTN/0.05/0.27 crystal occurs by the lower Nb concentrations. Figure 5.6 (a) shows the electric field dependence of Raman spectra of the KLTN/0.05/0.26 crystal in both VV and VH scattering measured at 298 K. It is interesting to note that the application of the electric fields causes the increase of the intensity for the VH spectra in the cubic phase, while no noticeable change appears for the VV spectra. In KTN, the relaxor-like behavior is originated from the correlated motion of the off-center Nb ions. These displacements are along equivalent [111] directions, and each one can switch between several equivalents or symmetry related sites as shown in Fig. 5.7(a).[12,26] The motion between these various orientations affects the off-diagonal components of the polarizability tensors, and therefore influences the intensity of the VH scattering. In this study, the electric field was applied along the *x* i.e., [100] direction, which is orthogonal to the *b*-*c* scattering plane. As a result, Nb ions became constrained for moving in this plane i.e., amongst four equivalent positions [Fig. 5.7(b)]. Such a motion enhances the intensity of the VH scattering, while preventing that of the VV one. This effect is clearly seen in Fig. 5.6(b), where the I_0 increases with increasing electric field in the VH spectrum, while in the VV spectrum the I_0 does not exhibit any appreciable change by the electric field. The switching of the Nb ions amongst four equivalent sites under the moderate electric fields can be the evidence of the dynamical response of local polarizations in the PNRs. Recently, the dynamic response of the PNRs under an electric field in the cubic phase of KTN was reported in Ref. 27. It is also expected that the restriction of the Nb ions to four sites results in a [100] time-averaged polarizations with the application of the sufficient applied field, and resulting in a crystal transforms into a lower tetragonal *P4mm* symmetry. Since the applied electric filed was not as high as that can induce the phase transition of the KLTN/0.05/0.26 crystal at 298 K, therefore the Raman spectra below 2.75 kV/cm was not same as observed spectra in the tetragonal phase, as presented in Fig. 5.1.

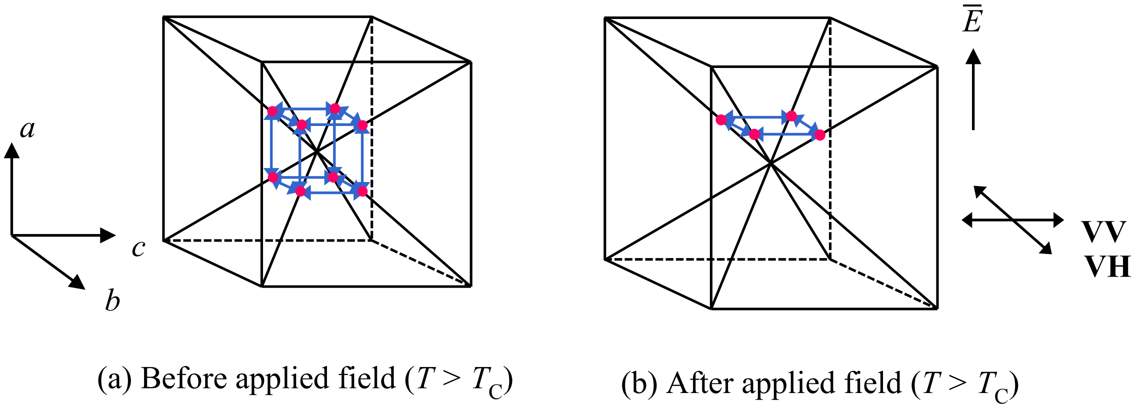

(a) Before applied field ($T > T_C$) (b) After applied field ($T > T_C$)

Fig. 5.7. A schematic illustration of off-center displacements of Nb ions in the cubic phase of the Li-doped KTN crystals in (a) before applied field and (b) after applied field. The off-centering of Li ions among the equivalent symmetry related sites, albeit not shown in the figure, can be described in a similar way.

To clarify the effects of the electric field on the Fano resonance of the Li-doped KTN crystals, we also performed the field induced Raman scattering in the ferroelectric phase where the microscopic local polarizations became a nanodomain state owing to the pinning of domain walls by the random fields. The electric field dependence of the I_0 and the A_{CP} measured at 275 K is displayed in Fig. 5.8. It is worth noting that the I_0 and the A_{CP} exhibits the anomalous change at E = 1.5 kV/cm. Since the applied electric field along [100] direction stabilizes a tetragonal phase, therefore, the field induced change at 1.5 kV/cm can be the transition from random nano-domain state caused by the freezing of PNRs to a single/macro domain state. Under electric field, such a transition from nano-domain state to a single/macro-domain state was observed in typical relaxor ferroelectrics.[28,29]

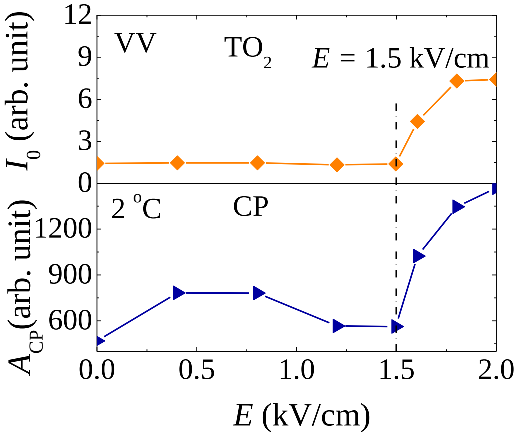

Fig. 5.8. The electric field dependence of the reduced intensity of the Fano resonance (upper half) and the CP (lower half) measured at 275 K.

5.4. Discussion on Fano resonance in Ferroelectrics

In the present study, the attention has been paid to clarify the microscopic origin of the Fano resonance in Li-doped KTN single crystals. The physical origin of the Fano resonance is discussed on the basis of different types of models and finally one model is chosen which reproduces the observed results appropriately. The Fano resonances reported in different types of materials may result from several different physical origins.[2-8] In $BaTiO_3$ single crystals, the Fano resonance at around 175 cm^{-1} was attributed to the interference effect arising from the coupling of a single phonon state to a two acoustical phonon state through the anharmonic terms in the potential function.[2] In that case, the variation of the intensity of the acoustical mode and the Fano resonance should be same in the wide temperature range. However, in Li-doped KTN crystals, the intensity of the 2TA mode did not exhibit any appreciable change in the cubic phase [Fig. 5.2(c)], whereas the intensity of the Fano resonance showed the noticeable temperature dependence [Figs. 5.3(a) and 5.3(b)]. Therefore, the coupling between the TO_2 phonon and the two acoustic phonons cannot be the origin of the Fano resonance in Li-doped KTN crystals.

Pinczuk *et al.* also suggested that the interference in $BaTiO_3$ crystals at about 175 cm^{-1} can be due to the anharmonic coupling of the lowest frequency TO phonon with the higher frequency TO phonon via acoustic phonons.[3] In Li-doped KTN crystals, the lowest frequency TO phonon vanished at the T_C, whereas the Fano resonance still existed above the T_C [Fig. 5.2(c)], and this fact again rules out the coupling of the lowest frequency TO phonon with the higher frequency TO phonon via acoustical phonons as the origin of our observation.

In the relaxor $Ba(Zr_{1/2}Ti_{1/2})O_3$ (BZT), the Fano resonance at around 155 cm^{-1} was caused by the interaction between the Ti and the Zr sublattices.[6] Interestingly, the Fano resonance in BZT was persisted up to 902 K, which is far above the $T_B \sim 450$ K at which dynamic PNRs start to appear. This is contrary to what was observed in the present observation, because the Fano resonance in Li-doped KTN crystals disappeared slightly above the T^* at which the dynamic to static transition of PNRs begins.

The inelastic light scattering study reported that the rapid polarization fluctuations in PNRs interfere with a polar TO phonon resulting in the Fano resonance in $SrTiO_3$ thin films and, $SrTiO_3$ and $Ca_xSr_{1-x}TiO_3$ nanocubes.[4,5] In Li-doped KTN crystals, since the I_0 and the Γ_{TO2} showed the noticeable change associated with these precursor effects, therefore the rapid polarization fluctuations in PNRs can be a good candidate for the continuum states. If the continuum states, which can interfere with the TO_2 phonon, are the rapid polarization fluctuations in PNRs in the Li-doped KTN crystals, then the Fano resonance must be appear just below the T_B. On the other hand, the Fano resonance in Li-doped KTN crystals disappeared just slightly above the T^*. Furthermore, it is significant that the value of the q gradually increased towards the T_C and became the maximum in the ferroelectric phase, where the local polarization fluctuations were totally absent.

According to the theory, the q parameter is the inversely proportional to the density of continuum states (ρ) and the interaction strength (V).[30,31] The Γ_{TO2} of the Fano resonance is proportional to the ρV^2. It is interesting to note that both Γ_{TO2} and q^{-1} increased approximately linearly with the temperature towards the T_C in the ferroelectric phase as shown in Fig. 5.3(d). These results reflect that the V does not vary strongly with the temperature, and the temperature dependence of both Γ_{TO2} and q^{-1} was caused by the increase of the density of continuum states towards the T_C. These results are similar to those observed in a ferroelectric semiconductor $Sn_2P_2Se_6$.[7] Hence, the interference between the polarization fluctuations in PNRs and the TO_2 phonon cannot be the origin of the Fano resonance in Li-doped KTN crystals.

Since the Fano resonance in Li-doped KTN crystals is affected by the precursor dynamics in the cubic phase, there can be the correlation between the Fano resonance and PNRs. It is well established that the dynamic PNRs in KTN and Li-doped KTN crystals are observed as the CP.[10-12,21] Therefore, to clarify the physical origin of the Fano resonance, it is worthy to compare the variation of the intensity of CP and the Fano resonance with the temperature, angular and electric field dependences of Raman spectra. It is clearly seen that the CP and the Fano resonance intensities showed the similar dependences on temperature, angular and electric field, which demonstrates that the Fano resonance is driven by the CP. On the basis of these results, it is concluded that the coupling between the CP and the TO_2 phonon can be the origin of the Fano resonance in Li-doped KTN single crystals.[8]

5.5 Summary

The microscopic origin of the Fano resonance in Li-doped KTN single crystals was investigated by the temperature, angular, and electric field dependences of Raman scattering. The local symmetry breaking in the cubic phase due to the existence of PNRs with $E(x,y)$ symmetry was observed by the intense first order Raman scattering, in which the first order scattering is forbidden by the cubic $Pm\bar{3}m$ symmetry. In the VH Raman spectra, the remarkable field dependence of the Fano resonance intensity in the cubic phase can be the dynamical response of local polarizations to the electric field. The CP and TO_2 phonon intensities showed the similar dependences on temperature, angular and electric field. From these experimental results, it is concluded that the origin of the Fano resonance in Li-doped KTN crystals is the coupling between polarization fluctuations in PNRs and the TO_2 phonon, both belong to the $E(x,y)$ symmetry of a rhombohedral $R3m$ symmetry of PNRs.

References

[1]U. Fano, Phys. Rev. **124,** 1866 (1961).

[2]D. L. Rousseau and S. P. S. Porto, Phys. Rev. Lett. **20,** 1354 (1968).

[3]A. Pinczuk, E. Burstein, and S. Ushioda, Solid State Commun. **7,** 139 (1969).

[4]A. A. Sirenko, I. A. Akimov, J. R. Fox, A. M. Clark, H.-C. Li, W. Si, and X. X. Xi, Phys. Rev. Lett. **82,** 4500 (1999).

[5]S. Banerjee, D.-I. Kim, R. D. Robinson, I. P. Herman, Y. Mao, and S. S. Wong, Appl. Phys. Lett. **89,** 223130 (2006).

[6]D. Wang, J. Hlinka, A. A. Bokov, Z.-G. Ye, P. Ondrejkovic, J. Petzelt, and L. Bellaiche, Nat. Commun. **5,** 5100 (2014).

[7]P. H. M. van Loosdrecht, M. M. Maior, S. B. Molnar, Yu. M. Vysochanskii, P. J. M. van Bentum, and H. van Kempen Phys. Rev. B **48,** 6014 (1993).

[8]S. Yoshino, G. Oohata, and K. Mizoguchi, Phys. Rev. Lett. **115,** 157402 (2015).

[9]D. A. Keen, IUCrJ **3,** 8 (2016).

[10]M. M. Rahaman, T. Imai, J. Miyazu, J. Kobayashi, S. Tsukada, M. A. Helal, and S. Kojima, J. Appl. Phys. **116,** 074110 (2014).

[11]R. Ohta, J. Zushi, T. Ariizumi, and S. Kojima, Appl. Phys. Lett. **98,** 092909 (2011).

[12]O. Svitelskiy and J. Toulouse, J. Phys. Chem. Solids **64,** 665 (2003).

[13]J. Toulouse, P. DiAntonio, B. E. Vugmeister, X. M. Wang, and L. A. Knauss, Phys. Rev. Lett. **68,** 232 (1992).

[14]Y. Yacoby, Z. Physik B **31,** 275 (1978).

[15]W. G. Nilsen and J. G. Skinner, J. Chem. Phys. **48,** 1413 (1967).

[16]S. K. Manlief and H. Y. Fan, Phys. Rev. B **5,** 4046 (1972).

[17]G. E. Kugel, M. D. Fontana, and W. Kress, Phys. Rev. B **35,** 813 (1987).

[18]G. E. Kugel, H. Mesli, M. D. Fontana, and D. Rytz, Phys. Rev. B **37,** 5619 (1988).

[19]S. Triebwasser, Phys. Rev. **114,** 63 (1959).

[20]D. Rytz and H. J. Scheel, J. Cryst. Growth **59,** 468 (1982).

[21]M. M. Rahaman, T. Imai, J. Kobayashi, and S. Kojima, Jpn. J. Appl. Phys. **54,** 10NB01 (2015).

[22]R. L. Prater, L. L. Chase, and L. A. Boatner, Solid State Commun. **40,** 697 (1981).

[23]J. Toulouse, F. Jiang, O. Svitelskiy, W. Chen, and Z.-G. Ye, Phys. Rev. B **72,** 184106 (2005).

[24]M. S. Islam, S. Tsukada, W. Chen, Z.-G. Ye, and S. Kojima, J. Appl. Phys. **112,** 114106 (2012).

[25]H. J. Trodahl, N. Klein, D. Damjanovic, N. Setter, B. Ludbrook, D. Rytz, and M. Kuball, Appl. Phys. Lett. **93,** 262901 (2008).

[26]O. Hanske-Petitpierre, Y. Yakoby, J. Mustre De Leon, E.A. Stern, and J. J. Rehr, Phys. Rev. B **44,** 6700 (1991).

[27]H. Tian, B. Yao, L. Wang, P. Tan, X. Meng, G. Shi, and Z. Zhou, Scientific reports **5,** 13751 (2015).

[28]T. H. Kim, S. Kojima, and J.-H. Ko, Curr. Appl. Phys. **14,** 1643 (2014).

[29]K. Matsumoto and S. Kojima, Jpn. J. Appl. Phys. **54,** 10NC04 (2015).

[30]M. V. Klein, *Light Scattering in Solids I* [Cardona, M. (ed.)] 147 (Springer-Verlag, Berlin, 1984).

[31]C. Tomsen, *Light Scattering in Solids VII* [Cardona, M. & Güntherodt, G. (ed.)] 285 (Springer-Verlag, Berlin, 1991).

Chapter 6

The Study on Composition Gradient Li-Doped $KTa_{1-x}Nb_xO_3$ Wafer by Micro-Brillouin Scattering

6.1 Introduction

The physical properties and structure of $KTa_{1-x}Nb_xO_3$ (KTN) are strongly dependent on the Nb content.[1,2] The physical properties such as an elastic constant, C_{ij}, which is related to the phase velocity of acoustic phonons at the center of the Brillouin zone and the inter-atomic potential, play an important role in materials science. Therefore, the accurate measurement of elastic constants and their temperature dependence as well as composition variation are important. By the ultrasonic pulse echo technique, the temperature dependences of the elastic properties of KTN with x = 0.012, 0.03, 0.08 and 0.157 were studied.[3] They observed that the elastic constants gradually decrease with the increase of Nb content. The similar results of KTN ($0.003 \le x \le 0.057$) were also reported in Ref. 4. By Brillouin scattering, the variation of elastic constants was reported in the case of PZN-0.045PT and PZN-0.09PT single crystals.[5] The analysis of temperature dependence of the elastic constants in the cubic phase of KTN single crystals suggested a strong coupling between phonons and polar nanoregions (PNRs).[3,6] As for integrated optics, a value of Curie temperature (T_C) near room temperature (RT) is highly desirable. However, as a common nature of solid solutions, the composition variation frequently occurs in a crystalline wafer. Therefore, it is necessary to characterize the composition gradient of a KTN wafer in the range where T_C is around RT. Moreover, another recent derivative i.e., Li-doped KTN an interesting system suitable for investigation of the effects of Li ions on the T_C and thus also related physical properties. Recently, Imai *et al.* observed the significant change in the capacitance and permittivity of the Li-doped KTN ($K_{0.95}Li_{0.05}Ta_{0.73}Nb_{0.27}O_3$, KLTN/0.05/0.27) crystal, which was induced by injecting electrons with the application of a voltage.[7] The injected electrons were trapped by the localized states in the crystal. The Li ions may be contributed to enhance the trap of injected electrons in the crystal. Therefore, for Li-doped KTN, the spatial variation of not only Nb but also Li ions also contribute the variation of the T_C.

On the other hand, defects have another important role on the elastic properties of materials. Theoretical study of the defect dependence of elastic properties of silicon crystals reported that both vacancy and interstitial defects, singly and/or in random combination, affect the elastic constants C_{11} and C_{44} of the silicon.[8] The decrease of the elastic constants C_{11} and C_{44} of the silicon by the defects was also reported in Ref. 9. Within our knowledge, no result was reported on the effect of defects on the elastic properties of high quality not only KTN but also Li-doped KTN single crystals.

In the present study, we investigated the defect dependence of the elastic properties of the composition gradient Li-doped KTN crystal wafer by micro-Brillouin scattering. The origin of positional dependence was discussed by the comparison with the temperature variation of elastic constants of the homogeneous KLTN/0.05/0.27 crystal.

6.2 Experimental

The Li-doped KTN single crystals used in the current study were grown at NTT Corporation by the top seeded solution growth technique. A crystal of an approximate size 36.00×35.00×1.48 mm^3 with large faces normal to [100] was polished to optical quality. Brillouin scattering in the frequency range from -65 to 65 GHz was studied by the high-contrast six-pass tandem Fabry-Perot interferometer (JRS TFP-1) combined with a modified optical microscope (Olympus BX60).[10] A free spectral range (FSR) of 75 GHz with a scan amplitude 470 nm was used to observe the Brillouin scattering spectra with a finesse ~100. A diode-pumped solid state laser (DPSS) was used to excite the sample with a wavelength of 532 nm and a power about 100 mW. A back scattering geometry was used to measure the Brillouin spectra.

6.3 Results and discussion

The composition gradient Li-doped KTN crystal wafer includes dislocations which appear during crystal growth from a seed along the [100] direction and the spatial distribution of T_C reflecting the composition gradient was schematically drawn in Figs. 6.1(a) and 6.1(b), respectively. The number density of dislocations was high near the center (grey color) of the sample along the [100] direction from the seed during crystal growth, which is from the top to the bottom in Fig. 6.1(a). By this reason, we divided the area of the sample into two parts to observe the effects of defects on the composition gradient Li-doped KTN. The region, where the number density of dislocation is high, marked by closed circles (red) are denoted as “high defects”, whereas other regions marked by closed rectangles (blue) are denoted as “low defects” throughout the article. The origin of the defects might be essentially screw dislocations, and additionally oxygen vacancies or protons.[11]

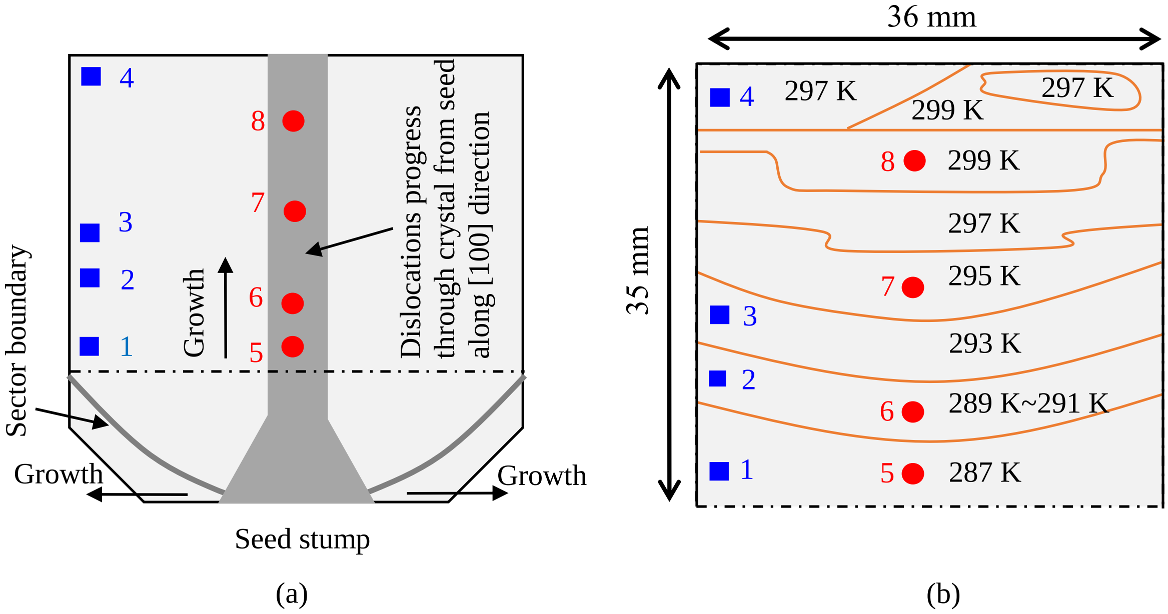

Fig. 6.1. Schematic illustration of (a) spatial heterogeneity and (b) the spatial dependence of Curie temperature in a composition gradient Li-doped KTN wafer. Closed circles (red) and rectangles (blue) denote the regions with high and low defect density regions, respectively.[12]

The typical Brillouin spectra of a FSR = 75 GHz observed at different positions in the low defects regions at RT (297 K) are shown in Fig. 6.2. The Brillouin doublet of longitudinal acoustic (LA) and transverse acoustic (TA) phonons was found in each spectrum. In addition, a central peak (CP), which is related to the relaxation process of dynamic PNRs, appeared in each spectrum. Similar spectra were observed in a homogeneous $KTa_{0.60}Nb_{0.40}O_3$ (KTN/0.40) single crystal in the vicinity of the T_C.[13] The observed LA and TA phonons are related to the elastic constants C_{11} and C_{44}, respectively.[14] In cubic symmetry, the TA mode is forbidden at the back scattering geometry in accordance to Brillouin selection rule.[14] Therefore, the existence of the TA mode in a cubic phase demonstrates the breaking of the cubic symmetry. Recently, the breaking of Raman selection rule of cubic symmetry in the high quality KTN/0.40 single crystal caused by PNRs with A_1(z) symmetry was observed by Raman scattering measurement.[13] The Brillouin doublet and CP were fitted using a Voigt function, where a width of a Gaussian component in the Voigt was fixed as an instrumental function. It is readily noticeable from Fig. 6.2 that the LA and TA phonons frequencies vary slightly with the positions. The positional variation of LA and TA phonon frequencies reflect the composition gradient.

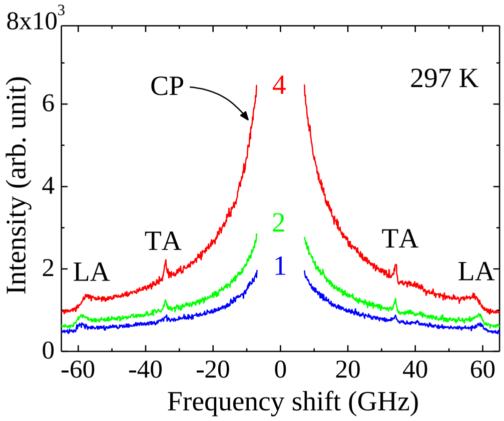

Fig. 6.2. Brillouin spectra at three positions, 1, 2, 4 in the low defects region.

The temperature dependences of the frequency shifts of LA and TA modes of a homogeneous Li-doped KTN i.e., $K_{0.95}Li_{0.05}Ta_{0.73}Nb_{0.27}$ (KLTN/0.05/0.27) single crystal are shown in Fig. 6.3. It is found that the LA phonon frequency exhibits the remarkable softening upon cooling towards T_C = 304 K, at the same time the TA phonon frequency shows the small discontinuity and slight softening. The continuous softening of LA and TA phonons down to the T_C = 304 K is due to the piezoelectric coupling of the fluctuating PNRs to the LA and TA phonons.[13,15] It is clearly seen from Fig. 6.3 that the frequency of the LA phonon begins to soften at higher temperature than the frequency of the TA phonon, implying that piezoelectric coupling for LA phonon is larger than that for the TA phonon near Burns temperature.[5]

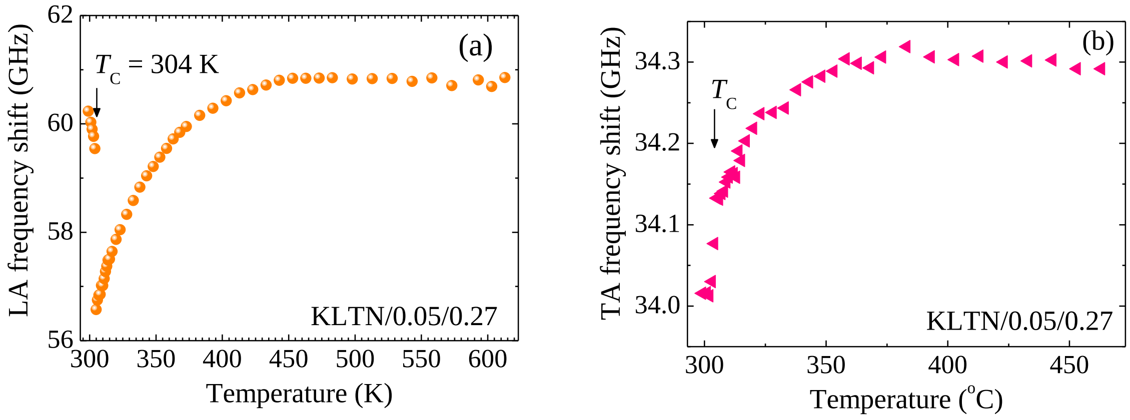

Fig. 6.3. The frequency shifts of (a) LA and (b) TA modes of a homogeneous KLTN/0.05/0.27 single crystal as a function of temperature.

The elastic constants C_{11} (related to LA phonon) and C_{44} (related to TA phonon) were determined using Eq. (4.1.1) and (4.1.2), respectively. The value of refractive index, n = 2.33, were used to calculate the elastic constants.[16] On the other hand, the value of density was used based on the expected value of T_C to calculate the elastic constants of the composition gradient Li-doped KTN crystal.[17] Figure 6.4 shows the positional dependence of elastic constants of the composition gradient Li-doped KTN crystal in the cubic coordinate system. It is found that both the elastic constants C_{11} and C_{44} gradually decrease with the increase of T_C i.e., increasing the Nb concentration in the low defects regions.

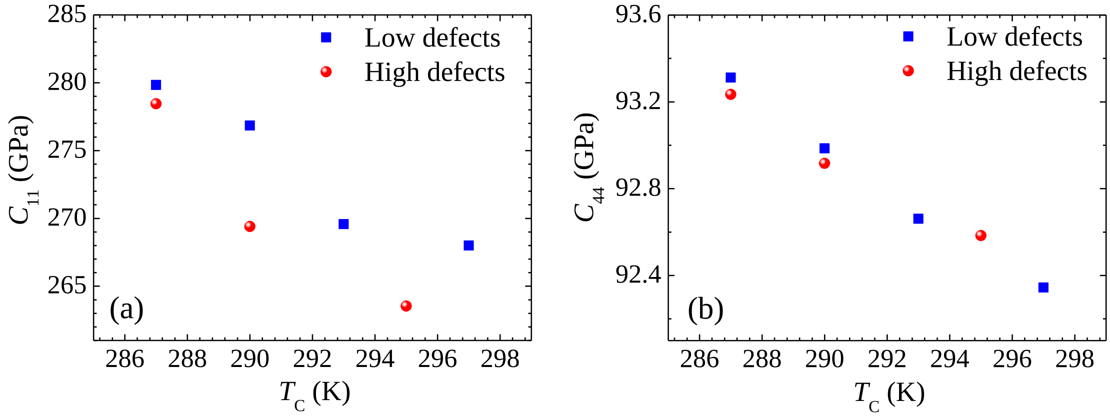

Fig. 6.4. Positional dependence of elastic constants (a) C_{11} and (b) C_{44} of the composition gradient Li-doped KTN wafer.

The variation of elastic constants C_{11} and C_{44} is related to the interaction of LA and TA phonon with PNRs, respectively.[5] These behaviours are very similar to those of temperature dependences observed in KTN single crystals by the ultrasonic pulse echo technique.[3] At 300 K, in the case of KTN/0.08 and KTN/0.157 crystals, the values of C_{11} around 390 GPa and 360 GPa were observed by the ultrasonic technique, respectively,[3] somewhat higher than those of our present results. Ko *et al.* studied the variation of elastic constants in 0.955Pb($Zn_{1/3}Nb_{2/3}$)O_3-0.045PbTiO_3 (PZN-0.045PT) and PZN-0.09PT crystals in the ferroelectric tetragonal symmetry at RT and they ascribed that the large difference was due to the difference in the contribution from the domain motion and domain walls.[5] However, we clearly observed the variation of elastic constants in the cubic phase (Fig. 6.4) where, there was no extrinsic contribution from the domain configurations. This fact indicates that the difference in C_{11} and C_{44} of the composition gradient Li-doped KTN single crystals can be caused only by the number density of defects and their different composition. Another possibility is that there might be the frequency dispersion of sound velocity among the high quality KTN crystals due to the difference of number densities of PNRs and their correlation length depending mainly on the Nb concentration. However, the acoustic phonons were markedly scattered by defects in the high defects regions, therefore the attenuations increase while velocity slightly decreases by the increase of the density of defects as shown in Fig. 6.4. The frequency of phonons decreased by the increase of defects, and it may indicate that defects enhance the creation of PNRs. In the non- ferroelectric materials such as silicon, the similar variation of elastic constants C_{11} and C_{44} by the density of defects was reported in Refs. 8 and 9.

In order to clarify the positional dependence of elastic constants of the composition gradient Li-doped KTN wafer, we compared the positional dependence with our results of the temperature dependence in a homogeneous KLTN/0.05/0.27 single crystal. The temperature dependence of the elastic constant C_{11} of a KLTN/0.05/0.27 crystal was determined from LA phonon frequency and plotted in Fig. 6.5. It is evident that the elastic constant C_{11} shows softening on approaching T_C = 304 K as similar to our previous study with no Li content. The elastic constant C_{11} measured on cooling exhibits almost a constant value at high temperatures, however on further cooling then significant softening occurs. Such a behavior was also observed in typical lead base relaxor ferroelectric materials.[18–20] The similar softening of the C_{11}

in KTN crystals was also studied by the ultrasonic pulse echo technique.[3] The softening of the C_{11} in the vicinity of the T_C can be caused by the piezoelectric coupling of the fluctuating PNRs and strain caused by acoustic waves.[13,15] As Li replaces K ions in KTN, the off-centered displacement of Li ions at the *A*-site may comprise an additional polarization.[21]

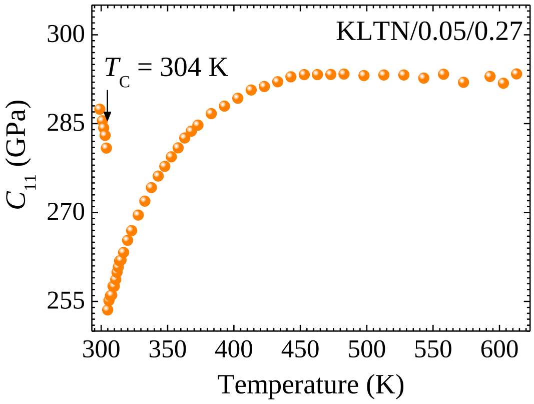

Fig. 6.5. Temperature dependence of the elastic constant C_{11} of a homogeneous KLTN/0.05/0.27 crystal.

This additional polarization is expected to be cooperative with neighboring polar clusters resulting in larger polar clusters which suppress the phonon frequency. Giulotto *et al.* observed such cooperative phenomena in KLTN/0.05/0.27 by Raman scattering in low Li concentrations.[22] The dipolar entities formed by the substitution of Nb and Li ions, of course, create random fields in the host $KTaO_3$. The lattice strains associated with these substituents also couple to the polarization setting up additional random fields or enhancing their presence.[23] The presence of random fields in KLTN/0.05/0.27 was related to the observation of stretched critical slowing down behavior in the vicinity of the T_C. The suppression of slowing down of the relaxation time by random fields was observed in relaxor ferroelectric PZN-0.07PT by the observation of stretched critical slowing down.[24] Figure 6.6 shows the comparison of elastic constant C_{11} between composition and temperature dependences. The effects of defects on the composition gradient KTN can be understood as the variation of the T_C on the basis of the result of KLTN/0.05/0.27 as shown in Fig. 6.6. It is clear from Fig. 6.6 that the value of C_{11} of the KLTN/0.05/0.27 is slightly larger than those values of the composition gradient Li-doped KTN at T_C. This might be due to the defect density and their composition variation.

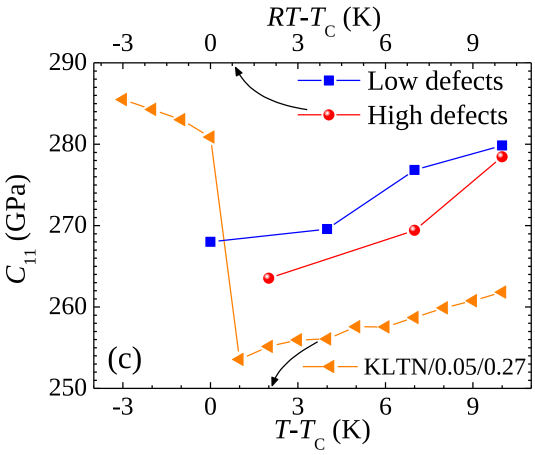

Fig. 6.6. Comparison of the elastic constant C_{11} between composition, defect density, and temperature dependences. The lower and upper transverse axes denote the difference in temperature from T_C in KLTN/0.05/0.27 and the difference in T_C from RT in a composition gradient Li-doped KTN, respectively.

6.4 Summary

The positional dependence of the elastic properties of the composition gradient KTN crystal wafer was investigated by micro-Brillouin scattering. The variation of elastic constants with the composition gradient was clearly observed. The positional change of elastic constants C_{11} and C_{44} was discussed in relation with the temperature dependences of LA and TA phonons of a homogeneous sample. The suppression of elastic constants by the defects of the composition gradient KTN wafer was observed with the comparison of the regions between high and low defect density.

References

[1]S. Triebwasser, Phys. Rev. **114,** 63 (1959).

[2]D. Rytz and H. J. Scheel, J. Cryst. Growth **59,** 468 (1982).

[3]L. A. Knauss, X. M. Wang, and J. Toulouse, Phys. Rev. B **52,** 13261 (1995).

[4]D. Rytz, A. Châtelain, and U. T. Höchli, Phys. Rev. B **27,** 6830 (1983).

[5]J-H. Ko, D. H. Kim, and S. Kojima, Phys. Rev. B **77,** 104110 (2008).

[6]O. Svitelskiy, A. V. Suslov, J. B. Betts, A. Migliori, G. Yang, and L. A. Boatner, Phys. Rev. B **78,** 064113 (2008).

[7]T. Imai, S. Toyoda, J. Miyazu, J. Kobayashi, and S. Kojima, Appl. Phys. Express **7,** 071501 (2014).

[8]L. A. Clark, Y. Xianglong, Z. B. Martin, and W. H. Linn, Phys. Rev. B **70,** 134113 (2004).

[9]P. J. Burnett and G. A. D. Briggs, J. Mater. Sci. **21,** 1828 (1986).

[10]S. Kojima, Jpn. J. Appl. Phys. **49,** 07HA01 (2010).

[11]T. Imai, S. Yagi, and H. Yamazaki, J. Opt. Soc. Am. B **13,** 2524 (1996).

[12]http://www.ntt.co.jp/about_e/group.html

[13]M. M. Rahaman, T. Imai, J. Miyazu, J. Kobayashi, S. Tsukada, M. A. Helal, and S. Kojima, J. Appl. Phys. **116,** 074110 (2014).

[14]R. Vacher and L. Boyer, Phys. Rev. **B 6,** 639 (1972).

[15]R. Ohta, J. Zushi, T. Ariizumi, and S. Kojima, Appl. Phys. Lett. **98,** 092909 (2011).

[16]F. S. Chen, J. E. Geusic, S. K. Kurtz, J. G. Skinner, and S. H. Wemple, J. Appl. Phys. **37,** 388 (1966).

[17]A. Reisman and E. Banks, J. Am. Chem. Soc. **80,** 1877 (1958).

[18]S. Tsukada and S. Kojima, Phys. Rev. B **78,** 144106 (2008).

[19]S. Kojima, S. Tsukada, Y. Hidaka, A. A. Bokov, and Z-G. Ye, J. Appl. Phys. **109,** 084114 (2011).

[20]V. Sivasubramanian, S. Tsukada, and S. Kojima, J. Appl. Phys. 105(1–5), 014108 (2009).

[21]W. Kleemann, S. Kütz, and D. Rytz, Europhys. Lett. **4,** 239 (1987).

[22]E. Giulotto, P. Galinetto, P. Camagni, G. Samoggia, V. A. Trepakov, L. Jastrabik, and P. P. Syrnikov, J. Phys.: Condens. Matter **12,** 6935 (2000).

[23]G. A. Samara and L. A. Boatner, Phys. Rev. B **61,** 3889 (2000).

[24]S. Kojima and S. Tsukada, Ferroelectrics **405,** 32 (2010).

Conclusions

This dissertation is devoted to clarify the dynamical behaviors of polar nanoregions (PNRs) in high quality Nb rich $KTa_{1-x}Nb_xO_3$ (KTN) and Li-doped KTN single crystals by inelastic light scattering. The dielectric measurements were also carried out to understand the dynamical behavior of relaxor-like ferroelectrics. The KTN high quality single crystals of with $x = 0.40$, 2.5%Li-doped KTN with $x = 0.38$, 5%Li-doped KTN with $x = 0.27$ and 0.26 were studied. The conclusions are as follows:

The precursor dynamics of relaxor-like ferroelectric phase transitions in non-dope and Li-doped KTN single crystals were investigated by Brillouin and Raman scattering. In the vicinity of the Curie temperature, T_C, the remarkable softening of sound velocity and the increase of sound attenuation were observed in both non-doped and Li-doped KTN single crystals. The increase in the central peak (CP) intensity and sound attenuation as well as significant softening of the V_{TA} were clearly observed below the intermediate temperature, T^*, indicating the start of the rapid growth of dynamic PNRs. The temperature variation of the mean size of dynamic PNRs in both crystals is evaluated, and below the T^*, it markedly increases down to T_C towards the percolation limit. In non-doped and Li-doped KTN, the relaxation time estimated by the width of a broad CP shows the critical slowing down towards T_C, which is the evidence of the order-disorder nature of a ferroelectric phase transition. Any soft mode behavior of both non-doped and Li-doped KTN crystals was not found by Raman scattering. Thus, it is concluded that the nature of the phase transition of non-doped, 2.5%Li-doped, 5%Li-doped KTN crystals is purely order-disorder. In the paraelectric cubic phase, the broken symmetry due to the existence of dynamic PNRs was proved by the intense first-order Raman scattering, nevertheless the first order scattering is Raman inactive for the cubic $Pm\bar{3}m$ symmetry. In the cubic phase, the microscopic origin of the CP of non-doped and 2.5%Li-doped KTN is attributed to $A_1(z)$ symmetry mode of PNRs, while in 5%Li-doped KTN the CP is attributed to $E(x,y)$ symmetry mode of PNRs by the measurement of the angular dependence of Raman scattering.

The Li-doping effect on KTN crystals was clearly seen as the stretching of the slowing down and broadening of the elastic anomaly in the 5%Li-doped KTN in comparison with those of the non-doped KTN by Brillouin scattering. The enlargement of the temperature region of the elastic anomaly in Li-doped KTN can be attributed to the fact that the random fields by doped Li ions enhance the growth of PNRs. By the Li-doping, the remarkable increase of the mean size of the dynamic PNRs towards T_C was also found. The broadening of the elastic anomaly can be the evidence of the enhanced relaxor nature of 5%Li-doped KTN single crystals. The enhanced relaxor nature by the Li-doping was also confirmed by the dielectric properties using the extended Curie-Weiss law. By the 5%Li-doping, the change of symmetry from $A_1(z)$ to $E(x,y)$ of the local modes in PNRs was observed by the angular dependence of Raman scattering. The first-principles calculation shows the partial occupancy of 5%Li ions at B-site. The total energy at A- and B-site occupancy of the perovskite structure for the Li-doped KTN was calculated by the density functional theory. In a stable equilibrium state, 4.2%Li ions occupy A-site, while the rest of 0.8% Li ions occupy B-site. Thus, the increase of the random field strength induced the partial occupancy of Li ions at B-site can cause by the hetero-valence charge disorder at B-site. Such an enhancement of random fields can be the physical origin on the suppression of the critical slowing down of the relaxation time near T_C and the change of the local mode symmetry of PNRs.

The microscopic origin of the Fano resonance was investigated in 5%Li-doped KTN single crystals by Raman scattering. The intensity of the CP (polarization fluctuations in PNRs) and the transverse optical phonon at about 196 cm^{-1} (Slater mode) shows the similar dependences on temperature, angular and electric field dependences of Raman scattering spectra. The angular dependence shows that the CP and the Slater mode belong to the $E(x,y)$ symmetry. In the cubic phase, the significant electric field dependence of the Fano resonace intensity in the VH Raman spectra can be caused by the switching of local polarizations in PNRs perpendicular to the applied electric field. At constant temperature of 275K, the significant change of the intensity of both CP and Fano resonance was attributed to the transition from random nano-domain state to a single/macro-domain state at the field, $E \sim 1.5$ kV/cm. From these observations, it is concluded that the origin of the Fano resonance in 5%Li-doped KTN crystals is the coupling between polarization fluctuations in PNRs and the Slater mode with the $E(x,y)$ symmetry.

We clearly observed the variation of elastic constants in a composition gradient KTN crystal wafer by micro-Brillouin scattering. The effect of defects on the elastic properties of was also investigated using the same wafer. By the defects, the suppression of elastic constants was observed in comparison between the regions of high and low defect density regions in the wafer.

List of publications

1. **M. M. Rahaman**, T. Imai, J. Miyazu, J. Kobayashi, S. Tsukada, M. A. Helal, and S. Kojima
   "Relaxor-like dynamics of ferroelectric $K(Ta_{1-x}Nb_x)O_3$ crystals probed by inelastic light scattering", J. Appl. Phys. **116,** 074110 (2014).
2. **M. M. Rahaman**, T. Imai, J. Kobayashi, and S. Kojima
   "Effect of Li-doping on polar-nanoregions in $K(Ta_{1-x}Nb_x)O_3$ single crystals", Jpn. J. Appl. Phys. **54,** 10NB01 (2015).
3. **M. M. Rahaman**, T. Imai, J. Miyazu, J. Kobayashi, and S. Kojima
   "Micro-Brillouin scattering study on composition gradient Li doped $KTa_{1-x}Nb_xO_3$ wafer", Ferroelectrics **487,** 47 (2015).
4. **M. M. Rahaman**, T. Imai, T. Sakamoto, S. Tsukada, and S. Kojima
   "The role of polar-nanoregions in $KTa_{1-x}Nb_xO_3$ single crystal studied by Raman scattering", Accepted for the publication in "Ferroelectrics".
5. **M. M. Rahaman**, T. Imai, T. Sakamoto, S. Tsukada, and S. Kojima
   "Electric field effect on Fano resonance of Li-doped $KTa_{1-x}Nb_xO_3$ single crystals studied by Raman scattering", to be submitted in "Scientific Reports".

List of conferences

A. Oral presentation

1. **M. M. Rahaman**, T. Imai, J. Miyazu, J. Kobayashi, and S. Kojima
 "Raman scattering study of cubic-tetragonal phase transition in ferroelectric $KTa_{1-x}Nb_xO_3$ crystals", The 13th Japan-Korea joint workshop in materials science, University of Tsukuba, Japan.
2. **M. M. Rahaman**, T. Imai, J. Miyazu, J. Kobayashi, and S. Kojima
 "Ferroelectric phase transition of $KTa_{1-x}Nb_xO_3$ crystals studied by Raman scattering", 31st meeting on ferroelectric materials and their applications, Kyoto, Japan.
3. **M. M. Rahaman**, T. Imai, J. Miyazu, J. Kobayashi, and S. Kojima
 "Critical slowing down and elastic anomaly of Li doped $KTa_{1-x}Nb_xO_3$ probed by micro-Brillouin scattering", 70th annual meeting of the physical society of Japan (JPS), Waseda university, Japan.
4. **M. M. Rahaman**, T. Imai, J. Miyazu, J. Kobayashi, and S. Kojima "Effect of Li-doping on polar-nanoregions in $KTa_{1-x}Nb_xO_3$ crystals", 32th meeting on ferroelectric materials and their applications, Kyoto, Japan.
5. **M. M. Rahaman**, T. Imai, J. Kobayashi, and S. Kojima
 "Electric field induced ferroelectric phase transition and critical endpoints of Li-doped $KTa_{1-x}Nb_xO_3$ single crystals studied by Brillouin scattering", 76th autumn meeting of the Japan society of applied physics (JSAP), Nagoya, Japan.

B. Poster presentation

1) **M. M. Rahaman**, T. Imai, J. Miyazu, J. Kobayashi, and S. Kojima
 "Brillouin and Raman scattering studies of phase transitions of KTN single crystals", 13th international meeting on ferroelectricity, Krakow, Poland.
2) **M. M. Rahaman**, T. Imai, J. Miyazu, J. Kobayashi, and S. Kojima
 "Micro-Brillouin scattering study on composition gradient $KTa_{1-x}Nb_xO_3$ crystals", 9th Asian meeting on ferroelectricity and 9th Asian meeting on electroceramics (AMF-AMEC-2014), Shanghai institute of ceramics, China.
3) **M. M. Rahaman**, T. Imai, J. Miyazu, J. Kobayashi, and S. Kojima
 "Raman scattering study of a ferroelectric phase transition o KTN crystals", 61st spring meeting of the Japan society of applied physics (JSAP), Tokyo, Japan.
4) **M. M. Rahaman**, T. Imai, J. Miyazu, J. Kobayashi, and S. Kojima
 "The role of dynamic polar nanoregions in $KTa_{1-x}Nb_xO_3$ single crystals studied by Raman scattering", 10th Japan-Korea conference on ferroelectrics (JKC-FE-10), Hiroshima, Japan.
5) **M. M. Rahaman**, T. Imai, J. Miyazu, J. Kobayashi, and S. Kojima
 "Elastic properties of $KTa_{1-x}Nb_xO_3$ studied by Brillouin scattering and first-priciples calculation", International workshop on science and patents (IWP-2014), University of Tsukuba, Japan.

Acknowledgements

It is an immense pleasure to express acknowledge and sincere regards to my academic advisor **Professor Seiji Kojima**, Institute of Materials Science, University of Tsukuba, who warmly welcomed me as part of their research group. I would like to express heart-felt gratitude to **Prof. S. Kojima** for his continued guidance, encouragement, and keen interest in my research. I also feel that the treatise would not have come to the current form without his kind co-operation.

I would like to express gratitude to NTT Corporation for providing high quality KTN and Li-doped KTN single crystals. I am thankful to Dr. T. Imai (NTT Corporation) for his valuable discussion on the experimental results. I would like to express sincere gratitude to Prof. S. Tsukada (Shimane University) for providing experimental facilities, precious advices and explanations on the research results. I am also grateful to Prof. J.-H. Ko (Hallym University, South Korea), Prof. T. Mori, (University of Tsukuba) and Dr. G. Shabbir (PINSTECH, Pakistan) for their fruitful discussion in connection to my research. I express my gratitude to all of existing and former members of Kojima laboratory for their technical support, help, and friendly behavior during my Ph.D. study.

I would like to express gratitude with great pleasure to the Japanese government for the financial support as MONBUKAGAKUSHO (MEXT) scholarship. For the partial financial support in my research, Marubun Research Promotion Foundation is also gratefully acknowledged.

It is beyond my words to express gratitude to Prof. M. Mozibur Rahman (University of Rajshahi, Bangladesh) for his extended moral support and motivation to proceed for Ph.D. study. I would like to express my gratefulness to my parents and relatives for their mental support and inspiration. I also really want to thank my friends, colleagues and well-wishers for their inspiration and cooperation. Finally, I would like to special thanks to my wife, Mst. Nahida Aktar, and beloved daughter, Nabila Rahaman Naba, for their sweet love, patience, mental support, and encouragement during the course of my long stay in Japan.